

Numerical Study of Flow over a Rotating Cone under Axial and Non-Axial Inflow

Srijan K. Mukhopadhyay

Technische Universiteit Delft

Numerical Study of Flow over a Rotating Cone under Axial and Non-Axial Inflow

by

Srijan K. Mukhopadhyay

in partial fulfillment of the requirements for the degree of

Master of Science
in Aerospace Engineering

at the Delft University of Technology,
to be defended publicly on 27th October, 2020.

Supervisors:	ir. Sumit Tambe	
	Dr. Arvind G. Rao	
	Dr. Ivan Langella	
Thesis committee:	Dr. A.G. Rao	
	Dr. I. Langella,	TU Delft
	Dr. A. C. Viré,	TU Delft
	Ir. S. S. Tambe,	TU Delft

An electronic version of this thesis is available at <http://repository.tudelft.nl/>.

Acknowledgment

Although it goes without saying, my parents are the very first individuals I would like to show my gratitude towards. Without their support and sacrifices, the dream of obtaining a higher education degree, from one of the best universities in the world, would never have come to fruition. I also take this opportunity, to thank my cousin sister, Baishali Chatterjee, and my cousin-in-law Dr. Nilanjan Chaterjee for their constant support throughout this endeavour. My visits to their home in the UK were always filled with joy, laughter, and amazing food. I will forever be grateful for everything they have done for me.

This thesis would not be possible without my supervisor, Dr. Arvind Gangoli Rao. I would like to thank him for giving me the opportunity to work on this topic and for guiding me throughout the duration of the thesis. My gratitude also extends towards my daily supervisor, ir. Sumit Tambe, for his constant advice over the course of my thesis. I also would like to thank him for perusing through my report and providing me with detailed feedback, this helped me edit and make improvements. My gratitude also extends towards, Dr. Ivan Langella. His guidance regarding some of my doubts in the simulations was invaluable. I will forever be grateful for all our constructive discussions during our meetings. I also thank Dr. Axelle Viré for being part of my thesis committee. In addition, I would also like to give special thanks to Martijn van Sluis, MSc and Biagio Della Corte, Msc for allowing me to share their workstation for part of this thesis and also providing me with some helpful tips on ICEM CFD.

Amongst my friends, my heartfelt thanks first extends towards Sampath! His help during the past few months was absolutely invaluable and I have always enjoyed our discussions over Skype. I was kept motivated by the constant chitchats with Amogh, Chaitanya, Katja, Rohan, Hazel and Chetan on random topics, from sports to politics along with cooking, often random, Indian dishes. My sincere thanks to Arjun, Kishan, and Anand as well for their help in completing FMT during my thesis.

I also would like to thank Rishabh for our phone calls and discussions on science and technology, I always enjoy them! Last but in no ways the least, my most sincere thanks goes towards, Akshay, Anuj, Dheer, Piyush, Lakshay, Aamir, Utkarsh, and Samadrita for all our long video calls which had kept me going throughout the last few years here in Europe, more so in the past few months (with our almost daily video calls) as our world reels from the effects of the Covid-19 pandemic.

Srijan K. Mukhopadhyay
Delft, The Netherlands

Abstract

Although significant strides have been made with regards to increasing the fuel economy of commercial passenger aircraft, the reduction of the environmental footprint remains of the utmost importance. The flow development over an aero-engine spinner will affect the velocity distribution over the fan of the engine and this affects the estimation of the losses generated in the fan and consequently the performance of the engine itself. Several theoretical and experimental studies have been conducted over different spinner geometries. The experimental studies have shown the existence of spiral vortices formed due to boundary layer instabilities over a rotating cone under axial and non-axial inflow. To study the effects of hub-corner separation in detail, it is first important to check the efficacy of existing commercial numerical simulation tools in the prediction of this boundary layer transition development of flow over a rotating nose-cone.

The objective of the thesis was thus to simulate using Unsteady Reynolds Averaged Navier Stokes (URANS) and Large Eddy Simulations (LES), the formation of the counter rotating vortices over the rotating cone. To this end, ANSYS DesignModeler and ICEM CFD were used to generate a meshed computational domain and ANSYS CFX was used as the solver.

With axis-symmetric cones considered as an idealised geometry for the spinner of an aircraft engine, a 15° half angle cone with a diameter of 47 mm was chosen. The tip of this cone was blunted by a factor of $1/100^{\text{th}}$ of the cone diameter. The domain diameter was set to 10 times the diameter of the cone so as to reduce the impact of the flow over the side walls. Two structured hexahedral meshes were generated with different refinements.

The Baseline Explicit Algebraic Reynolds Stress Model was chosen for the URANS simulation and the Wall Adapting Local Eddy Viscosity Model for the LES run. To check if the simulations were able to capture the vortices, the footprint left behind by them were visualised using the instantaneous wall shear values. This was non-dimensionalised using the free stream dynamic pressure. The variable was named the wall friction coefficient.

The magnitude of the inlet flow velocity given was 2.46 m/s. A 2° incidence is given to the flow for the non-axial case. The effect of mesh refinement was studied for the axial case using both meshes and the finer mesh was used for the non-axial case. The axial case was studied using both the URANS and LES runs, while the non-axial case was studied using only the LES run.

In addition to the footprint by the vortices, the variation of local Reynolds number (defined using boundary layer edge velocity) with local rotation ratio (defined using local radius, boundary layer edge velocity, and rotation velocity of the cone) was also studied and compared with available experimental data. The wall parallel velocity profiles over the length of the cone were also studied. Using the contours of the wall parallel velocity, the momentum mixing in the boundary layer due to the vortices was visualised and compared with the results from the experiments.

To characterise the spatial development of the spiral vortices, a critical point was defined using the wall friction coefficient. This critical point was then compared to the one obtained through the experiments. The number of counter rotating vortices formed over the length of the cone was also checked and the trend between the simulations and experiments were compared.

List of Abbreviations

Abbreviations

BLI	Boundary Layer Ingestion
BSL EARSM	Baseline Explicit Algebraic Reynolds Stress Model
CFD	Computational Fluid Dynamics
CFL	Courant-Fredrichs-Lewy
DNS	Direct Numerical Simulation
LES	Large Eddy Simulation
NASA	National Aeronautics and Space Administration
RANS	Reynolds Averaged Navier Stokes
SGS	Subgrid Scale
URANS	Unsteady Reynolds Averaged Navier Stokes
WALE	Wall Adapting Local Eddy Viscosity

Symbols and Variables

α	Angle of incidence
C_f	Wall friction coefficient
C_s	Smagorinsky constant
Δt	Time step
Δx	Mesh node spatial spacing
G	Görtler number
μ_{SGS}	SGS eddy viscosity
ν_{SGS}	SGS kinematic viscosity
ω	Rotational velocity
Ω_{ij}	Vorticity tensor
Re	Reynolds number
Re_D	Diameter based Reynolds number
Re_l	Local Reynolds number
$Re_{l,c}$	Critical local Reynolds number
ρ	Density
S	Local rotational speed ratio
S_{ij}	Shear strain rate tensor
θ	Cone half angle
I	Turbulence intensity
u_e	Boundary layer edge velocity
U_∞	Free stream velocity
y^+	Non-dimensional height of first cell

Contents

Acknowledgment	iii
Abstract	v
List of Figures	xi
List of Tables	xv
1 Introduction	1
1.1 Report Structure	3
2 Literature Review	5
2.1 Theoretical Background	5
2.1.1 Flow over Axis-symmetric bodies	5
2.1.2 Flow Instabilities	7
2.1.3 Secondary Flow Structures	8
2.1.4 Effect of Boundary Layer Ingestion	8
2.2 Early Studies	9
2.3 Recent Studies	17
2.4 Vortex Visualisation	19
2.4.1 Mathematics	19
2.4.2 λ_2 Criterion	20
2.4.3 Q Criterion	20
2.4.4 Δ Criterion	21
2.4.5 Swirling Strength Criterion	21
2.4.6 Helicity	21
2.4.7 Swirl Parameter Method	21
2.4.8 Eigenvector Method	22
2.4.9 Maximum Vorticity	22
2.4.10 Streamline Method	22
2.5 Conclusions and Research Objective	22
3 Turbulence Modelling	31
3.1 Navier Stokes Equations	31
3.2 Characteristics and Effects	33
3.3 Energy Cascade	34
3.4 Reynolds Averaged Navier Stokes (RANS)	35
3.5 Large Eddy Simulations (LES)	35
3.5.1 Smagorinsky Eddy Viscosity Model	36
3.5.2 Dynamic Smagorinsky-Lilly Model	37
3.5.3 Wall Adapted Local Eddy-Viscosity Model (WALE)	38
3.6 Direct Numerical Simulation (DNS)	38
4 Numerical Methodology	41
4.1 Workflow	41
4.2 Geometrical Model	41
4.3 Mesh Methodology	42
4.4 Case Setup	44
4.4.1 Case 1	46
4.4.2 Case 2	48
4.4.3 Case 3	50

5	URANS: Axial Inflow	51
5.1	Analysis	51
5.2	Potential Cause	52
6	LES: Axial Inflow	55
6.1	Coordinate System	55
6.2	Mesh 1	55
6.2.1	Vortex Footprint	56
6.2.2	Wall Parallel Velocity Profiles.	56
6.2.3	Wall Friction Coefficient Variation	56
6.2.4	Local Reynolds Number Variation	57
6.3	Mesh 2	58
6.3.1	Vortex Footprint	58
6.3.2	Wall Parallel Velocity Profiles.	58
6.3.3	Wall Friction Coefficient Variation	59
6.3.4	Local Reynolds Number Variation	59
6.4	Spatial Distribution of Vortices	59
6.5	Conclusions.	60
7	LES: Non-Axial Inflow	75
7.1	Vortex Footprint	76
7.2	Reynolds Number.	78
7.3	Wall Parallel Velocity Profile	79
7.4	Spatial distribution of Vortices	80
7.5	Conclusions.	80
8	Conclusions and Recommendations	87
8.1	Conclusions.	87
8.2	Limitations	88
8.3	Recommendations	89
8.3.1	Meshing	89
8.3.2	Future Work	89
A	Plane Boundary Layer Equation	91
B	Linear Stability Theory	95
C	Baseline Explicit Algebraic Reynolds Stress Model	97
	Bibliography	99

List of Figures

1.1	"Starry Night" - Vincent van Gogh	1
1.2	D8 Configuration	2
1.3	Transition process observed over cone rotating at 700 rpm and axial inflow of 2.9 m/s (Image source: [2])	3
2.1	Generic axis-symmetric geometry (Image source: [10])	5
2.2	Disturbances in the boundary layer of flow over curved surfaces (Image source: [14])	8
2.3	Normalised streamwise vorticity fluctuations (negative vorticity represented using bold) [16]	9
2.4	Coherent vortex structures over a rod (Image source: [18])	9
2.5	Illustration of generic upstream section for an engine operating under Boundary Layer Ingestion	10
2.6	Coordinate system used in the analytical study of rotating disk by Kobayashi et al. (Image source: [20])	10
2.7	Flow over a disk rotating at 1800 RPM (Image source: [20])	11
2.8	Cross section of spiral vortices for disk rotating at 1200 rpm (Image source: [21])	11
2.9	Geometry used for the theoretical work carried out by Kobayashi (Image source: [23])	12
2.10	Variation of number of spiral vortices (n) against half angle of cone (θ) (Image source: [1])	13
2.11	Flow pattern and vortices over a 15° half angle cone rotating at 3500 RPM in still fluid (Source of images: [1])	13
2.12	Flow pattern and vortices over a 15° half angle cone rotating at 670 RPM and an inflow velocity of 1.7 m/s (Source of images: [2])	14
2.13	Variation of Reynolds number (both critical, $Re_{x,c}$ and transitional, $Re_{x,t}$) with rotation ratio (S) (Image source: [2])	14
2.14	Variation of number of spiral vortices (n) with rotation ratio (S) (Image source: [2])	15
2.15	Development of spiral vortices in the transition regime. Rotation Rate : 785 RPM Inflow velocity : 1.85 m/s (Image source: [24])	23
2.16	Variation of number of spiral vortices with local rotation ratio for different cone apex angles (Image source: [25])	24
2.17	Ogive configuration implemented by Degani and Schiff (Image source; [30])	24
2.18	Mesh used for the numerical simulation of the ogive (Image source: [30])	24
2.19	Helicity density contours. Mach number = 0.8, angle of attack = 40° and diameter based Reynolds Number = 200,000. Jet = 0% (Image source: [30])	25
2.20	Helicity density contours. Mach number = 0.8, Angle of attack = 40°, Diameter based Reynolds Number = 200,000. Jet = 1.2 % at $x/D \approx 1.2$ (Image source: [30])	25
2.21	Helicity density contours. Mach number = 0.8, Angle of attack = 40°, Diameter based Reynolds Number = 200,000. Jet = 1.2 % at $x/D \approx 0.12$ (Image source: [30])	25
2.22	Comparison of instantaneous spanwise vorticity (Image source: [31])	26
2.23	Experiment setup schematic (Image source: [3])	26
2.24	Instantaneous surface temperature footprints of spiral vortices under axial inflow (Image source: [5])	27
2.25	Instantaneous surface temperature footprints of spiral vortices under non-axial inflow with incidence angle: 2° (Image source: [5])	27
2.26	Instantaneous contour plots of wall normal velocity fluctuations under axial inflow (Image source: [5])	27
2.27	Instantaneous contour plots of wall normal velocity fluctuations under non-axial axial inflow (4° incidence angle) for windward (left image) and leeward (right image) meridians (image source: [5])	28
2.28	Convex geometry used by Karp and Hack (Image source: [13])	28

2.29	Linear DNS showing streamwise streaks using isosurfaces of 0.01 times the maximum streamwise velocity disturbance. Left to right flow. Red signifies positive disturbance and blue negative. (Image source: [13])	28
2.30	Variation of Stall criterion with Diffusion parameter (Image source: [6])	29
3.1	Illustration depicting a fluid element (Image source: [49])	32
3.2	Division of length scales for High Reynolds Number flows	34
3.3	Use of two different filters for the Germano model	37
4.1	Workflow in setting up simulations	42
4.2	Illustration of geometry considered	43
4.3	Illustration of blocking method implemented	44
4.4	Front views of the mesh	45
4.5	Side views of the mesh	45
4.6	Mesh metric histograms	46
4.7	Overview of boundary conditions	46
4.8	Probes for measurement of variations in velocity components and pressure	47
4.9	Case 2 - Mesh 1 - Pressure variation at both probe locations	47
4.10	Case 2 - Mesh 1 - U component velocity variation at both probe locations	48
4.11	Case 2 - Mesh 1 - V component velocity variation at both probe locations	48
4.12	Case 2 - Mesh 1 - W component velocity variation at both probe locations	49
4.13	Representation of angle of attack (α)	50
5.1	Instantaneous contour plots of C_f	52
5.2	T_u (%)	52
5.3	Illustration of LES scale separation	53
6.1	User defined local coordinate system	55
6.2	Mesh 1 - Instantaneous (C_f) contours (Instantaneous physical time = 0.1 s and 0.13 s)	62
6.3	Mesh 1 - Instantaneous (C_f) contours (Instantaneous physical time = 0.15 s and 0.2 s)	63
6.4	Mesh 1 - Wall normal velocity fluctuation Contour	64
6.5	Axial locations for velocity profiles	64
6.6	Mesh 1 - Velocity Profile	65
6.7	Mesh 1: Wall parallel transient average velocity contour	65
6.8	C_f fluctuation profile	66
6.9	Meridional Trace of Γ'_{RMS} [5]	66
6.10	Critical point Mesh 1	67
6.11	Mesh 1 - Local Reynolds Number variation with local rotation ratio	67
6.12	Mesh 2 - Instantaneous Wall Friction Coefficient Contours (t = 0.1 s and 0.13 s)	68
6.13	Mesh 2 - Instantaneous Wall Friction Coefficient Contours (t = 0.15 s and 0.2 s)	69
6.14	Mesh 2 - Wall normal velocity fluctuation Contour	70
6.15	Mesh 2 - Wall Parallel Transient Mean Velocity Profile	70
6.16	Mesh 2: Wall parallel transient average velocity contour	71
6.17	Wall normal velocity fluctuations	72
6.18	Mesh 2: Local Reynolds Number Variation with local rotation ratio (Re_l Vs S)	73
6.19	C_f variation in Y/D	73
6.20	n vs S	74
7.1	Velocity magnitude vectors (in red) showing effect of incidence of flow upstream over cone	75
7.2	Velocity magnitude vectors (in red) showing effect of incidence of flow near the inlet	76
7.3	Velocity magnitude vectors (in red) showing effect of incidence of flow near the outlet	76
7.4	Velocity magnitude vectors (in red) showing effect of incidence of flow at the side walls	77
7.5	Illustration of windward and leeward side of cone	77
7.6	Instantaneous C_f contours (physical timestep = 0.15s)	78
7.7	Wall normal velocity fluctuations	79
7.8	Counter rotating vortices for axial and non-axial case at instantaneous physical time of 0.15s	79
7.9	Fluctuating C_f v/s X/D for non axial inflow	80

7.10 Fluctuating C_f (moving mean) profile v/s X/D for both axial and non axial inflow	81
7.11 Non Axial - Re_1 vs S (Windward Meridian)	82
7.12 Non Axial - Re_1 vs S (Windward Meridian)	83
7.13 V velocity variation in time at 2 probe locations	83
7.14 Leeward meridian: Wall parallel velocity profile ($\alpha = 2^\circ$)	84
7.15 Windward meridian locations for velocity profile	84
7.16 Windward meridian: Wall parallel velocity profile ($\alpha = 2^\circ$)	85
7.17 Leeward transient velocity contour	85
7.18 Windward transient velocity contour	86
7.19 N vs S	86
A.1 Coordinate system following the body profile [10]	93

List of Tables

4.1	Dimensional and non-dimensional parameters used to define the numerical model	43
6.1	Discretization Effect	60
7.1	Non-Axial case - Spatial distribution of n ($\alpha = 2^\circ$)	81
C.1	A_j coefficients in ANSYS CFX [51]	97

Introduction

Intuitively, the first thing which comes to mind upon encountering the word vortices, is something akin to the spirals seen in "The Starry Night" (figure 1.1), a famous painting by Vincent van Gogh. Such motions are seen across every aspect of mother nature. From the rotating motion of plasma over the surface of a star to the water spiralling into the drain of a sink. Understanding the various traits of vortices has been a topic of intensive study throughout history.



Figure 1.1: "Starry Night" - Vincent van Gogh¹

Somewhere in between these two extremes, laboratory experiments using air (details in chapter 2) have found the formation of vortices over rotating cones under the influence of still flows (Kobayashi et al. [1]), axial inflows (Kobayashi et al. [2], Tambe et al. [3], Tambe et al. [4]) and non-axial inflows (Tambe et al. [5]). The formation of these observed vortices is yet to be seen through numerical experiments and research into this has potential industry impacts, explained in the following paragraphs.

Although significant strides have been made to increase the fuel economy in aircraft using modern technologies, the room for improvement remains large. Modern turbofan engines implement a higher bypass ratio to

¹<https://www.vangoghgallery.com/painting/starry-night.html>

reduce specific fuel consumption. The flip side is the increase in the nacelle weight and drag. If the nacelle length is reduced to compensate, the performance of the fan is compromised due to the losses generated by the non-axial inflow and separation at the blade hub junction [6]. To overcome such issues many aircraft design innovations have been suggested. One such example is by the National Aeronautics and Space Administration (NASA) which would use the boundary layer formed over the fuselage of an aircraft as inflow. This is known as a Boundary Layer Ingestion (BLI) engine. Various vehicle concepts such as STARC-ABL, D8 and N-3X amongst others have been proposed (Hendricks [7]).

Urunga et al. [8], worked on providing a good initial sense of the advantages gained by using BLI engines for civil aviation. Their experimental work on the D8 configuration (figure 1.2) shows promise even though the research is in its primitive stage.



Figure 1.2: D8 Configuration²

The rotating cone referred to in the title, can be considered to be an idealised model of an aero-engines spinner (Tambe et al. [5]). The boundary layer profile formed over the spinner affects the velocity distribution over the fan and thus affects the evaluation of the losses generated.

For flow to transition from laminar to turbulent, small perturbations grow rapidly in time leading to unpredictability in the flow. This behaviour is called *deterministic chaos* and is a trait of turbulent motion (Westerweel et al. [9]). For an initial analytical study of the transition process, a common method is the linear stability analysis (theory in appendix B). Flows along curved surfaces are subjected to centrifugal forces due to changes in direction and this displaces the particles from their equilibrium position.

Experiments in the past have been conducted over rotating cones with varied half angles, rotating speeds and inflow conditions. These counter-rotating small wavelength perturbations have been observed in the transition region over the rotating cones (Figure 1.3) and the above mechanism has been studied in great detail by previous researchers. The spatial distribution of these vortices have also been studied (details in chapter 2). Recent experiments on non-axial inflow over rotating cones have also been undertaken by Tambe et al. [5] (detailed discussion in chapter 2). The need for numerical simulations arises due to the application area of this research field.

To study the hub-corner separation in detail, it is important to check the capability of existing numerical simulation techniques in the prediction of the boundary layer transition and flow development over a rotating nose-cone.

Numerical studies also provide multiple advantages over an experimental one. The essence of numerical simulations lies in its principle. A computer code being capable of capturing complex flow phenomena makes its use accessible remotely as well. In addition to this, studying the various effects of mother nature is also easier. As an example, to study the different effects of laminar and turbulent flow, the user in a numerical

²<https://www.nasa.gov/content/the-double-bubble-d8-0>

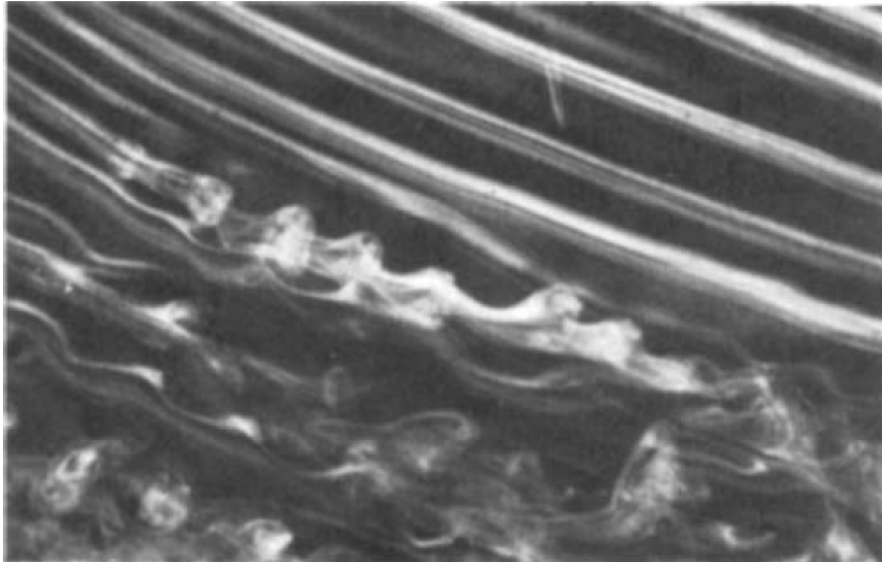


Figure 1.3: Transition process observed over cone rotating at 700 rpm and axial inflow of 2.9 m/s (Image source: [2])

simulation need only switch between the different available turbulence models and the laminar model. In the case of experiments, studying this is tricky. CFD simulations provide the user to study different effects of different initial and boundary conditions while keeping all other parameters constant with remarkable accuracy. Maintaining such consistency will require a great deal of skill from the experimentalist and even then achieving this would be extremely difficult. Successful CFD simulations will motivate studies in this field to move beyond academia and provide real-world applications.

1.1. Report Structure

The thesis is structured as follows. A theoretical background along with some of the early and recent work covered in the field of flow over axis-symmetric bodies are given in chapter 2. Following the literature review, chapter 2 also states the research question and objectives. Chapter 3 provides the reader with an introduction into turbulence modelling and various techniques available in the numerical simulation of turbulent flows. The methodology applied in this thesis to model the flow phenomenon over rotating cones under axial and non-axial inflows is given in chapter 4. This chapter includes the geometry creation, meshing and model setup. The results from the Unsteady Reynolds Averaged Navier Stokes (URANS) simulations for an axial inflow are presented in chapter 5. The results from the subsequent Large Eddy Simulation (LES) for the axial inflow is discussed in chapter 6. The final set of results from the non-axial simulations are discussed in chapter 7. Completing the report, the conclusions derived from the simulations and the suggested recommendations by the author are provided in chapter 8.

2

Literature Review

This chapter can be broken down into two parts. This begins with a brief description of general equations governing the flow over axis-symmetric bodies, followed by a general discussion on the instabilities involved in such flows. The effect of an engine operating under BLI on the flow is also discussed (section 2.1).

The second part delves into the description of previous experimental, numerical and analytical work carried out to study the flow over axis-symmetric bodies along with defining the research question for this thesis (section 2.2 - 2.5).

2.1. Theoretical Background

2.1.1. Flow over Axis-symmetric bodies

The inflow conditions for spinners in BLI engines will be highly viscous and involve transition from laminar to turbulent flow over the body itself. Thus, it is important to gain an understanding of how the general flow would develop over it. The contents of this section are based on the book by Schlichting et al. [10].

A generic axis-symmetric geometry is shown in figure 2.1. As shown, the x coordinate, in this case, is the arc length measured from the tip (stagnation point). y coordinate is therefore the wall-normal direction and z the circumferential direction. A function $r_w(x)$ ¹ may be used to define the shape of the body.

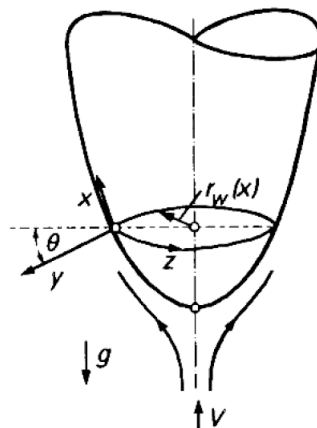


Figure 2.1: Generic axis-symmetric geometry (Image source: [10])

The velocity components over this cone will likewise be, u , v and w , where, u is the velocity along the meridian, v is the wall normal velocity and w is the velocity in the wall circumferential parallel direction. The potential flow velocity above the boundary layer is considered to be $U(x)$.

¹ $r_w(x)$ is the radius of an arbitrary section of the body normal to the axis

Assuming that the boundary layer formed over the body is thin compared to the radius (i.e. $\delta \ll r_w$) and for the Reynolds Number (Re) $\rightarrow \infty$ ($Re = Ul/\nu$ where l is the radius of curvature near the stagnation point and ν is the kinematic viscosity of the fluid) and there are no thermal effects, the boundary layer equations may be written,

$$\begin{aligned} \frac{\partial(r_w \rho u)}{\partial x} + \frac{\partial(r_w \rho v)}{\partial y} &= 0 \\ \rho(u \frac{\partial u}{\partial x} + v \frac{\partial u}{\partial y}) &= -\rho g \sin(\alpha) - \frac{dp}{dx} + \frac{\partial}{\partial y}(\mu \frac{\partial u}{\partial y}) \end{aligned} \quad (2.1)$$

Here, α represents the angle of inclination with respect to the horizontal at a certain position x . In this coordinate system, $\alpha = \theta + \pi/2$. The pressure gradient ($\frac{dp}{dx}$) is given by :

$$\frac{dp}{dx} = -\rho_e U \frac{dU}{dx} \quad (2.2)$$

e indicates the outer edge of the boundary layer. For this case $U(x) = u_e(x)$.

To appreciate the salient features of equation 2.1, a comparison should be made to the plane boundary layer equations (plane flows refer to flows in which all streamlines are in parallel planes),

$$\begin{aligned} \frac{\partial(\rho u)}{\partial x} + \frac{\partial(\rho v)}{\partial y} &= 0 \\ \rho(u \frac{\partial u}{\partial x} + v \frac{\partial v}{\partial y}) &= -\rho g \sin(\alpha) - \frac{dp}{dx} + \frac{\partial}{\partial y}(\mu \frac{\partial u}{\partial y}) \end{aligned} \quad (2.3)$$

The derivation for equation 2.3 is provided in appendix A.

When equation 2.1 and 2.3 are compared, it is evident that they are very similar and indeed only the continuity equation has changed. The introduction of the geometrical parameter ($r_w(x)$) for the axis-symmetric body is the only difference between those two equations. This leads to the requirement of having both the geometry and the velocity functions to define the boundary layer equations as given in equation 2.1.

Rewriting the continuity equations of 2.1 and 2.3 in a generic form :

$$\frac{\partial(r_w^j \rho u)}{\partial x} + \frac{\partial(r_w^j \rho v)}{\partial y} = 0 \quad (2.4)$$

If $j = 1$, equation 2.4 refers to the continuity equation from the axis-symmetric case and the plane case for $j = 0$.

For a rotating body, there is an additional flow component in the azimuthal direction due to the no-slip boundary condition. This velocity component reduces within the boundary layer in the wall-normal direction. The flow will remain axis-symmetric as depicted in figure 2.1. The effect of this additional component is seen when re-writing equation 2.1:

$$\begin{aligned} \frac{\partial(r_w \rho u)}{\partial x} + \frac{\partial(r_w \rho v)}{\partial y} &= 0 \\ \rho(u \frac{\partial u}{\partial x} + v \frac{\partial v}{\partial y} - \frac{\mathbf{w}^2}{r_w} \frac{d\mathbf{r}_w}{d\mathbf{x}}) &= -\rho g \sin(\alpha) - \frac{dp}{dx} + \frac{\partial}{\partial y}(\mu \frac{\partial u}{\partial y}) \\ \rho(u \frac{\partial w}{\partial x} + v \frac{\partial w}{\partial y} + \frac{uw}{r_w} \frac{dr_w}{dx}) &= \frac{\partial}{\partial y}(\mu \frac{\partial w}{\partial y}) \end{aligned} \quad (2.5)$$

The bold term in equation 2.5 refers to the "coupling term" added to equation 2.1.

2.1.2. Flow Instabilities

The previous section introduced the boundary layer equations defining the flow over axis-symmetric bodies. It is also important to gain an insight into the types of instabilities one might encounter when dealing with such complex flows. This section will thus give a short background into the theory of those different flow instabilities defining this study.

Flows along curved surfaces are subjected to centrifugal forces due to the change of direction of fluid motion. On account of these forces, a particle is displaced from its equilibrium position. Such instabilities were first shown in 1923 by Taylor [11] between two concentric rotating cylinders and for certain cases, the flow between these two cylinders turned unstable and formed pairs of counter-rotating vortices.

The centrifugal effects are broadly categorised as :

- Wall curvature induced changes in the turbulent flow structures
- Longitudinal vortices formed (secondary flow)
- Secondary flows generated affecting the turbulent flow structures

The note begins with the Görtler instabilities, i.e. the longitudinal secondary flow.

Görtler Instability

Görtler [12] first showed these types of instabilities which would occur in the boundary layer over curved walls. Such instabilities were shown to occur when the Görtler number, defined as,

$$G = \frac{U_\infty \delta_r}{\nu} \left(\frac{\delta_r}{R_g} \right)^{1/2} \quad (2.6)$$

was greater than a critical value. δ_r is the boundary layer thickness, U_∞ is the free stream velocity, R_g^2 is the radius of curvature of the wall and ν is the kinematic viscosity.

Görtler instabilities are phenomena induced by geometry and thus depend on the complete flow rather than just the geometry of the body. The study of these instabilities remains an active area. Floryan [14] gives an excellent review of the work carried out up to 1991, on this subject.

Streamline Curvature Effects

Turbulent flows are highly affected by the curvature in the geometry and any rotational effects for rotating bodies. This extra rate of strain has a greater impact than any other extra terms appearing in the equations of motion. In a comprehensive review of the work carried out on longitudinal curvature effects, Patel et al. [15] mention that experiments have shown there to be a direct impact of curvature on the Reynolds stresses.

The focus here is however on transverse curvatures. These are basically wall curvatures in planes perpendicular to the direction of oncoming flow. With a boundary layer not subjected to pressure gradient in the axial direction, the transverse curvature effects remain isolated.

An excellent review on this was done by Piquet and Patel [16] in 1999. Their review revolved around experiments conducted on axial flows over a cylinder. The review concluded that the effect of curvature is minimal when the Reynolds number is large and the boundary layer formed over the cylinder is thin. However, at smaller Reynolds number and thicker boundary layer, the effects of transverse curvature are present across the entire boundary layer along with the relaminarisation of the flow.

Figure 2.3 represents the longitudinal vorticity contours obtained from a Direct Numerical Simulation (DNS). Large scale structures are seen wrapped around the body. One other fundamental case which comes up in such studies, is the presence of large boundary layers under high Reynolds number condition, Piquet et al. [16] mentions that there has been little study in that area and recommends Large Eddy Simulations (LES) to gain further knowledge of the interaction between the smaller wall-bounded eddies with the larger eddies seen in figure 2.3.

²Here the subscript g is used to prevent confusion with Karp et al [13] having used R without the subscript

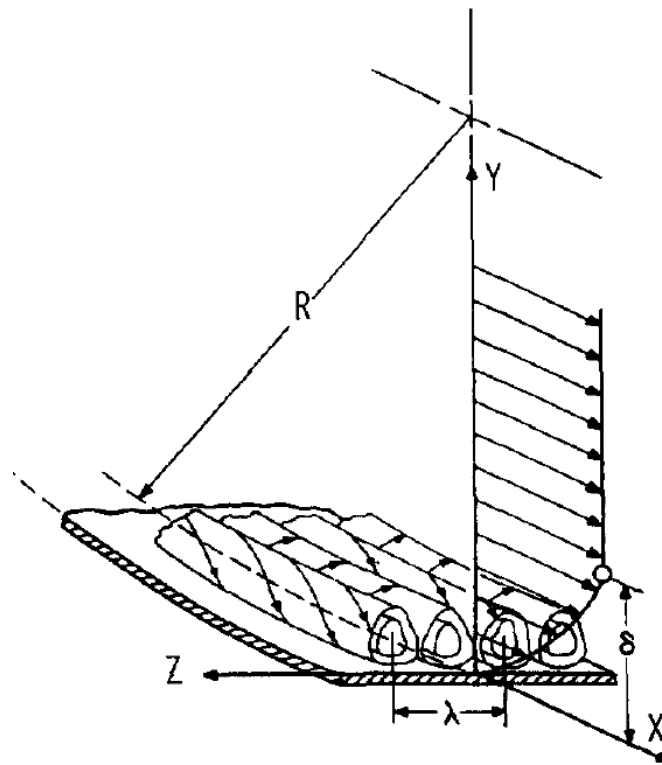


Figure 2.2: Disturbances in the boundary layer of flow over curved surfaces (Image source: [14])

2.1.3. Secondary Flow Structures

The presence of three dimensions significantly affects the flow structures and simple extrapolation of 2D theory does not depict accurately the three dimensional turbulent structures formed.

Consider a cartesian coordinate system, with x in the streamwise direction, y being normal to the wall and z being in the spanwise direction. Vorticity may be generated via different mechanisms (Bradshaw [17]) :

- Quasi inviscid deflection of existing mean vorticity
- Reynolds stresses generating stress induced vorticity

Cross flows (axial vorticity in the gradient of spanwise velocity normal to the wall) and streamwise vorticity can be generated by either mechanisms. Presence of significant effects of Reynolds stresses when identifiable vortices are formed. Bradshaw [17] in 1987 reviewed these turbulent flows having mean streamwise vorticities and concluded that numerical simulations of eddy motions may provide the detailed pressure fluctuation statistics and reproduce these complex flow phenomena.

Chang and Tavoularis [18] worked on Unsteady Reynolds Average Navier Stokes (URANS) simulations of an axial flow over a cylinder inside a rectangular domain. Figure 2.4 depicts the resolved velocity fields (which are strongly time dependant) using Q criterion (section 2.4.3) showing the quasi periodic vortical coherent structures on either side of the rod.

2.1.4. Effect of Boundary Layer Ingestion

The primary application area of this research work is for its use in Boundary Layer Ingestion. It is thus important to discuss the effect of an engine operating under this concept, on the flow upstream of the spinner and fan.

A boundary layer ingestion engine, as the name suggests, operates using the boundary layer as its inflow. This is different from conventional engines which are placed away from the fuselage and work only with clean air



Figure 2.3: Normalised streamwise vorticity fluctuations (negative vorticity represented using bold) [16]

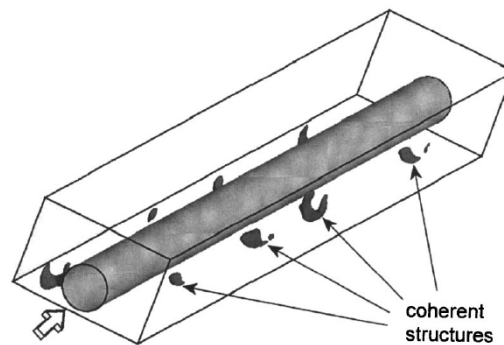


Figure 2.4: Coherent vortex structures over a rod (Image source: [18])

inflow. The boundary layer over a fuselage is an energetic and viscous zone and this detail affects the flow development.

The flow upstream would result in a non-axial flow over the spinner. This process is explained in the following way. Consider figure 2.5a, the shaded region represents the small distorted boundary layer zone as inflow through the inlet of the engine. The rest of the region can be represented as being non-distorted.

Under the influence of clean flow, the stagnation point over the spinner would have been at the centre. Due to the presence of distortion, this would change. The reason for this is that the clean part of the flow (nonshaded region) would have a higher static pressure compared to the distorted section. Thus, this induces some of the clean flow to migrate towards the distorted section (Fidalgo et al. [19]). Figure 2.5b illustrates this using streamlines. It is easier to model flow with non-axial inflow than imposing a distorted section and thus this study will hope to serve as a starting point for future numerical studies on non-axial flows over rotating axis-symmetric bodies.

2.2. Early Studies

Kohama and Kobayashi worked on the formation of spiral vortices over rotating disks [20]. Their work focused on both theoretical and experimental studies. Experiments on rotating disks involved still fluids and for the theoretical approach, they included the effects of Coriolis force and streamline curvature into the linear stability analysis (a description of the general method involved in linear stability analysis is given as part of appendix B) to obtain the critical Reynolds number at the onset of instabilities. For their analytical study, the Reynolds number was defined as:

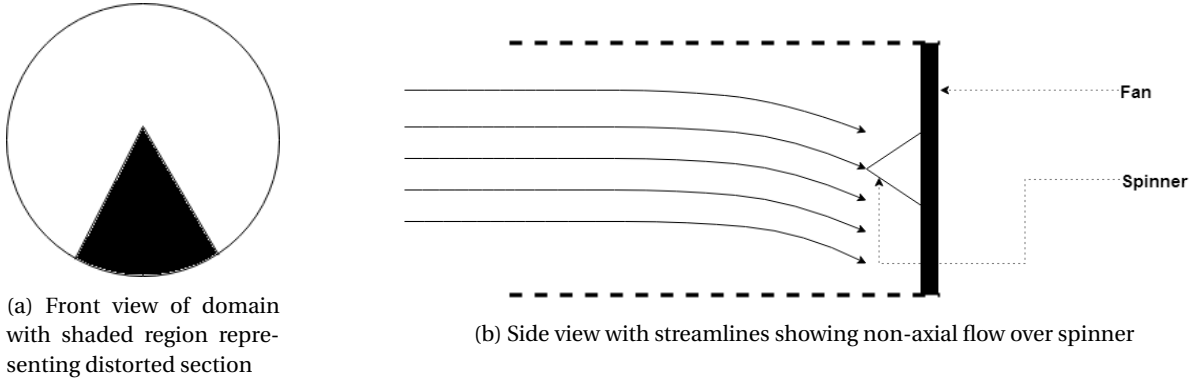


Figure 2.5: Illustration of generic upstream section for an engine operating under Boundary Layer Ingestion

$$Re = \frac{r_0 \omega \delta^*}{\nu} \quad (2.7)$$

Here, δ^* is the displacement thickness of the laminar boundary layer based on the circumferential boundary layer. They evaluated this to be:

$$\delta^* = 1.271 \sqrt{\frac{\nu}{\omega}} \quad (2.8)$$

ω is the rotational velocity of the plate, ν is the kinematic viscosity and r_0 is the distance from the origin to a new proposed orthogonal coordinate system. The origin (O') of this is fixed relative to the rotating plate with x' and y' set along with a pair of logarithmic spirals. This coordinate system is shown in figure 2.6.

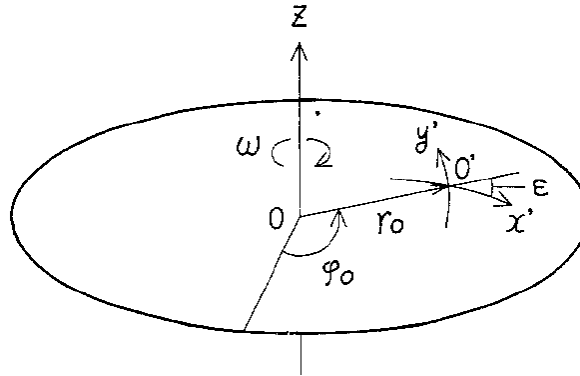


Figure 2.6: Coordinate system used in the analytical study of rotating disk by Kobayashi et al. (Image source: [20])

To validate the findings, a hot wire probe was used as the experimental tool. Kobayashi et al. [20] also studied the effects of variation of the rotation rate (disk rotation speed was varied constantly up to 1880 RPM). An example of the flow over such a geometry visualised in their experiments is shown in figure 2.7. The spiral vortices are observed to be in the transition regime.

For the experiments by Kobayashi et al. [20], flow patterns were observed using radially applied $TiCl_4$ applied over black painted rotating disk. The motion of white gas would then be used to visualise the flow. The Reynolds number from the experiments, Re_1 was defined as $Re_1 = r^2 \omega / \nu$ and thus, $Re = \sqrt{1.616 Re_1}$.

The findings from the experiments conducted by Kobayashi et al. [20] can be listed below:

- Critical Reynolds Number ($Re_{1,c}$) was around 8.8×10^4 and the transition Reynolds number ($Re_{1,t}$) was 3.2×10^5
- Average of 31 to 32 spiral vortices developed over the disk and increased radially

- The critical Reynolds number obtained using the theoretical approach was 6.8×10^4

Vortex branching was given as the cause for this increase in the number of vortices. The reason behind the approximately 22% difference between the theoretical and experimental value was not given, but may be attributed to the shortcomings of the linear stability theory. The authors (Kobayashi et al. [20]), however, mention that this difference is 15% lower than the difference in previous studies.

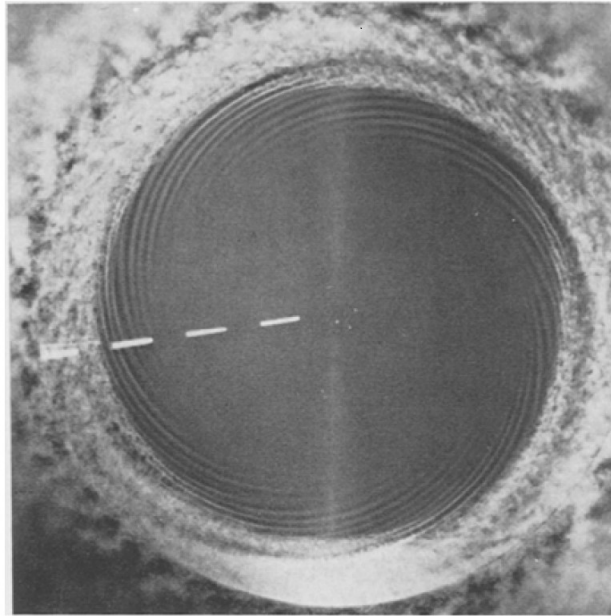


Figure 2.7: Flow over a disk rotating at 1800 RPM (Image source: [20])

Kohama [21] conducted experiments to study the transition process involved in the above research. The main conclusions he drew from his study are listed below:

- Co-rotating spiral vortices with respect to its neighbours
- Structure similar to ones observed on a rotating sphere (Kohama and Kobayashi [22] worked on rotating spheres)

Kohama [21] showed the cross-sectional image of the vortices in the transition region, for a lower angular velocity of the disk (figure 2.8).

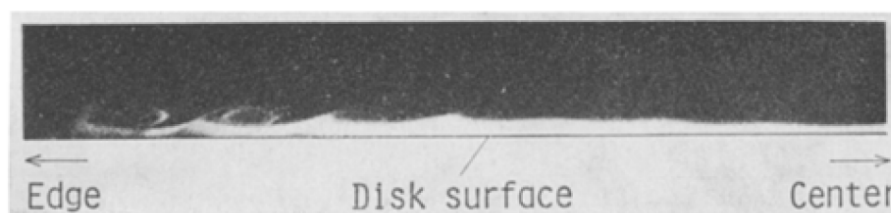


Figure 2.8: Cross section of spiral vortices for disk rotating at 1200 rpm (Image source: [21])

The above study is a special case for flow over conical geometries (cones with half angle 90°). Some early theoretical work on rotating cones was carried out by Kobayashi [23]. Linear stability theory was used to develop the perturbation equations for an incompressible boundary layer over a cone under axial inflow rotating at a constant velocity. The small perturbations were assumed to be spiral vortices. The coordinate system used for this study is shown in figure 2.9. A curvilinear coordinate system (x' , y' and z') was used, where x' is aligned in the direction of propagation of the spiral vortices and y' aligned along the axis of the vortices, making them

orthogonal to each other (a similar coordinate system will be found later in many studies). A local rotational speed ratio (S) was defined as,

$$S = \frac{R_0 \omega}{U_e} \quad (2.9)$$

where, R_0 is the radius at the origin o' , ω is the rotational velocity of the cone and U_e is the meridional velocity at the outer edge of the boundary layer over the cone. This was seen to have an important influence on the instabilities.

Conclusions drawn from the study by Kobayashi [23] were :

- Perturbation equations developed include velocity components in both x' and y' directions for the rotating case as compared to the Orr-Sommerfeld equations governing the non-rotating cone'
- The critical and transition Reynolds number obtained for a test case (total cone angle: 30° and $S = 3$) were consistent with experiments

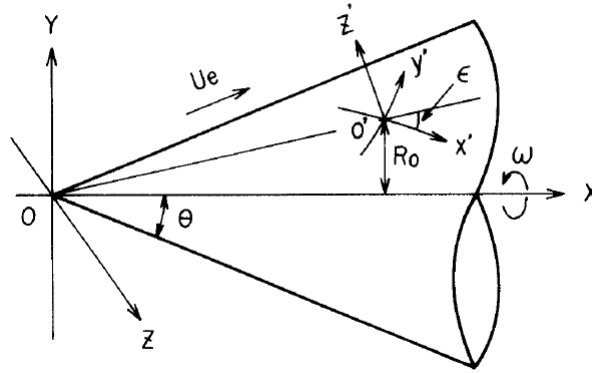


Figure 2.9: Geometry used for the theoretical work carried out by Kobayashi (Image source: [23])

Experimental work were carried out on a conical geometry by Kobayashi and Izumi in 1983 [1] under conditions of still flow. The critical and transitional positions (\bar{x}_c ³, \bar{x}_t ⁴) were measured and based on that the critical and transitional Reynolds numbers were calculated. Defined in their research as, $Re_{x,c} = \omega \bar{x}_c^2 \sin^2 \theta / \nu$ and $Re_{x,t} = \omega \bar{x}_t^2 \sin^2 \theta / \nu$. A parametric study of the cone angle was undertaken (varied from total included angle of 30° to 150°). They concluded the following :

- Counter rotating pair of spiral vortices for cones of half angle 15° whereas co-rotating vortices observed for rotating disks
- The critical and transitional Reynolds number increases with the increase in the cone angle
- The average number of spiral vortices increases from 22 - 23 for a cone with half angle of 45° to one with 90° (case of rotating disk) as shown in figure 2.10

Kobayashi and Izumi [1] found the spiral vortices change constantly with increasing half angle of the cone. The reason for this change was not given. They also conducted a theoretical analysis (using linear stability theory) and found differences in the critical and transitional Reynolds number with those found in experiments. The difference was chalked down to complicated flow disturbances not accounted for in the former.

³Critical position for the experiments by Kobayashi et al. [1] was the point where periodical signals from the hot-wire probe were detected at a certain frequency in a frequency spectrum

⁴Transitional position for the experiments by Kobayashi et al. [1] was the point where velocity fluctuations gave a frequency spectrum for the turbulent boundary layer

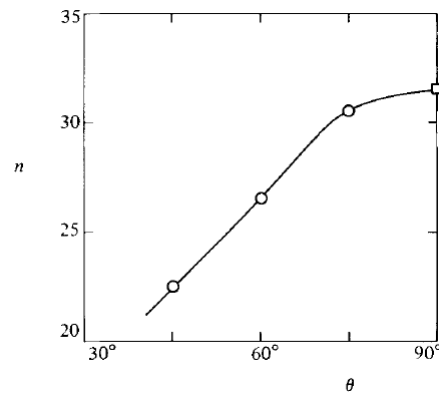


Figure 2.10: Variation of number of spiral vortices (n) against half angle of cone (θ) (Image source: [1])

Figure 2.11 shows the flow pattern developed over one such cone (half angle 15° rotating at 3500 RPM). Figure 2.11a shows the general flow pattern developed over the cone and figure 2.11b shows the cross sectional view of the spiral vortices developed over the same cone.

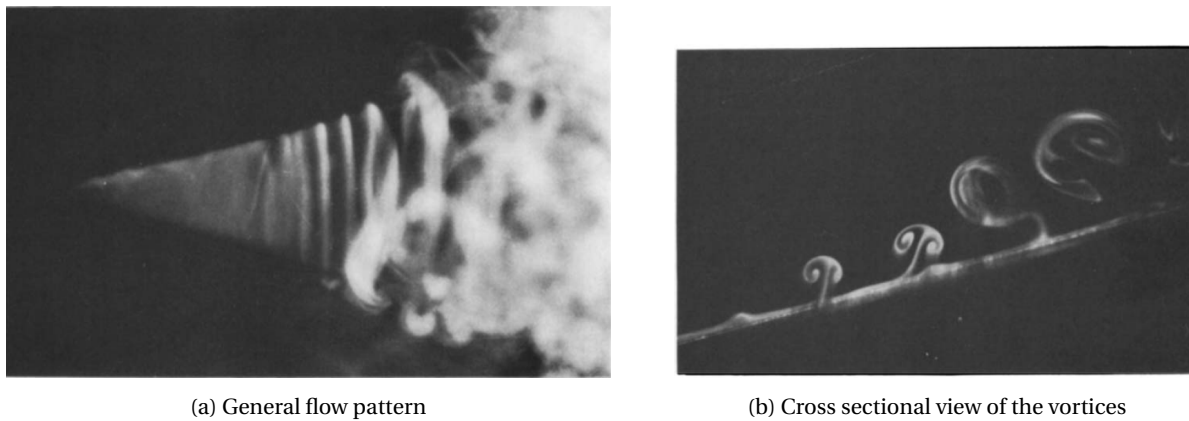


Figure 2.11: Flow pattern and vortices over a 15° half angle cone rotating at 3500 RPM in still fluid (Source of images: [1])

Kobayashi et al. [2] continued the experimental work on flow over conical bodies to study the transition laminar to turbulent transition regime. This work made an increment on the previous work by Kobayashi et al. [1] having included an external axial flow in the setup.

The experiments by Kobayashi et al. [2] involved a 15° half angle rotating cone with the study using the coordinate system defined in figure 2.11b. Similar to previous studies, the theoretical approach involved linear stability analysis and the small scale disturbances were assumed to be spiral vortices. The turbulence intensity ($I = \sqrt{u'^2}/U_\infty$), u' is the longitudinal velocity perturbations and U_∞ is the free stream velocity) in the inflow varied from 0.05 % to 0.15 % for U_∞ from 1 m/s to 14 m/s.

The experiments by Kobayashi et al. [2] visualised the flow (figure 2.12a) using TiCl_4 spread over the surface of a black painted cone. The spiral vortices are observed in the transition region. The experiments also showed that increasing the rotational speed of the cone, shifts the transition region closer to the tip. A cross section of the spiral vortices for the same rotation rate and inlet flow is shown in figure 2.12b.

The study concluded the following :

- The theoretical work showed the importance of the rotation ratio, S (defined earlier in equation 2.9) on the critical Reynolds number
- The critical and transitional Reynolds number decrease with increasing S (figure 2.13)
- Their theoretical approach under-predicted the Reynolds number values

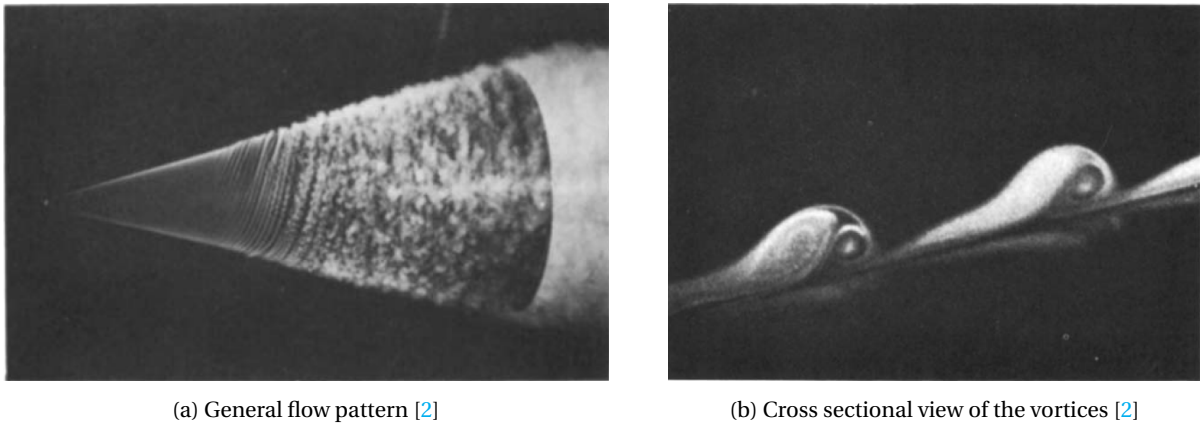


Figure 2.12: Flow pattern and vortices over a 15° half angle cone rotating at 670 RPM and an inflow velocity of 1.7 m/s (Source of images: [2])

- The number of spiral vortices (n) reduce with increasing S (figure 2.14)

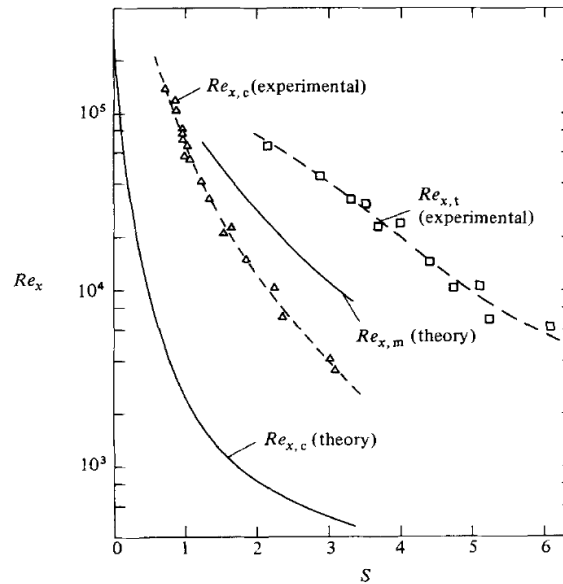


Figure 2.13: Variation of Reynolds number (both critical, $Re_{x,c}$ and transitional, $Re_{x,t}$) with rotation ratio (S) (Image source: [2])

Kobayashi et al. [2] showed that at higher rotation ratios, the major instability factor is the centrifugal instabilities (Taylor instability is an example). This was concluded by examining figure 2.13 and the known fact that theoretical predictions of critical Reynolds number tend to agree with those with experiments for the centrifugal instabilities. Figure 2.13 shows that the difference between the theoretical and experimental prediction of the Reynolds number decrease with increasing S .

Kohama, Y. [24] experimentally studied the behaviour of these vortices observed in the above mentioned work. Another 15° half angle cone was taken and rotated under an axial inflow. The coordinate system employed in this case is once again similar to the one shown in figure 2.9. This work aimed to study the transition process and the development of the observed vortices during this process. These vortices were observed in a time dependant series of frames to aid the visualisation of the growth and breakdown process.

This transition process studied by Kohama [24] can be summarised in the following phases :

- Curling Period: Steep velocity profiles observed in the laminar boundary layer wherein these spiral vortices grow under centrifugal forces of certain frequency

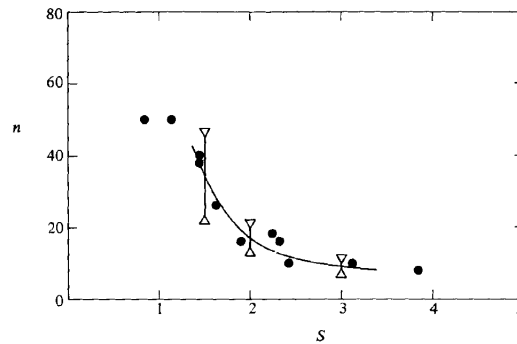


Figure 2.14: Variation of number of spiral vortices (n) with rotation ratio (S) (Image source: [2])

- **Prominence Period:** Rapid growth in all three directions. Average growth rate (wrt the mean velocity field) of 6%, 1.4% and 14% in the z , y and x direction respectively. It was suspected that the vortices affect the mean velocity profiles forming Tollmien-Schlichting type instabilities. These vortices are strongly decelerated in the curling period and the head portion of the vortex is stretched in the downstream direction
- **Decay Period:** The vortices are torn off and the boundary layer completes its transition to a turbulent one

Figure 2.15 shows a series of photographs taken by Kohama [24] and illustrates in wonderful detail the process described above.

Kohama [24] also concluded that the boundary layer turns unstable due to the following actions of the vortices in addition to the mixing of fluids due to the inflow of flow from outside the boundary layer :

- Curling motion of the vortices accelerating the mixing of fluids with different velocities in a narrow space
- Rapid growth in the z direction during the second phase promoting mixing of high and low velocity fluids in the shear layer
- Horse-shoe type vortices towards the end of the second phase extending the mixing region in the z direction

Kobayashi et al. [25] further worked (experimentally) on these rotating cones under axial inflow with a parametric study of the cone angles and free stream turbulence intensity. They conducted experiments on three different cones with total included angles of 15° , 30° and 60° . The meridian length of these cones were 172.7 mm (for the 30° total angle) and 200 mm (for the other two). The default turbulence intensity (defined previously) in the test section was 0.04 %.

The main take-aways from the experiments by Kobayashi et al. [25] :

- The turbulence intensity did not have any impact on the transition Reynolds number. The critical Reynolds number, on the other hand, was highly sensitive to it and decreased with an increase in the intensity. They found that this sensitivity only increased with an increasing cone angle
- They also found that the number of spiral vortices only increased with increasing cone angle (figure 2.16) and the trend of decreasing number of these spiral vortices with increasing rotation ratio for rotating cones as found in earlier studies continued

A thorough review of such experimental work on different rotating bodies of revolution was done by Wimmer, M. [26] in 1988. This is an extensive review on the various experiments carried out on spheres, cones, disks and cylinders till then. The review includes studies of the initialisation and development of different types of instabilities (depending on the geometry) and is an excellent starting point for researchers wanting to gather an initial understanding of different flow features over different geometries and the experimental techniques used to visualise them.

William S. Saric and Helen L. Reed [27] reviewed some of the work done on trying to understand the origins of turbulent flow and transition over geometries such as swept wings, rotating disks, rotating cones and ellipsoids. Saric [28] also studied the disturbances induced by wall curvatures and specifically the Görtler vortices.

Kobayashi [29] reviewed the work done on flow transition from laminar to turbulent over various axis-symmetric bodies.

With all the studies noted above revolving around theoretical and experimental work, a related numerical study carried out in the later years of the 20th century was carried out by Degani and Schiff [30].

Degani and Schiff [30] showed the steady asymmetric vortex patterns on slender bodies of revolution. This study motivated by the yaw effects induced on slender bodies maneuvering at large angles of attack (under subsonic flow conditions), led the researchers to use two ogive configurations as shown in figure 2.17

A circumferential numerical grid was used for the simulation which would cover the entire geometry (shown in figure 2.18).

One of the most important factors in numerical modelling are the boundary and initial conditions imposed. To this, Degani and Schiff [30] used a no slip adiabatic wall on the surface of the cone and an undisturbed free stream inflow. Periodic boundary conditions were imposed at the circumferential edges of the mesh. The downstream boundary condition used zero axial gradient extrapolation and even though it is not valid for subsonic flow, as the wake generated behind the geometry will have a significant effect on the outlet, this was minimised by placing the outlet far downstream.

The free-stream conditions were allowed to be the initial flow field or a previous solution was used as the initial conditions and the solution was made to progress from that point. A constant global timestep was used. To break the symmetry of the flow, two weak jets, perpendicular to the plane of the angle of attack was imposed on the surface.

The results by Degani and Schiff [30] can be summarised in the following points:

- The computation study did not show the presence of asymmetry in the absence of symmetry breaking perturbations (helicity contours for one such case is shown in figure 2.19) unlike those in the experiments with which they compared their results
- To induce asymmetry in their computations, they introduced a jet with fixed strength of 0.1 % of the total normal force downstream ($x/D \approx 1.2$). Small asymmetry was observed (figure 2.20)
- They conducted an interesting numerical experiment in the above case. At a certain point of time during the simulation, they first switched off the jet (which generated the perturbations) and their solution regained symmetric flow conditions and in the other numerical experiment, they halved the jet strength at the same point of time and the solution reached a smaller point of asymmetry
- A perturbation upstream resulted in highly asymmetric flow over the ogive (figure 2.21)

They thus concluded that the degree of asymmetry was dependant on the point of application of the perturbations and the strength of the jets inducing these perturbations. They were successful in showing the existence of asymmetry in the flow forced due to spatially and temporally fixed disturbances.

Large Eddy simulation (LES) of the laminar-turbulent breakdown in a boundary layer flow over a cylinder was simulated by El-hady and Zang [31] in 1995. The flow considered was supersonic and validated using Direct Numerical Simulation (DNS) data.

Details to some extent on turbulence modelling using DNS, LES and Reynolds Averaged Navier Stokes (RANS) will be provided in chapter 3.

El-Hady and Zang [31] developed an LES model for such compressible flows and evaluated the model coefficients using the dynamic eddy viscosity subgrid-scale (SGS) models developed by Germano et al. [32] and Moin et al. [33].

The model developed was able to dynamically change the behaviour of the coefficients based on requirements, adjusting near the wall and capturing the asymptotic behaviour. To agree with DNS results, they used a trial and error approach to select the energy transfer rate from the larger to smaller scales. They were also successful in capturing the flow field over the transition regime using one-sixth of the grid resolution required in DNS. Figure 2.22 shows the predictions of the flow structure using spanwise vorticity.

2.3. Recent Studies

The previous section delved into the primary work done in this research field in the mid-late 20th century. This section gives a small review on some of the work carried out in this field in this century.

Garrett and Peake [34] studied the presence of absolute instabilities (instabilities which amplify locally) in the boundary layer over the outer surface of rotating cones under both still flow and axial flow conditions for a wide range of cone angles. The analysis also included viscosity and streamline curvature effects and within limitations of linear stability theory.

Their analysis revealed the following :

- Irrespective of still or non-zero axial inflow, the boundary layer is locally absolutely unstable over the entire range of cone angles
- Presence of axial inflow stabilises these absolute instabilities by delaying the onset of these instabilities to larger Reynolds numbers

On a more recent note (2019-2020), Tambe et al. [4], [3], [5] studied the formation of these boundary layer instabilities over a rotating cone and an ellipsoid under both axial and non-axial inflow.

A cone of half angle 15° and with a diameter of 47 mm was chosen. They conducted the experiments in the low speed W-Tunnel at the Aerospace faculty of TU Delft. The cone was rotated at 5000 RPM and a parametric study with different inflow velocities were conducted. Using an infrared camera, surface temperatures were measured. 2000 images were obtained at a rate of 200 Hz. This IRT setup (schematic shown in figure 2.23) was verified using a time resolved Particle Image Velocimetry (PIV) setup.

The coordinate system (figure 2.9) and variables used to characterise the flow parameters were similar to the ones defined in the theoretical and experimental studies by Kohama and Kobayashi (section 2.2). The local Reynolds number (Re_l) used in the experiment was:

$$Re_l = \frac{lU_e}{\nu} \quad (2.10)$$

Here, U_e is the edge velocity of the boundary layer, given by Garrett and Peake [34] as $U_e = Cx^m$. The value of C and m were established experimentally by them to be, $1.84U_\infty$ and m as 0.23 [3] respectively. l is the location of the point along the meridian.

Their study involved Re_D (diameter based Reynolds number, $Re_D = U_\infty D / \nu$) ranging from 7.4×10^3 to 2×10^4 and S_b (diameter based rotation ratio, $S_b = r\omega / U_\infty$) varying from 0 to 5. The cone and ellipse are rotated at 5000 RPM.

With their results on the slender cone in line with the experimental and theoretical work carried out in the past (with respect to the axial inflow), they extended the range from previous research by introducing non-axial inflow over the rotating cones (detailed flow physics study done by Tambe et al. [5]). The motivation behind this particular study can go back to the description of flow development inside a boundary layer engine upstream of the fan (chapter 2 section 2.1.4). For the non-axial inflow, the authors explained the spatial delay in the formation of the coherent structures by taking into account the asymmetric distribution of the local Reynolds number and local rotation ratio. The growth of vortices has already been established, in the earlier sections, to be directly influenced by those two factors. Even though the boundary layer remains unstable at lower rotation ratios, the asymmetry makes sure that they do not form coherent structures until downstream over the cone where the influence of S on the instability characteristics such as the azimuthal number of vortices is significantly lower. The following summarises the work done by Tambe et al. [3] and [5].

- For the axial inflow case, the vortices appeared to undergo amplification through vortex pairing
- Asymmetry of non-axial inflow appeared to suppress the initial growth of the spiral vortices and were detected at higher local rotation ratios and local Reynolds numbers
- The local Reynolds number varied azimuthally for the non-axial case and thus different stability characteristics along the circumference caused the wavelengths and angles of most amplified perturbations to vary along the circumference

- At higher rotation ratios the local flow parameters do not affect the stability characteristics to a large extent and thus the spiral vortices were found to grow under non-axial flow conditions

The experiments conducted by Tambe et al. [5], visualised the footprints of these vortices using Infrared Thermography. Instantaneous snapshots of the axial and non-axial inflow cases are shown in figures 2.24 and 2.25.

To visualise individual vortices, a wall normal velocity fluctuation contour was plotted by Tambe et al. [5] for both axial and non-axial inflow with a 4° incidence angle (including the windward and leeward sides). Figures 2.26 and 2.27 shows these contours. These fluctuations are obtained by subtracting the mean flow velocity from the instantaneous velocity.

In the experiments by Tambe et al. [5], streamwise transient mean velocity contours were plotted to visualise the physical phenomena near the wall. They observed that with the amplification of the spiral vortices high momentum fluid in the outer regions of the boundary layer are transported towards the wall leading to a higher streamwise momentum near the wall.

Their study on the rotating ellipsoids showed similar results to the above mentioned case, but with pressure gradient playing a greater role in such a geometry, Tambe et al. [4] advice the necessity for further work.

Michael Karp and M.J. Phillip Hack [13] in 2018, worked on the transition process of inviscid flows over convex surfaces using DNS. Secondary instabilities and transient growth over convex surfaces was investigated.

Figure 2.28 shows the geometry used in their study. As part of their mathematical formulation, Karp and Hack [13] used the non-dimensional curvature parameter, Görtler Parameter ($\widetilde{G}\ddot{o}$)

$$\widetilde{G}\ddot{o} = \frac{U_{\infty}\delta}{\nu} \sqrt{\frac{\delta}{R}} \quad (2.11)$$

δ represents the boundary layer thickness, ν is the kinematic viscosity and R is the radius of the convex surface. Equation 2.11 was re-written in non-dimensional form, using the well used, Reynolds Number and normalised curvature ($\kappa_c = \delta/R$)⁵:

$$\widetilde{G}\ddot{o} = Re\sqrt{\kappa_c} \quad (2.12)$$

They used Local stability analysis to study transient growth. Feeding DNS the optimal solution as inflow conditions, they were able to study the non-linear and non-parallel effects.

Figure 2.29 shows the DNS results over the convex surface.

The following summarises the observations by Karp et al. [13]:

- Compared to flat plates, the stability analysis used showed negligible impact of curvature on secondary instabilities
- The secondary instabilities alone do not ensure transition to turbulence and highly energetic or long streaks are needed for the process to be completed. Thus, convex surfaces may be used to delay the transition process

As mentioned in chapter 1, the primary motivation area for the work conducted in this master thesis was the application area, namely, spinners used in engines operating under the concept of BLI. When it comes to this field, there has been very few work, and any numerical research conducted has focused on the efficiency of the fan blades. Lei et al. [6] worked on the development of a criterion for hub corner stall on axial compressors in 2008. The criterion they developed was a function of the following parameters :

1. Mach Number
2. Reynolds Number
3. Aspect Ratio

⁵The subscript, c is used in this text for this parameter to separate it from the turbulence kinetic energy variable used later. This was not in the original definition by the authors Karp and Hack [13]

4. Ratio of incoming boundary layer thickness and chord length
5. Solidity
6. Flow inlet and exit angles
7. Blade stagger angle
8. Blade camber angle
9. Skewness of flow with respect to end wall boundary layer

A diffusion parameter was defined to show the flow diffusion limit associated with stall and is a factor of points 5 to 9 above. Figure 2.30 shows how the stall criterion varies with the diffusion parameter.

The plot shows the effects of aspect ratio, Reynolds number and boundary layer thickness. Corner stall was observed for diffusion parameter above 0.4 (critical diffusion parameter) and a higher value represents flow reversal on both the end wall and suction side. An interesting observation in this plot is the region of overlap near the critical value of the diffusion parameter. A higher or lower value of the stall indicator may be obtained for different combinations of blade passage geometry and flow conditions. The authors mention that the reasons for this were yet to be solved.

For further details, the interested reader is directed to the works by Hah et al. [35] for the effects of inlet distortion in a transonic compressor rotor. The works by Chen et al. [36] for the fan interaction with flow in a specific design of a Boundary Layer Ingestion engine. Fidalgo et al. [19] also worked on fan distortion interaction for the NASA Rotor 67 Transonic stage and Hall et al. [37] worked on an analysis of fan stage conceptual design attributes for BLI.

2.4. Vortex Visualisation

Intuitively a vortex can be considered to be the rotating motion of a collection of particles around a central point [38]. This definition being vague, methods were needed to be developed for visualising these motions of fluid. There exist many different definitions of a vortex used to identify them in any numerical simulation and there remains no consensus on any one particular method. The choice depends on the particular case. This being said, a short note on the various existing methods will be explored in this section.

Before moving onto the methods, a couple of definitions is important at this point :

- **Vortex Core:** For inviscid flows, the centre of a fluid body about which it is rotating
- **Vortex Core Line:** The locus of the vortex core as it moves through a velocity field

2.4.1. Mathematics

Most of the techniques implement an eigen analysis on the velocity gradient tensor [39]. The velocity gradient tensor can be written as,

$$\mathbf{D} = \nabla U = \begin{bmatrix} \frac{\partial u}{\partial x} & \frac{\partial u}{\partial y} & \frac{\partial u}{\partial z} \\ \frac{\partial v}{\partial x} & \frac{\partial v}{\partial y} & \frac{\partial v}{\partial z} \\ \frac{\partial w}{\partial x} & \frac{\partial w}{\partial y} & \frac{\partial w}{\partial z} \end{bmatrix} \quad (2.13)$$

This can be decomposed into its symmetric and anti-symmetric parts,

$$\begin{aligned} S_{ij} &= \frac{1}{2} \left(\frac{\partial u_i}{\partial x_j} + \frac{\partial u_j}{\partial x_i} \right) \\ \Omega_{ij} &= \frac{1}{2} \left(\frac{\partial u_i}{\partial x_j} - \frac{\partial u_j}{\partial x_i} \right) \end{aligned} \quad (2.14)$$

Here S_{ij} is the symmetric part of the tensor and Ω_{ij} is the anti-symmetric part. They are called, the rate of shear strain tensor and vorticity tensor respectively.

The characteristic equation for the velocity gradient (equation (2.13)) is :

$$\lambda^3 + P\lambda^2 + Q\lambda + R = 0 \quad (2.15)$$

Here, λ are the eigenvalues and the coefficients are :

- $P = -\text{tr}(\mathbf{D})$; Note : "tr" represents the trace of the matrix
- $Q = \frac{1}{2}(\text{tr}(\mathbf{D})^2 - \text{tr}(\mathbf{D}^2)) = \frac{1}{2}((\|\Omega\|)^2 - (\|S\|)^2)$
- NOTE : $\|\Omega\| = \text{tr}(\Omega\Omega^t)^{1/2}$; "t" representing the transpose of the matrix

2.4.2. λ_2 Criterion

Jinhee Jeong and Fazle Hussain [40] introduced this criterion for visualising vortices. Their study identified vortex cores and defined the following requirements for the existence of a vortex core:

- Presence of net circulation around the core (non zero vorticity)
- Vortex should be Galilean invariant (Galilean invariant quantities are independent of observers position and velocity)

Intuitively, the pressure at the vortex core should be a point of minima, but there exist exceptions to this condition,

- Unsteady straining in regions without vortices causing pressure minima
- Presence of high pressure regions in the vortex core due to viscous effects

The authors suggested taking the gradient of the Navier-Stokes equations,

$$a_{i,j} = -\frac{1}{\rho} p_{,ij} + \nu u_{i,jkk} \quad (2.16)$$

Here, $a_{i,j}$ represents the acceleration gradient and $p_{,ij}$ represents the Hessian of pressure and is symmetric. $a_{i,j}$ is decomposed as follows :

$$a_{i,j} = \left[\frac{DS_{i,j}}{Dt} + \Omega_{ik}\Omega_{kl} + S_{ik}S_{kj} \right] + \left[\frac{D\Omega_{i,j}}{Dt} + \Omega_{ik}S_{kj} + S_{ik}\Omega_{kj} \right] \quad (2.17)$$

The term within the first "[]" represent the symmetric part and the second one, anti-symmetric.

The anti-symmetric part of equation (2.16) is the vorticity transport equation and the symmetric part can now be written as :

$$\frac{DS_{ij}}{Dt} - \nu S_{ij,kk} + \Omega_{ik}\Omega_{kj} + S_{ik}S_{kj} = -\frac{1}{\rho} p_{,ij} \quad (2.18)$$

The first term above is the unsteady irrotational straining and the viscous effects are represented by the second term, hence for the previously mentioned reasons, they will be ignored and thus only the term $S^2 + \Omega^2$ is taken.

For a local pressure minima to be present, two positive eigenvalues of the tensor $p_{,ij}$ are needed. The authors define a vortex core as, "a connected region with two negative eigenvalues" of $S^2 + \Omega^2$. This being symmetric, provides 3 eigenvalues, which can be ordered such that, $\lambda_1 \geq \lambda_2 \geq \lambda_3$. Which, according to the definition, results in the requirement that $\lambda_2 < 0$ within the core (hence the name).

Jiang et al. [41] worked on an extensive review of the various types of vortex identification methods available and according to them, this method is not always suitable when distinguishing multiple vortices.

2.4.3. Q Criterion

Hunt, Moin and Wray [42] defined an eddy as a region having a second positive invariant (Q). For $Q > 0$, the vorticity tensor exceeds the rate of strain tensor. To this, another condition set by the authors was the requirement of pressure within the vortex core exceeds the ambient pressure.

Jeong et al. [40] had compared their definition for λ_2 with other methods and mentioned that the Q criterion is insufficient if non-uniform strain fields cause the vortex to expand locally but show better representation when stretching and compression is significant.

2.4.4. Δ Criterion

This is a Galilean Invariant criterion introduced by Dallmann et al. [43]. They defined vortices as flow fields whose eigenvalues have complex conjugate pairs. Additionally, the streamlines should either be spiralling or closed in a local reference frame. Mathematically, this can be represented as,

$$\Delta = \left(\frac{Q}{3}\right)^3 + \left(\frac{R}{2}\right)2 > 0 \quad (2.19)$$

For an incompressible flow $P = 0$ (defined in section 2.4.1) and critical point theory⁶ is used to visualise the points obtained through equation (2.19).

2.4.5. Swirling Strength Criterion

This method uses the imaginary part of the complex eigen values of the velocity gradient tensor to visualise the vortices. The idea is to decompose the velocity gradient tensor into the imaginary and complex eigenvalues and eigenvectors [44]. Mathematically,

$$\nabla u = [d_{i,j}] = [\vec{v}_r \quad \vec{v}_{cr} \quad \vec{v}_{ci}] \begin{bmatrix} \lambda_r & 0 & 0 \\ 0 & \lambda_{cr} & \lambda_{ci} \\ 0 & -\lambda_{ci} & \lambda_{cr} \end{bmatrix} [\vec{v}_r \quad \vec{v}_{cr} \quad \vec{v}_{ci}]^T \quad (2.20)$$

This represents the real part of the eigenvector (\vec{v}_r) and λ_r is the corresponding real eigenvalue. The complex conjugate pair of eigenvalue is, $\lambda_{cr} \pm i\lambda_{ci}$ and the corresponding eigenvector pair, $\vec{v}_{cr} \pm \vec{v}_{ci}$. The streamlines are expressed in a three dimensional coordinate system using the three eigenvectors and thus the flow can be visualised as either stretched or compressed on the real plane and swirling in the complex plane. The eigenvalue ($\lambda_{ci} > 0$) will represent the strength of this swirling motion. This threshold is not well defined and needs to be set based on user preference.

2.4.6. Helicity

Introduced by Levy et al. [45], works on normalised helicity to extract vortex core lines. this quantity, H_n is defined everywhere, except at critical points,

$$H_n = \frac{\vec{v} \cdot \vec{\omega}}{|\vec{v}||\vec{\omega}|} \quad (2.21)$$

Thus, H_n is basically the cosine of the angle between the velocity and vorticity vector. The sign of this will indicate the direction of the swirl. The extracted core line, however, might not always correspond to an actual vortex core line.

2.4.7. Swirl Parameter Method

Introduced by Berdahl et al. [46] in 1993. This swirl parameter is defined as,

$$\tau_s = \frac{\tau_{convec}}{\tau_{orbit}} \quad (2.22)$$

Here, τ_{convec} is defined as the time taken for the fluid particle to convect through a region of complex eigenvalues and τ_{orbit} represents the time taken by the particle to make one revolution. Mathematically,

$$\tau_{convec} = \frac{2\pi}{|I_m(\lambda_c)|} \quad (2.23)$$

$$\tau_{orbit} = \frac{L}{V_{convec}} \quad (2.24)$$

$|I_m(\lambda_c)|$ is the imaginary part of the complex conjugate pair of the eigenvalues. L is the characteristic length associated with the corresponding eigenvalues and V_{convec} is the convective velocity in the direction of L . V_{convec} is calculated by projecting the velocity vector onto the planar normal to the vorticity or the real eigenvector. Mathematically,

$$V_{convec} = \vec{v} - (\vec{v} \cdot \vec{n})\vec{n} \quad (2.25)$$

⁶Critical points are points in a function $f(c)$ such that $f'(c) = 0$ or is undefined

Observing the definitions of τ_s (equation (2.22)), τ_{convect} (equation (2.23)) and τ_{orbit} (equation (2.24)), if $\tau_s \rightarrow 0$, the fluid is convecting too fast to be captured by the vortex. Thus, non-zero τ_s , indicates presence of vortices. Colormaps or isosurfaces are used to visualise them, using arbitrary (based on user requirements) thresholds.

2.4.8. Eigenvector Method

The eigenvalues and eigenvectors are evaluated at critical points in the flow-field and define the flow pattern about that point.

If there are no critical points at the centre of a swirling flow, the velocity vectors are projected onto a plane perpendicular to the eigenvector of the real eigenvalue and are checked if they are zero on that plane.

The evaluation involves creating tetrahedral cells. Contiguous line segments may not form.

2.4.9. Maximum Vorticity

Introduced by Strawn et al. [47], wherein, a vortex core is defined as the local maxima of the vorticity magnitude, $|\bar{\omega}|$. Applicable to free shear flows. Across a mesh cell, the absolute value is assumed to vary bilinearly. However, setting the threshold remains arbitrary.

2.4.10. Streamline Method

Uses the winding angle method. This measures the amount of rotation of the streamline with respect to a point (a_w). Sadarjoen et al. [48] measure the cumulative change in direction of streamline segments.

$$a_w = \sum_{i=1}^{N-2} \angle(P_{i-1}, P_i, P_{i+1}) \quad (2.26)$$

P_i represents the N streamlines. A vortex is said to exist if $a_w \leq 2\pi$ for at least one streamline. Cluttering algorithm is used to group streamlines belonging to the same vortex.

2.5. Conclusions and Research Objective

The above sections described in brief the work done by previous researchers on this area. The studies have focused primarily on using experimental techniques to understand the development of these vortices over the cone. The two main divisions in this field can be stated as the study of flow under axial inflow and non-axial inflow. There has been little to no work conducted using numerical techniques to study this phenomenon and with the advent of modern computation power, this master thesis will attempt to fill the void. The research question is thus stated as follows,

"Can numerical techniques model the spiral counter-rotating vortices observed over rotating cones under axial and non-axial inflow?"

This leads the master thesis to work on the following sub-questions :

- How effective is the Baseline Explicit Algebraic Reynolds Stress (BSL EARS) model of the Unsteady Reynolds Averaged Navier Stokes (URANS) method, in the visualization of these vortices?
- Is the Large Eddy Simulation (LES), Wall Adapting Local Eddy Viscosity (WALE) an appropriate model for simulating the counter-rotating vortices under axial and non-axial inflow?
- How do the azimuthal number of vortices vary along the length of the cone under axial and non-axial inflow?

It is also important to set the scope of this project at this stage. The parameters not included in the study are the turbulence models and the coefficients used for BSL EARS and WALE.

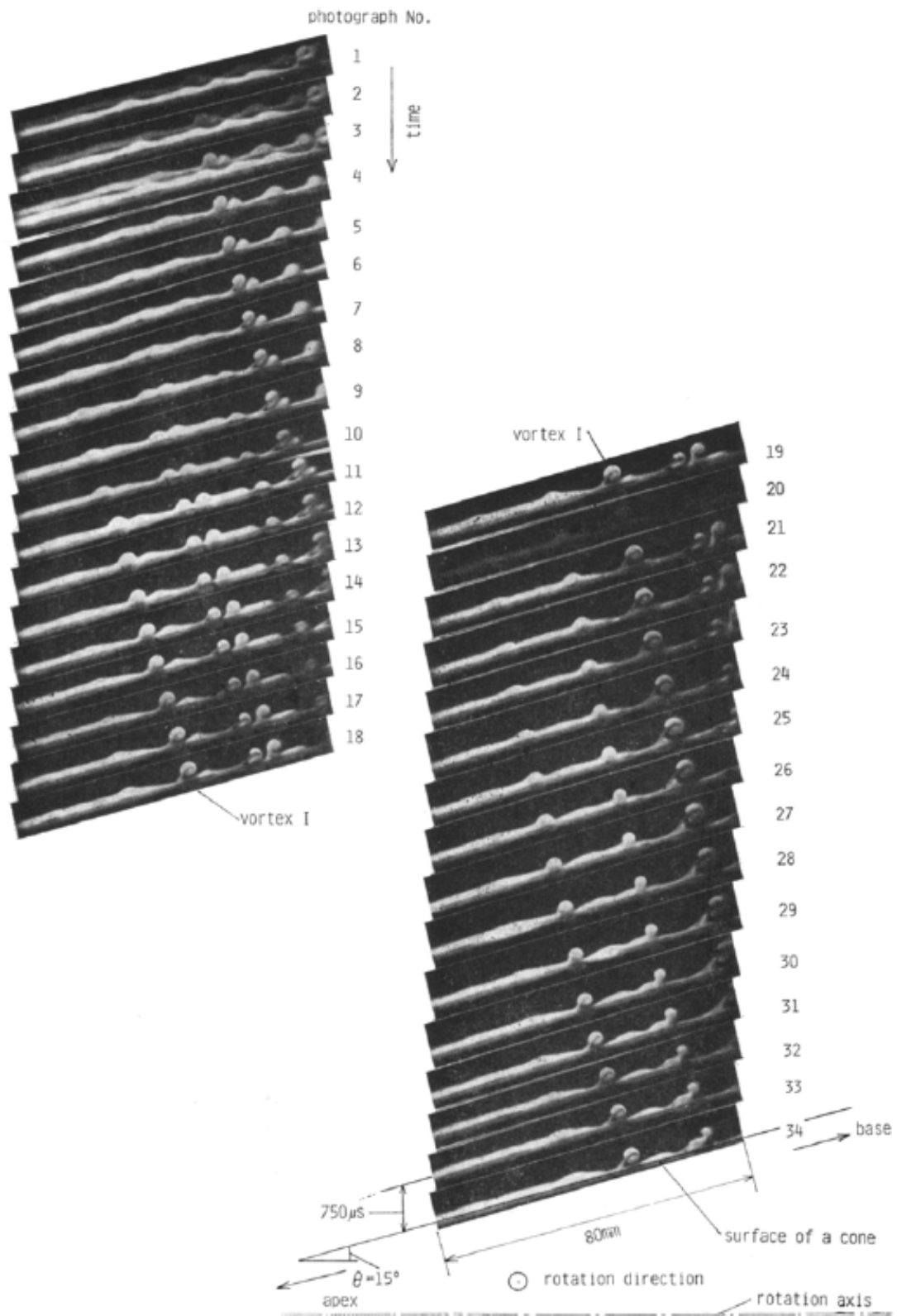


Figure 2.15: Development of spiral vortices in the transition regime. Rotation Rate : 785 RPM Inflow velocity : 1.85 m/s (Image source: [24])

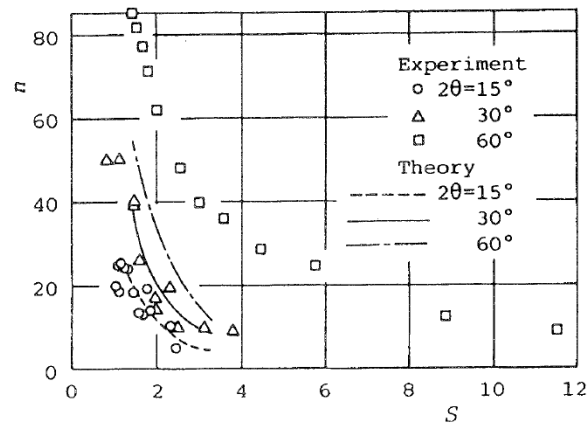


Figure 2.16: Variation of number of spiral vortices with local rotation ratio for different cone apex angles (Image source: [25])

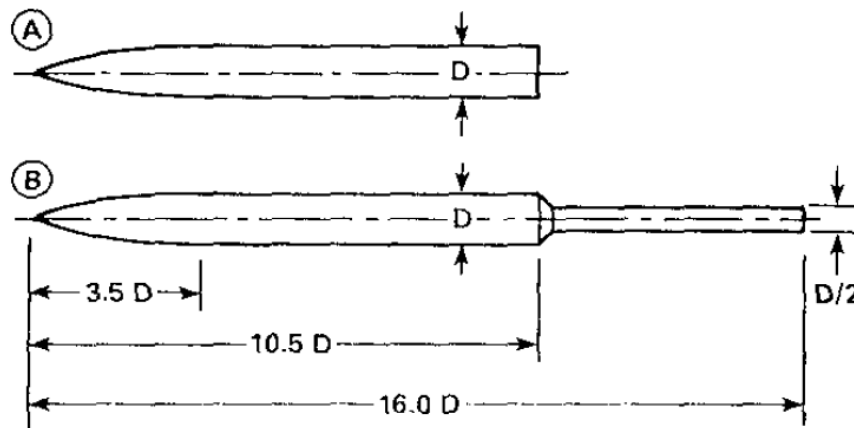


Figure 2.17: Ogive configuration implemented by Degani and Schiff (Image source; [30])

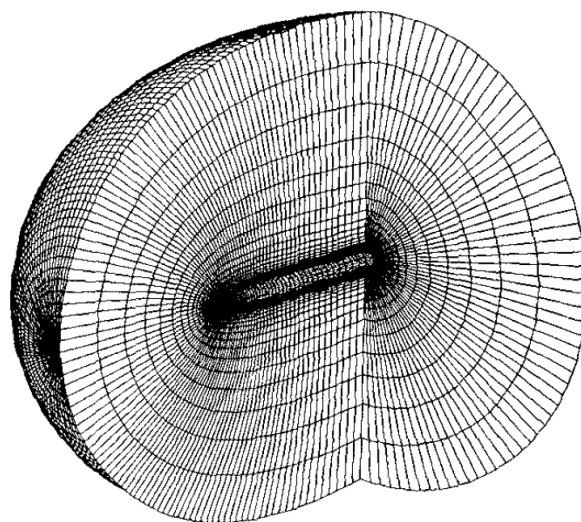


Figure 2.18: Mesh used for the numerical simulation of the ogive (Image source: [30])

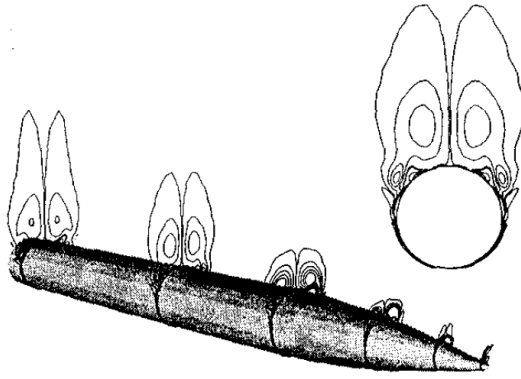


Figure 2.19: Helicity density contours. Mach number = 0.8, angle of attack = 40° and diameter based Reynolds Number = 200,000. Jet = 0% (Image source: [30])

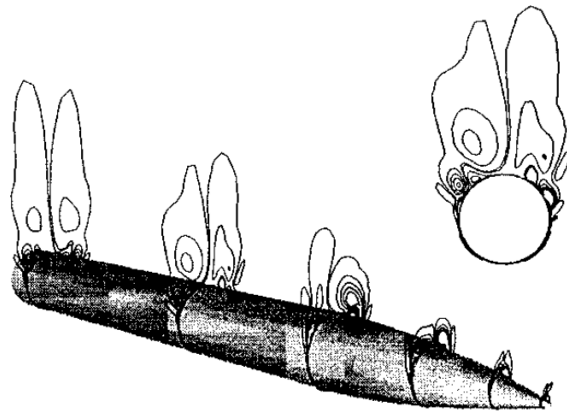


Figure 2.20: Helicity density contours. Mach number = 0.8, Angle of attack = 40° , Diameter based Reynolds Number = 200,000. Jet = 1.2% at $x/D \approx 1.2$ (Image source: [30])

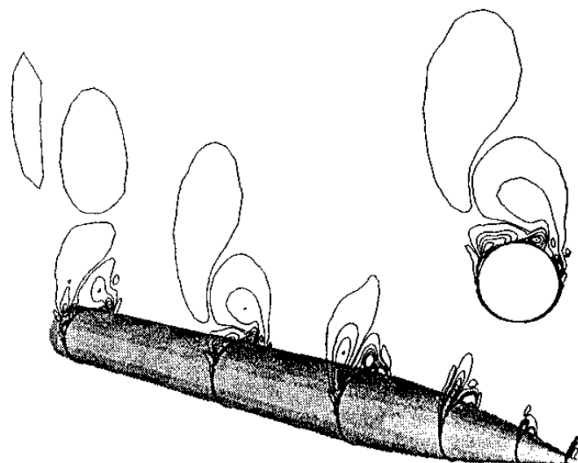


Figure 2.21: Helicity density contours. Mach number = 0.8, Angle of attack = 40° , Diameter based Reynolds Number = 200,000. Jet = 1.2% at $x/D \approx 0.12$ (Image source: [30])

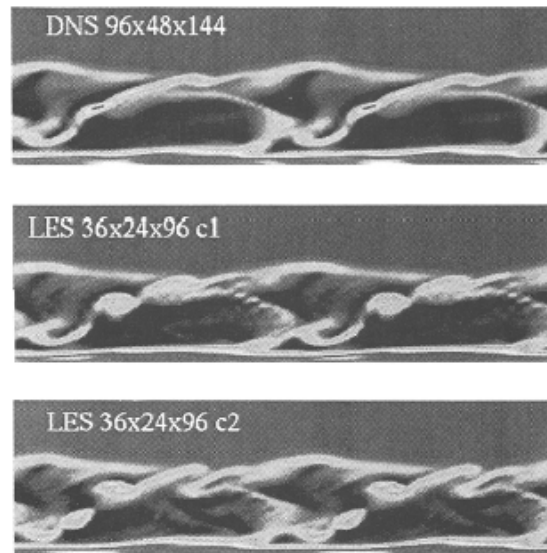


Figure 2.22: Comparison of instantaneous spanwise vorticity (Image source: [31])

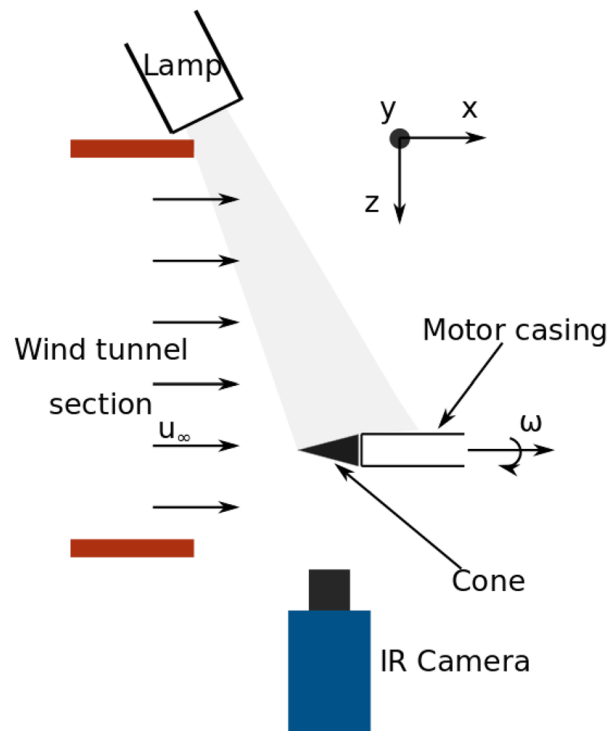


Figure 2.23: Experiment setup schematic (Image source: [3])

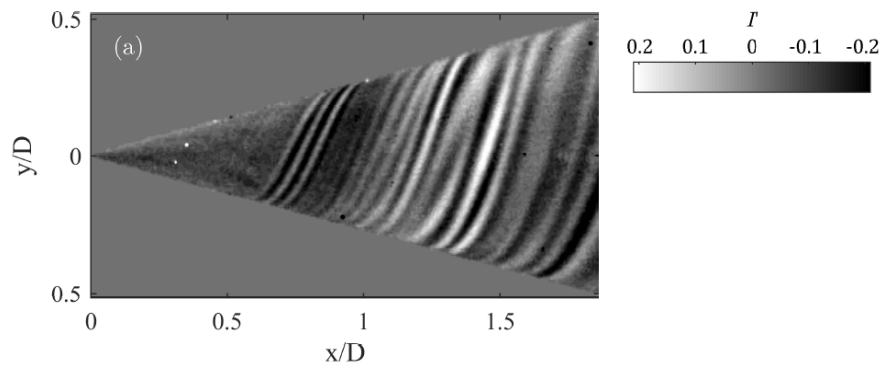


Figure 2.24: Instantaneous surface temperature footprints of spiral vortices under axial inflow (Image source: [5])

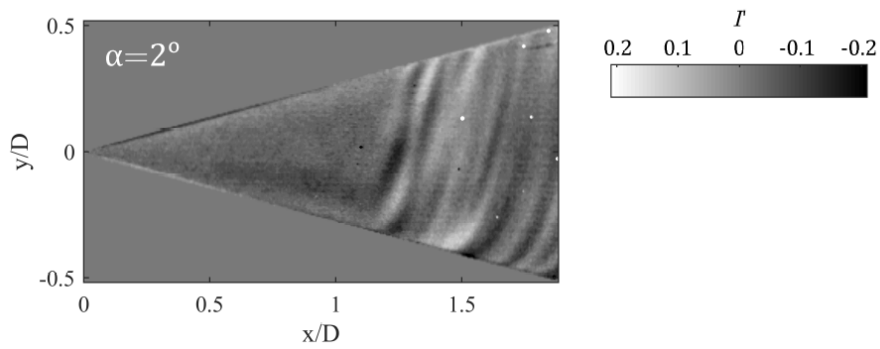


Figure 2.25: Instantaneous surface temperature footprints of spiral vortices under non-axial inflow with incidence angle: 2° (Image source: [5])

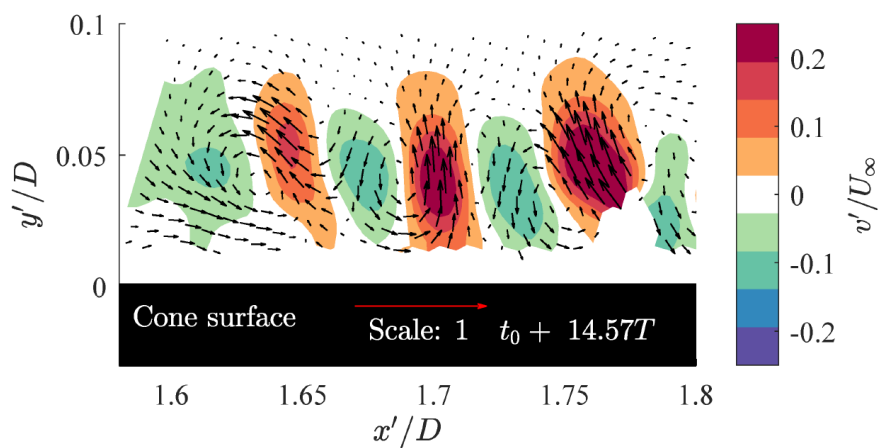


Figure 2.26: Instantaneous contour plots of wall normal velocity fluctuations under axial inflow (Image source: [5])

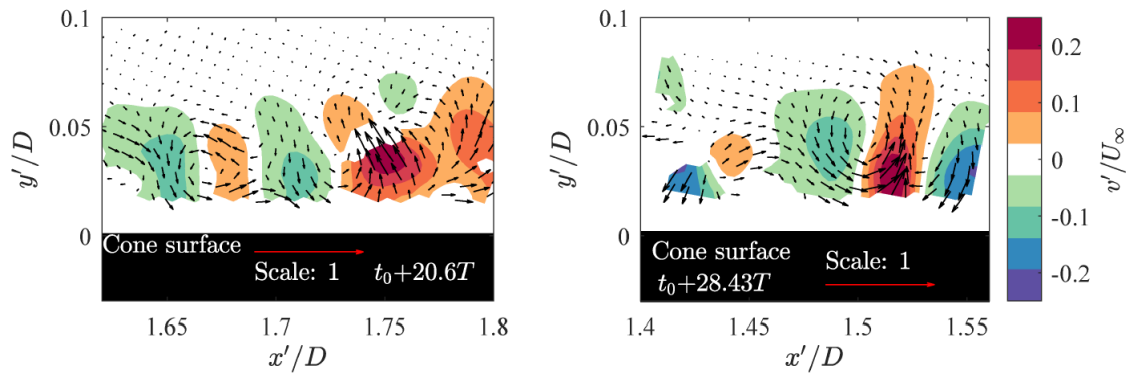


Figure 2.27: Instantaneous contour plots of wall normal velocity fluctuations under non-axial axial inflow (4° incidence angle) for windward (left image) and leeward (right image) meridians (image source: [5])

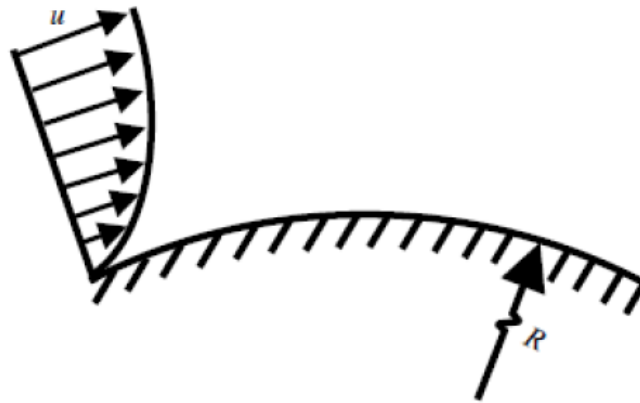


Figure 2.28: Convex geometry used by Karp and Hack (Image source: [13])

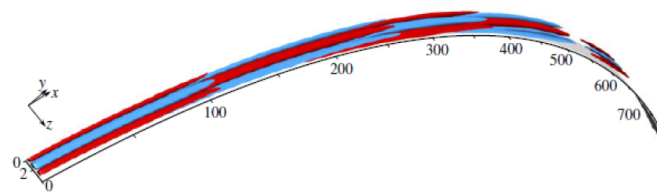


Figure 2.29: Linear DNS showing streamwise streaks using isosurfaces of 0.01 times the maximum streamwise velocity disturbance. Left to right flow. Red signifies positive disturbance and blue negative. (Image source: [13])

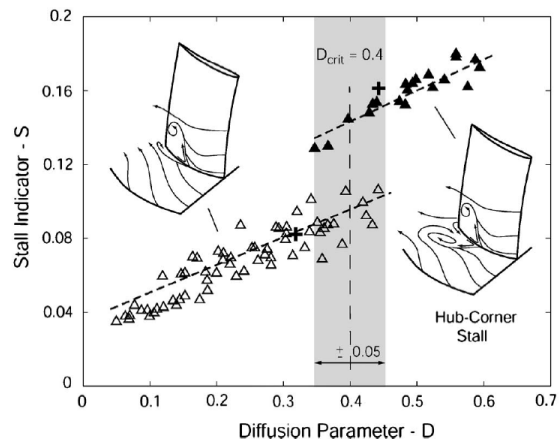


Figure 2.30: Variation of Stall criterion with Diffusion parameter (Image source: [6])

3

Turbulence Modelling

Mechanism of the formation of observed spiral counter rotating vortices were discussed in the previous chapter. It was found that these vortices form in the laminar to turbulent transition region of the flow over rotating cones. Turbulence is a complex three dimensional unsteady phenomena with a wide range of length and time scales. There does not yet exist a closed system of equations defining this complex flow for an analytical study.

In practice, turbulence is characterised with high Reynolds number flows and solving the Navier-Stokes equations numerically is not always practical as the smallest length scales associated with such conditions are smaller than the smallest mesh volumes.

To predict the effects of turbulence, various Computational Fluid Dynamics (CFD) methods have been developed making use of models. This would be a workaround for the limitations due to mesh cells.

This chapter will provide a brief introduction to the theory involved in turbulence modelling. This begins with an introduction to turbulence, its characteristics and then moves onto describing some of the modelling techniques available.

3.1. Navier Stokes Equations

The discussion on turbulence must first begin with defining a mathematical model for fluid motion.

These equations describing the general fluid motion may be integral or differential in form and depends on the fluid model chosen (whether it is a fluid volume or infinitesimally small fluid element). The reader will obtain a more descriptive derivation of the equations from the highly informative book on CFD by John D. Anderson [49].

Using the Eulerian model, wherein the equations are based on observing a fixed point in the fluid domain and defining the following velocity components :

$$\begin{aligned}u &= u(x, y, z, t) \\v &= v(x, y, z, t) \\w &= w(x, y, z, t) \\\rho &= \rho(x, y, z, t)\end{aligned}\tag{3.1}$$

The velocity vector defining the direction of fluid may be written as,

$$\vec{V} = \bar{u}\hat{i} + \bar{v}\hat{j} + \bar{w}\hat{k}\tag{3.2}$$

Here \hat{i} , \hat{j} and \hat{k} represent the unit vectors in the x, y and z direction respectively and u , v and w represent the velocity components in the x, y and z direction respectively. ρ represents the density.

Figure 3.1 shows an infinitesimally small fluid element along with the mass flow across through every face. The continuity equation based on such a model is written as,

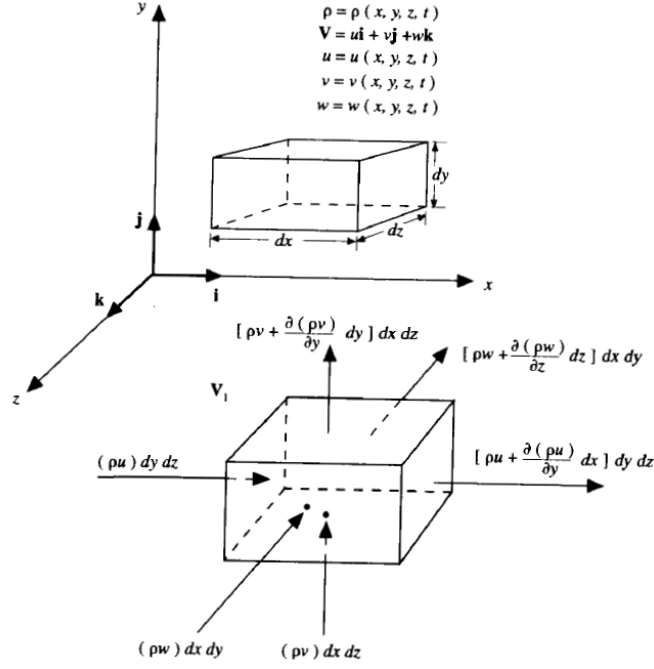


Figure 3.1: Illustration depicting a fluid element (Image source: [49])

$$\frac{\partial \rho}{\partial t} = \nabla \cdot (\rho \mathbf{V}) \quad (3.3)$$

The momentum equation is derived based on Newton's 2nd Law. The equation in all three directions,

$$\begin{aligned} \frac{\partial(\rho u)}{\partial t} + \nabla \cdot (\rho u \mathbf{V}) &= -\frac{\partial p}{\partial x} + \frac{\partial \tau_{xx}}{\partial x} + \frac{\partial \tau_{yx}}{\partial y} + \frac{\partial \tau_{zx}}{\partial z} + \rho f_x \\ \frac{\partial(\rho v)}{\partial t} + \nabla \cdot (\rho v \mathbf{V}) &= -\frac{\partial p}{\partial y} + \frac{\partial \tau_{xy}}{\partial x} + \frac{\partial \tau_{yy}}{\partial y} + \frac{\partial \tau_{zy}}{\partial z} + \rho f_y \\ \frac{\partial(\rho w)}{\partial t} + \nabla \cdot (\rho w \mathbf{V}) &= -\frac{\partial p}{\partial z} + \frac{\partial \tau_{xz}}{\partial x} + \frac{\partial \tau_{yz}}{\partial y} + \frac{\partial \tau_{zz}}{\partial z} + \rho f_z \end{aligned} \quad (3.4)$$

The term ρf_x represents the x component of the body forces acting per unit mass on the fluid element. Similarly, ρf_y and ρf_z are the y and z components. τ_{xx} , τ_{yy} and τ_{zz} represent the normal stresses and τ_{xy} components represent the shear stresses. Both are related to the velocity gradients. The normal components are negligible in most wall bounded flows with the exception of high axial direction velocity gradient, such as those across shock waves.

Using the stress tensor relation,

$$\tau_{ij} = -P\delta_{ij} + \mu\left(\frac{\partial V_i}{\partial x_j} + \frac{\partial V_j}{\partial x_i}\right) \quad (3.5)$$

P represents the pressure and μ is the constant dynamic pressure.

The equation set 3.4 can be re-written using the substantial derivative and equation 3.5. The momentum equation for a constant density divergence free ($\nabla \cdot \mathbf{V} = 0$) flow can thus be given by,

$$\frac{D\mathbf{V}}{Dt} = -\frac{1}{\rho}\nabla p + \nu\nabla^2\mathbf{V} \quad (3.6)$$

Here, p is the modified pressure and ν is the kinematic viscosity ($\nu = \mu/\rho$).

The energy equation based on the conservation of energy, i.e. the first law of thermodynamics, is written in the following form,

$$\begin{aligned}
 \frac{\partial}{\partial t} \left[\rho \left(e + \frac{V^2}{2} \right) \right] + \nabla \cdot \left[\rho \left(e + \frac{V^2}{2} \right) \bar{\mathbf{V}} \right] = & \rho \dot{q} + \frac{\partial}{\partial x} \left(k \frac{\partial T}{\partial x} \right) + \frac{\partial}{\partial y} \left(k \frac{\partial T}{\partial y} \right) + \frac{\partial}{\partial z} \left(k \frac{\partial T}{\partial z} \right) \\
 & - \frac{\partial (up)}{\partial x} - \frac{\partial (vp)}{\partial y} - \frac{\partial (wp)}{\partial z} \\
 & + \frac{\partial (u\tau_{xx})}{\partial x} + \frac{\partial (u\tau_{yx})}{\partial y} + \frac{\partial (u\tau_{zx})}{\partial z} \\
 & + \frac{\partial (v\tau_{xy})}{\partial x} + \frac{\partial (v\tau_{yy})}{\partial y} + \frac{\partial (v\tau_{zx})}{\partial z} \\
 & + \frac{\partial (w\tau_{xz})}{\partial x} + \frac{\partial (w\tau_{yz})}{\partial y} + \frac{\partial (w\tau_{zz})}{\partial z} \\
 & + \rho f \cdot \bar{\mathbf{V}}
 \end{aligned} \tag{3.7}$$

In the above equation, $e + \frac{V^2}{2}$ represents the total energy and \dot{q} is the rate of volumetric heat addition per unit mass. $\frac{V^2}{2}$ represents the kinetic energy due to the translation of the fluid. The above equations ((3.3), (3.4) and (3.7)) are not applicable for chemically reacting flows which would need the additional mass diffusion term. If these equations are to be further simplified, the assumption of inviscid flow may be made, which would further neglect the viscous transport phenomena terms (shear and normal stresses), dissipation and thermal conductivity terms, leading to the Euler equation. There does not yet exist any closed form solution to the set of 3 equations, collectively termed as the Navier - Stokes equation [49].

3.2. Characteristics and Effects

The characteristics for any turbulent flow may be listed as follows :

- Three dimensional
- Unsteady
- High Reynolds Number flow
- Rotational
- Viscous
- Chaotic
- Wide range of length and velocity scales of the turbulent structures
- Coherent structures

Before delving into the mathematical description, it is important to detail some of the effects of turbulence:

- Turbulence enhances mixing. This is most evident in the combustion chambers of engines
- Delays flow separation. As an example, consider the flow over a wing, due to the geometry of the wing, the flow particles over the surface would lose momentum since it is faced with an adverse pressure gradient. This will cause the fluid particle to separate from the surface and lead to pressure drag. Turbulence can minimise this, as turbulent flows have highly energetic particles, thus having higher momentum and more likely to overcome the gradient. Vortex generators on wing surfaces induce turbulence and delay flow separation. Dimples on golf balls serve the same purpose.
- Turbulence is also responsible for increasing wall friction, as wall friction is proportional to the Reynolds Number

Modelling such a process involves complex mathematics and the following few sections will delve into the different models used for this purpose over the many years.

3.3. Energy Cascade

The discussion in this section is based on the book by Pope [50].

It was mentioned in subsection 3.2 that turbulent flows have a wide range of length and velocity scales. The flow thus have high kinetic energy and anisotropy. Richardson in 1922, introduced the concept of Energy Cascade. The basic principle here is that kinetic energy is transferred inviscidly from larger (more energetic) scales to successively smaller scales till viscous dissipation takes over the energy transfer model. Kolmogorov in 1941, quantified this process by defining the smallest scales (named as the Kolmogorov scales).

Consider moderately coherent structures localised within a region of length scale, \mathbf{l} , these structures can be named as eddies. According to the Energy Cascade theory, the largest eddies are unstable and break into smaller and smaller eddies, transferring their energy. The largest eddies have length scales comparable to the length scale of the flow, \mathcal{L} . When the eddies are small enough to be stable, viscosity is responsible for the dissipation of this kinetic energy.

This dissipation rate, ϵ is based on the energy transfer from the largest eddies. From experimental and analytical studies of free shear flows (for high Reynolds number flows), the dissipation rate is found to scale with the velocity and length scales of the largest eddies (\mathbf{u}_0 and \mathbf{l}_0) as,

$$\epsilon \propto \frac{(\mathbf{u}_0)^3}{\mathbf{l}_0} \quad (3.8)$$

The quantification of the smallest scales determines when the breakdown process comes to a halt. Kolmogorov stated that at high Reynolds numbers, the smallest scales can be assumed to be statistically isotropic and defined those scales using ϵ and ν (kinematic viscosity) :

$$\begin{aligned} \eta &\equiv \left(\frac{\nu^3}{\epsilon}\right)^{\frac{1}{4}} \\ u_\eta &\equiv (\epsilon\nu)^{\frac{1}{4}} \\ \tau_\eta &\equiv \left(\frac{\nu}{\epsilon}\right)^{\frac{1}{2}} \end{aligned} \quad (3.9)$$

η , u_η and τ_η represent the length, velocity and time scales of the smallest eddies. The Reynolds number associated with these scales equals unity and is thus consistent with the energy Cascade Theory (as viscous dissipation dominates for lower Reynolds numbers). To understand the cascade process better, the range of scales can be divided as illustrated in figure 3.2.

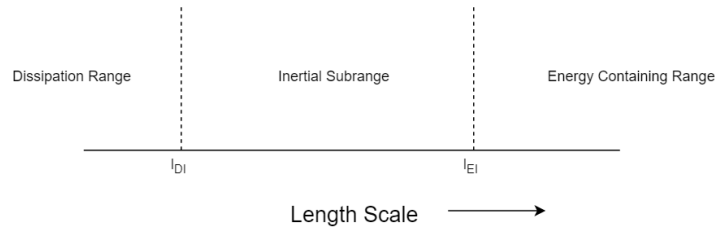


Figure 3.2: Division of length scales for High Reynolds Number flows

The inertial subrange have motions defined by the inertial effects with negligible viscous dissipation and thus ϵ determines the dissipation rate in this range. l_{DI} and l_{EI} are the demarcations in the range segregating the "inertial subrange" from the "dissipation range" and the "energy containing range" from the "inertial range".

As these structures are in motion, the lengthscales can be associated with wavenumbers, κ , defined as,

$$\kappa = \frac{2\pi}{\lambda} \quad (3.10)$$

Here, λ is the wavelength of the turbulent fluctuations. The net turbulent kinetic energy (\mathbf{k}) within a wavenumber range of κ_a and κ_b is thus,

$$\mathbf{k}(\kappa_a, \kappa_b) = \int_{\kappa_a}^{\kappa_b} E(\kappa) d\kappa \quad (3.11)$$

3.4. Reynolds Averaged Navier Stokes (RANS)

The Navier-Stokes equations (equation (3.3) - (3.7)) model the velocity field, $\bar{\mathbf{V}}(x, t)$. The following discussion contains only the inviscid form of the continuity and momentum equations.

This velocity field is decomposed (Reynolds Decomposition) into its mean and fluctuating components,

$$\bar{\mathbf{V}}(x, t) = \langle \bar{\mathbf{V}}(x, t) \rangle + \bar{\mathbf{v}}(x, t) \quad (3.12)$$

Using this decomposition the incompressible form of the continuity equation can be re-written as,

$$\begin{aligned} \nabla \cdot \bar{\mathbf{V}} &= \nabla \cdot (\langle \bar{\mathbf{V}} \rangle + \bar{\mathbf{v}}) = 0 \\ &= \nabla \cdot \langle \bar{\mathbf{V}} \rangle = 0 \quad \text{and} \\ \nabla \cdot \bar{\mathbf{v}} &= 0 \end{aligned} \quad (3.13)$$

Using tensor notations, the Left Hand Side of the momentum equation may be re-written as,

$$\frac{\partial \langle \bar{\mathbf{V}}_j \rangle}{\partial t} + \frac{\partial}{\partial x_i} \langle \bar{\mathbf{V}}_i \bar{\mathbf{V}}_j \rangle \quad (3.14)$$

Implementing the Reynolds decomposition on this will yield,

$$\langle \bar{\mathbf{V}}_i \bar{\mathbf{V}}_j \rangle = \langle \bar{\mathbf{V}}_i \rangle \langle \bar{\mathbf{V}}_j \rangle + \langle \bar{\mathbf{v}}_i \bar{\mathbf{v}}_j \rangle \quad (3.15)$$

The velocity covariances, $\langle \bar{\mathbf{v}}_i \bar{\mathbf{v}}_j \rangle$ are termed as the Reynolds Stresses. The equation (3.15) can be written using the mean substantial derivative (non-conservation form), i.e. using the relation,

$$\frac{\mathbf{D}}{\mathbf{D}t} = \frac{\partial}{\partial t} + \langle \bar{\mathbf{V}} \rangle \cdot \nabla \quad (3.16)$$

Equation (3.6) can be re-written with the application of the mean quantities,

$$\frac{\mathbf{D} \langle \bar{\mathbf{V}} \rangle}{\mathbf{D}t} = \nu \nabla^2 \langle \bar{\mathbf{V}} \rangle - \frac{\partial \langle \bar{\mathbf{v}}_i \bar{\mathbf{v}}_j \rangle}{\partial x_i} - \frac{1}{\rho} \frac{\partial \langle p \rangle}{\partial x_j} \quad (3.17)$$

The only difference between the non-conservation form of the RANS equation and the non-conservation form of the base form of the momentum equation is the presence of the Reynolds stress terms, $\langle \bar{\mathbf{v}}_i \bar{\mathbf{v}}_j \rangle$. To solve these terms, further equations are needed. For this, the Reynolds stress tensors are approximated using either Eddy Viscosity or Reynolds Stress Models. The Reynolds stress terms represent the mixing phenomena by the convective transport as a result of the velocity fluctuations.

The mean turbulent kinetic energy per unit mass is defined here as the half of the trace of the Reynolds stress tensor, i.e.

$$k = \frac{1}{2} \langle \mathbf{v}_i \bar{\mathbf{v}}_j \rangle \quad (3.18)$$

For the interested reader, a statistical description of turbulence can be found in chapter 5 of the book on Turbulence by Westerweel et al [9] and chapter 3 of the book on Turbulent Flows by Pope [50].

3.5. Large Eddy Simulations (LES)

Different numerical simulations have different types of accuracy levels. This accuracy is determined by the degree of approximations made in the system of equation describing the flow. These approximations can be made in the form of grid size (Δx), time steps (Δt), or any other assumption made in the flow parameters to reduce the level of complexity. Large Eddy Simulation (LES) has a level of accuracy and computational power requirement in between that of RANS (section 3.4) and DNS (section 3.6).

The reader would recall the discussion on the energy cascade, wherein the energy from the larger scales are transferred to the smaller scales. LES is responsible to resolve these large scales (RANS resolves only the mean flow scales and models all other scales) and a filter is set up such that it acts as a cutoff. All scales below this cut-off are modelled while the larger ones are resolved.

The following few steps govern the development of LES:

- Filtering the Navier Stokes equations in physical space to represent the largest scales (through the filtered components). The velocity field will be decomposed into the resolved, $\bar{\mathbf{V}}^1$ and the residual Subgrid Scales (SGS) \bar{v}' components
- The set of equations are "closed" using algebraic equations for the Sub-Grid Scale (SGS) eddy viscosity to model the residual stress-tensors
- Numerically solve the equations for the filtered velocity to obtain an approximation for the large scale turbulent flow

These smaller scales are responsible for the development of the turbulent flows. Resolving all the scales is the ideal requirement, but requires immense computational costs and in today's world is limited to flows with lower Reynolds numbers. LES *models* these small scales and as these scales are dominated by viscous effects, there exists many algebraic eddy viscosity models.

Any such viscosity model should satisfy the following requirements:

- Maintain computational stability and provide appropriate energy drain
- LES should tend towards DNS when the filter width is in the order of the small scale structures
- Stress tensors obtained using the model should show good correlation with validated results

The simulations in this master thesis are carried out on ANSYS CFX and as the current version has three such LES models, those will be discussed in the following paragraphs. The details are based on the documentation in ANSYS CFX [51] and the book on Turbulent flows by Pope [50].

3.5.1. Smagorinsky Eddy Viscosity Model

Smagorinsky [52] defined an algebraic relation for the unresolved (SGS) viscosity. using dimensional analysis,

$$\mu_{SGS} \propto \rho l \bar{v}'_{SGS} \quad (3.19)$$

Here, l is the length scale associated with the unresolved motions which can be approximated as the cube root of the mesh volume, i.e. the mesh size ($\Delta = \sqrt[3]{Vol}$).

Using the Prandtl mixing length model, the velocity scales for the unresolved motion can be related to the filtered velocity gradient tensor, \bar{S}_{ij} (introduced in chapter 2 section 2.4.1) as,

$$\bar{v}'_{SGS} = \Delta |\bar{S}| \quad (3.20)$$

Here, $|\bar{S}| = \sqrt{2(\bar{S}_{ij} \bar{S}_{ij})}$. The final Smagorinsky Eddy Viscosity model is therefore,

$$\nu_{SGS} = (C_s \Delta)^2 |\bar{S}| \quad (3.21)$$

C_s is the Smagorinsky constant and this is where one of the major disadvantages of the model arises. The value for this constant is dependant on the flow and mesh resolution. For an isotropic turbulent flow, it has a value of 0.18. The constant is found to vary from 0.065 to 0.25. Another disadvantage is the need for damping functions near the wall.

The no slip wall condition produces strong gradients in the flow dependant variables. Viscosity is the major driving force for the transport processes and how well different models simulate this, determines how well a specific model will perform when the flow near the wall is the subject of investigation.

To capture this gradient, the turbulent viscosity near the wall needs to be damped using a mixing length minimum function and viscosity damping function (f_μ). The mixing length minimum function is defined as,

$$l_{mix} = \kappa \cdot y_{wall} \quad (3.22)$$

The constants can be set by the user on CFX 19.2. y_{wall} is the distance from the wall.

¹The smaller bar ($\bar{\mathbf{V}}$) over the variables define vector quantities as opposed to the longer bar ($\bar{\mathbf{V}}$) defining resolved quantities

On CFX, the default value of the damping function is set to 1 but can be modified based on the function preferred (either Van Driest or Piomelli). For the Van Driest function,

$$f_\mu = 1 - \exp(-\tilde{y}/A) \quad (3.23)$$

Here, $A = 25$ by default and \tilde{y} is the normalized wall distance given by, $\tilde{y} = (y_{\text{wall}}) \cdot \tilde{u}/\nu$. \tilde{u} is the local velocity scale.

For the Piomelli function ($A = 25$ by default for this as well),

$$f_\mu = \sqrt{1 - \exp(-\tilde{y}/A)^3} \quad (3.24)$$

3.5.2. Dynamic Smagorinsky-Lilly Model

To account for the issues faced due to the varying Smagorinsky constant (C_s) in the previous model, Germano et al. [32] in 1991, introduced a model to evaluate the constant using the resolved turbulent velocity scales. Lilly [53] modified this the following year.

The interaction between the smallest resolved scales and the largest unresolved scales is responsible for the stress tensor in the subgrid scales. Two different filters were used relating the subgrid scale stresses on both the filters of different widths. The mesh width acts as the smaller filter width and an explicit filter is added for the larger one (test filter). Figure 3.3 illustrates this (κ is the wavenumber and $E(\kappa)$ is the energy associated at that wavenumber).

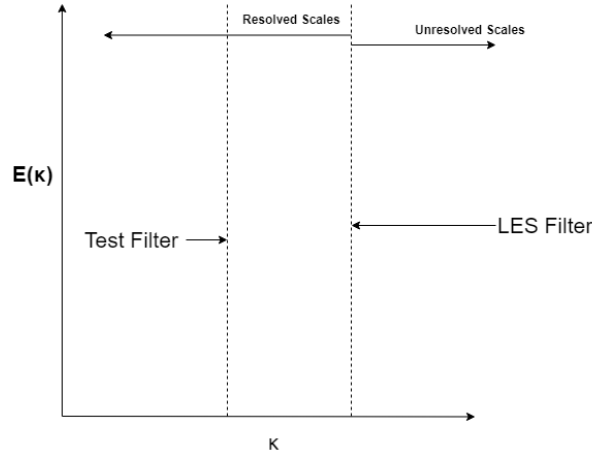


Figure 3.3: Use of two different filters for the Germano model

The filtered velocity is filtered once again using the larger filter width ($\hat{\Delta}$). The width of the test filter is usually twice the width of the smaller ones. The same model constant is used for SGS stress tensor (τ_{ij}) and that for the sub-filtered SGS stress tensor (T_{ij}).

The SGS stress tensor forms on both filters can be given as,

$$\begin{aligned} \tau_{ij} &= \overline{u_i u_j} - \bar{u}_i \bar{u}_j = \frac{1}{3} \delta_{ij} \tau_{kk} - 2(C_s \Delta)^2 |\bar{S}_{ij}| \bar{S}_{ij} \\ T_{ij} &= \overline{\hat{u}_i \hat{u}_j} - \hat{u}_i \hat{u}_j = \frac{1}{3} \delta_{ij} T_{kk} - 2(C_s \hat{\Delta})^2 |\hat{S}_{ij}| \hat{S}_{ij} \end{aligned} \quad (3.25)$$

The Germano identity can be written as,

$$L_{ij} = T_{ij} - [\tau_{ij}] \quad (3.26)$$

Here, L_{ij} is the Leonard stress and this identity is used to connect the model on the filter and that on the test filter. The Leonard stress is given by,

$$L_{ij} = \widehat{\overline{u_i u_j}} - \widehat{u_i} \widehat{u_j} \quad (3.27)$$

Substituting the tensors described in equation (3.25) to equation (3.26),

$$L_{ij}^d = -2C_d \hat{\Delta}^2 |\widehat{S}_{ij}| \widehat{S}_{ij} + 2C_d \Delta^2 \overbrace{|\widehat{S}_{ij}| \widehat{S}_{ij}}^{\wedge} \quad (3.28)$$

Comparing equation (3.28) with (3.21) and concluding that $C_d = (C_s)^2$ will be incorrect, since the model coefficient, C_d , is a function of space and time. Neglecting the spatial variation of the model coefficient will yield an over-determined system and this was worked on by Lilly [53]. A new form for the model coefficient was proposed,

$$C_d = \frac{L_{ij}^d M_{ij}}{M_{ij} M_{ij}} \quad (3.29)$$

Here, $M_{ij} = -2\hat{\Delta}^2 |\widehat{S}_{ij}| \widehat{S}_{ij} + 2\Delta^2 \overbrace{|\widehat{S}_{ij}| \widehat{S}_{ij}}^{\wedge}$.

CFX implements an upper and lower bound for the model coefficient since it varies over a wide range which may lead to numerical instability.

$$\begin{aligned} C_d^{\text{lower}} &= \max(C_d, C_d^{\text{min}}), \quad C_d = 0 \\ C_d^{\text{upper}} &= \min(C_d, C_d^{\text{max}}) \end{aligned} \quad (3.30)$$

The value for C_d^{max} is calibrated on CFX using decaying homogenous isotropic turbulence and is set to 0.04 as default. It should vary between 0.04 and 0.09. The coefficient varies in time according to the following relation,

$$\tilde{C}_d^n = \alpha C_d^n + (1 - \alpha) \tilde{C}_d^{n-1} \quad \text{here } \alpha = 0.01 \quad (3.31)$$

3.5.3. Wall Adapted Local Eddy-Viscosity Model (WALE)

Nicoud et al [54] proposed to replace the traceless symmetric part of the velocity gradient tensor (S_{ij}) by its square. Thus mathematically,

$$S_{ij}^d = \frac{1}{2}(\overline{G}_{ij}^2 + \overline{G}_{ij}^2) - \frac{1}{3} \delta_{ij} \overline{G}_{kk}^2 \quad (3.32)$$

Here, $\overline{G}_{ij} = \frac{\partial \overline{u}_j}{\partial x_i}$. The model is thus formulated as,

$$v_{\text{sgs}} = (C_w \Delta)^2 \frac{(S_{ij}^d S_{ij}^d)^{\frac{3}{2}}}{(\overline{S}_{ij}^d \overline{S}_{ij}^d)^{\frac{5}{2}} + (S_{ij}^d S_{ij}^d)^{\frac{5}{2}}} \quad (3.33)$$

The WALE model implements the correct wall asymptotic variation (y^+) of the SGS viscosity without the need for an additional filter. The model is also capable of reproducing the laminar to turbulent transition. The model constant (C_w) in CFX is calibrated using freely decaying homogeneous isotropic turbulence and is given a default value of 0.5.

3.6. Direct Numerical Simulation (DNS)

The previous sections gave an introduction into the wide range of length and velocity scales characteristic of turbulent flows. Direct Numerical Simulations (DNS) resolve all the scales across the spectrum (in both space and time), from the smallest Kolmogorov scales to the largest. DNS does not rely on modelling the effects of the smaller scales (in contrast to LES).

Resolving all these scales come at a high cost. The numerical grid required is extremely fine and time steps should likewise be small to maintain numerical stability. As an example, consider a grid with number of mesh cells, N_x , N_y and N_z in the x , y and z direction respectively. Consider the Kolmogorov relations,

$$\begin{aligned}
\left(\frac{\eta}{l_l}\right) &\sim \left(\frac{\nu}{u_l l_l}\right)^{3/4} \sim (\text{Re}_l)^{-3/4} \\
\left(\frac{\tau u_l}{l_l}\right) &\sim \left(\frac{\nu}{u_l l_l}\right)^{1/2} \sim (\text{Re}_l)^{-1/2} \\
\left(\frac{\nu}{u_l}\right) &\sim \left(\frac{\nu}{u_l l_l}\right)^{1/4} \sim (\text{Re}_l)^{-1/4}
\end{aligned} \tag{3.34}$$

This leads to,

$$N = N_x N_y N_z = \mathcal{O}(\text{Re}_l)^{9/4} \tag{3.35}$$

Here, Re_l represents the Reynolds number based on characteristic length l .

The penalty paid for in time, scales as follows,

$$T \sim \mathcal{O}(\text{Re}_l)^3 \tag{3.36}$$

Such high computational time requirement makes DNS highly unfavourable to use for realistic flow conditions and complex geometries.

4

Numerical Methodology

This chapter will delve into the geometrical design adopted for the study along with the meshing technique and details of the numerical methodology implemented to attempt and obtain the answers to the questions stated in chapter 2 section 2.5.

4.1. Workflow

The first step in setting up a simulation is to identify the workflow. The process followed in this thesis is shown in the flow chart 4.1.

The process involved setting up the geometry using ANSYS DesignModeler and then moving onto the meshing process using ANSYS ICEM CFD and setting up the simulation with ANSYS CFX. If the results obtained were not in line with expectations/requirements, previous steps were revisited. Thus, the setup was checked and if no problems were found then the meshing was improved and finally changes in the geometry were made if the mesh quality was found to be acceptable but the solutions were still not improving.

4.2. Geometrical Model

The geometry was designed using ANSYS DesignModeler and an illustration of this is shown in figure 4.2. The following are the considerations taken while designing the geometry:

- To avoid the introduction of negative volume elements and singularities during the meshing process, the tip of the cone was blunted by a factor of $1/100^{\text{th}}$ of the cone diameter. This factor was also kept in line with the physical cone used in the experiments by Tambe et al. [5]
- The domain diameter was set to 10 times the diameter of the cone (and motor)
- The domain outlet was kept at a considerable distance from the corner of the cone so that the flow downstream of the cone has enough distance to stabilize and not impact the upstream flow development
- The cone and motor are solid non-deformable surfaces
- The motor surface is considered as a shroud with the actual motor inside and with this assumption the surface is not rotated. This assumption was made for two reasons:
 - Save computational time and power
 - The upstream flow should not be affected by any rotational effects on the flow due to the motor

The process of designing the geometry followed the workflow described in figure 4.1. The initial geometry designs included a shorter length of the motor (shorter H3, i.e. 2 times the cone diameter) and a shorter inlet/outlet diameter (V1, 5 times the cone diameter). This was seen to cause backflow problems at the outlet and divergence in the linear solver of CFX. To circumvent this, the domain diameter and motor length were increased to approximately 10 times and 5 times the cone diameter respectively.

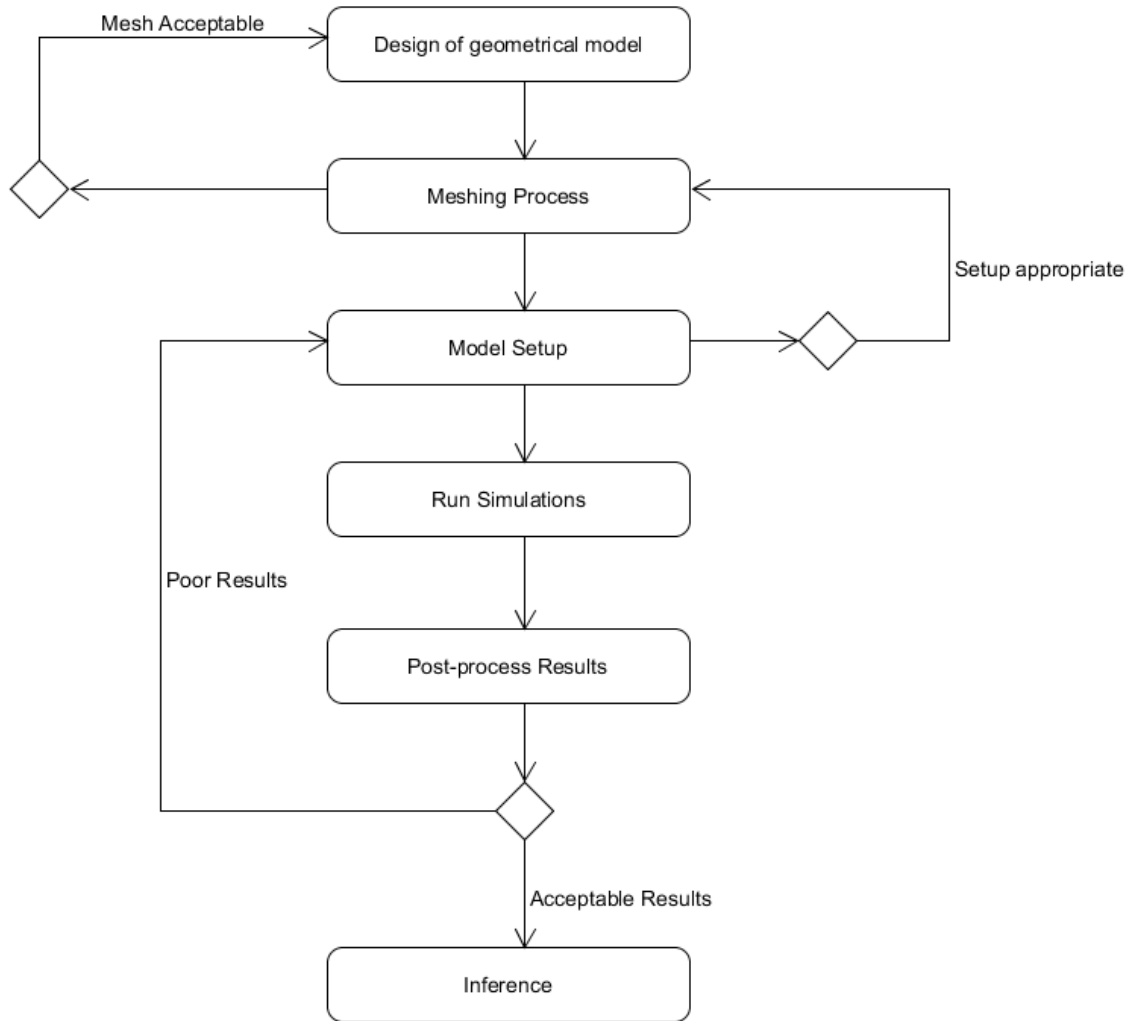


Figure 4.1: Workflow in setting up simulations

A list of all the dimensions and its corresponding dimensionless factors are given in table 4.1.

The global coordinates implemented has its positive x direction from the left to right and the positive y going from the bottom to the top. The positive z direction normal to both x and y is in the out of plane direction facing the reader. The origin of this system is at the tip of the cone.

4.3. Mesh Methodology

The essence of numerical simulation lies in the discretisation process. Meshing is a process to discretize the domain and this has a direct influence on the accuracy of the simulation. Meshing involves striking a balance between the required level of accuracy from the simulation and the available computational time and resources. To this end, the domain was divided into three different sections, upstream, cone region and downstream. The meshing process was undertaken using ICEM CFD.

Keeping in mind the quality requirement of the mesh and that of the solver, in this case, ANSYS CFX, a hexahedral structured meshing technique was used with the blocking represented in figure 4.3. The critical reader would point towards the shape of the domain in the meshing process, this shape does not affect the simulations since each edge is associated with the geometry imported from DesignModeler and thus the final mesh incorporates the shape of the domain.

Another potential comment might be directed towards the edges joining the tip of the cone and the inlet

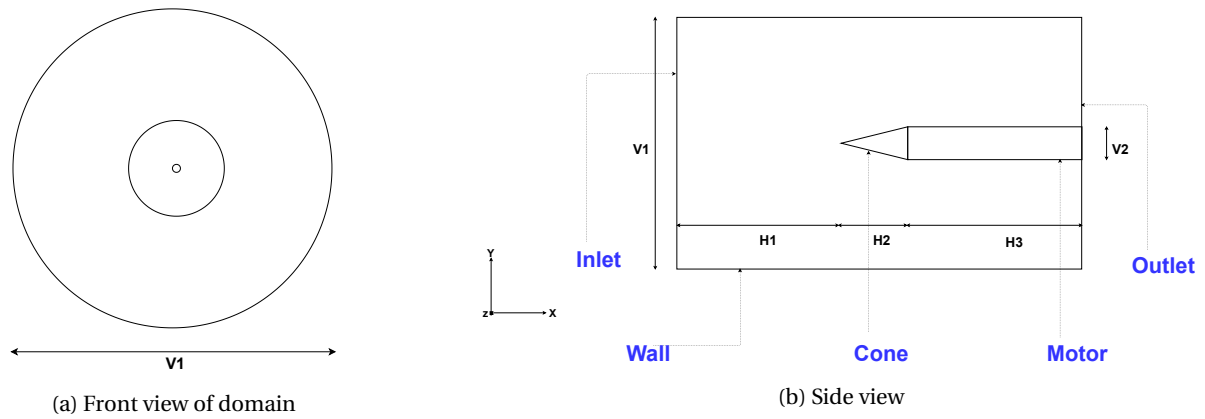


Figure 4.2: Illustration of geometry considered

Geometry Data		
Property	Value	Non-Dimensionalised (wrt cone diameter)
Cone Half Angle (°)	15	N/A
Cone Base Diameter: V2 (m)	0.047	1
Cone tip (m)	4.7×10^{-4}	0.01
Domain Length (m)	0.78	16.59
Domain Diameter: V1 (m)	0.47	10
Motor Length: H3 (m)	0.25	5.31
Upstream Length: H1 (m)	0.4429	9.42

Table 4.1: Dimensional and non-dimensional parameters used to define the numerical model

(seen in figure 4.3b). This was chosen to maintain a high quality mesh and keep the Aspect Ratio¹ of the mesh elements below 1000 as the CFX solver introduces significant numerical errors for meshes with a maximum aspect ratio above this [51].

To generate the mesh an O-grid was created which would wrap around the cone and the motor and run across the entire length of the cylindrical domain. Two factors were taken into consideration for an acceptable mesh, **Quality** and **Aspect Ratio**. For ICEM, these are defined as follows (the details mentioned are taken from the ICEM CFD manual [55]):

- **Quality:** For hexahedral elements, this factor is weighted between Determinant, maximum orthogls² and maximum warpgls³
- **Aspect Ratio:** This is the ratio of the longer element edge to the shorter element edge.

$$AR = \frac{\text{Longer edge length}}{\text{Shorter edge length}} \quad (4.1)$$

The factors which play a role in these metrics include the association (i.e. linking the edges of the blocks to the curves of the geometry), the distribution of nodes along the edges of the blocks and the blocking technique itself. The two meshes generated have 95%+ of their elements above a quality factor of 0.8 and a maximum of 12 elements are within the minimum quality range of 0.01 to 1. These could not be avoided due to the incredibly small diameter of the cone tip. This was the primary reason for the block edges to be diverging from the tip to the inlet. This reduced the number of poor elements significantly. The maximum aspect ratio of the elements was calculated to be 875, with 8 elements between the ratio of 850 to 875 and 88%+ of the elements between 1 and 50. Histograms in figure 4.6 shows the number of elements within different ranges of quality (figure 4.6a) and aspect ratio (figure 4.6b).

Figures 4.4 and 4.5 show the planar views of the front and side view respectively.

¹Defined as the ratio of the longer element edge length to the shorter element edge length [55]

²Evaluates the maximum deviation of the internal angles from 90° of the elements

³This is the maximum warp of the quad faces

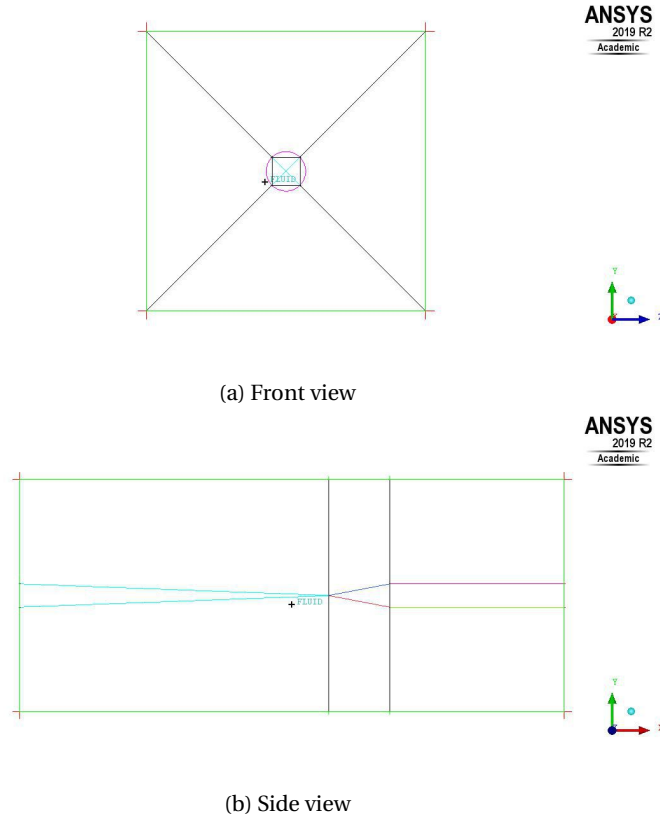


Figure 4.3: Illustration of blocking method implemented

4.4. Case Setup

Figure 4.7 shows an overview of the boundary conditions used across the domain, common for all the cases studied. The flow was from left to right as shown. The shear stress on the far wall was set to 0 Pa, thus a free slip wall. The cone and motor were given no-slip boundary conditions. In addition, a pressure outlet and velocity inlet were used to complete the boundary condition setup. All walls were given adiabatic boundary conditions, thus a thermal study was not conducted.

The setup of the case is based on the objectives defined earlier. The first case, thus, is the setup of the URANS simulation. For this, an axial inflow was used and the cone was rotated. Since running all the possible RANS models to check the one best suited for simulating these spiral vortices is time consuming, the Baseline Explicit Algebraic Reynolds Stress Model (BSL EARS), based on the work by Wallin and Johansson [56], was chosen since the model formulation is such that it captures both the secondary flows and any streamline curvatures with rotating bodies. CFX Pre manual [51] details the implementation of this model in the CFX solver (a small introduction on this model is given in appendix C).

The second case deals with Large Eddy Simulations (LES) of these vortices under axial inflow and rotating cone using the WALE model to this end. Two different meshes were used for this purpose. The point to note here is that none of the meshes provide a y^+ of less than 1 and although it is recommended for LES, this is not done here keeping in mind the exponential requirements in time and computation power. The reader is reminded here of the CFX limitation on the maximum aspect ratio of the mesh of 1000 and having a y^+ of less than 1 requires excessive refinement in the near wall region making the mesh exponentially large.

The final case is the non-axial inflow, implementing an incidence angle of 2° with respect to the x axis. LES WALE is used to study this case as well.

An adaptive time stepping scheme is used to maintain the maximum CFL number of less than 1 for every time step.

$$\text{CFL} = \frac{U\Delta t}{\Delta x} \quad (4.2)$$

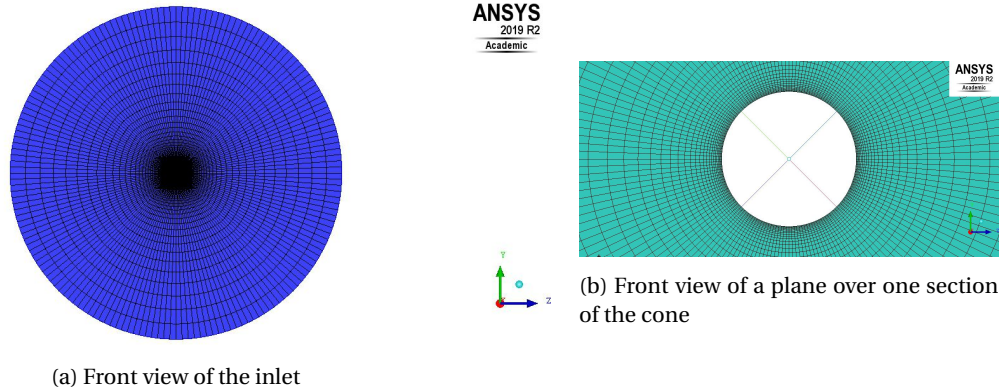


Figure 4.4: Front views of the mesh

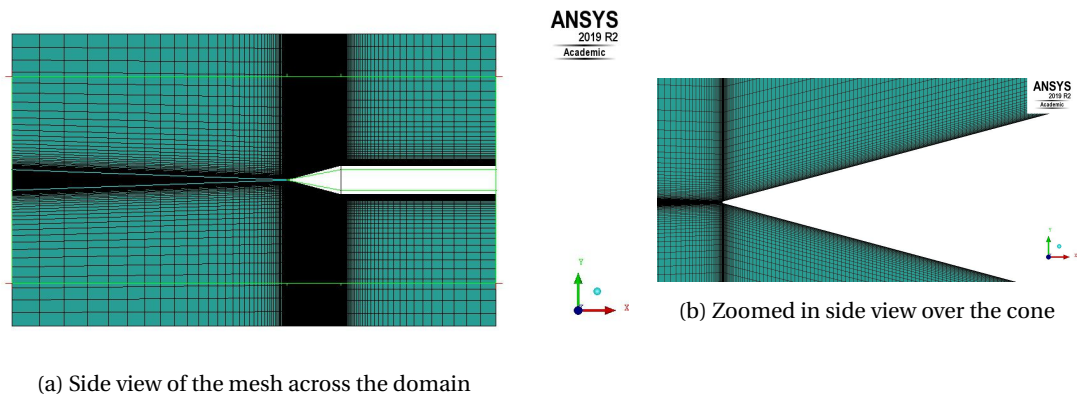


Figure 4.5: Side views of the mesh

Here U is the instantaneous velocity in one mesh element, Δx is the size of the mesh and Δt is the time step. CFX provides the option for adaptive time stepping scheme where the time step adjusts based on a specified maximum CFL Number (it was set as 1 for all simulations). The difference between the timesteps for all cases varied only for the initial few timesteps but remained constant after that. The average time step for all cases are provided in the details section of the cases.

The simulations were run for around 0.2 s which corresponds to the flow rotating around the cone a little over 16 times. To check if this time is sufficient for a reasonable convergence of the transient statistics, two probes over the cone (figure 4.8) were placed and the variations in the velocity components and pressure were monitored.

The location of the probes:

- Probe 1: $X = 0.02$; $Y = 0.015$; $Z = 0$
- Probe 2: $X = 0.02$; $Y = -0.015$; $Z = 0$

The probes are thus placed at diametrically opposite locations over the cone close to the edge of the boundary layer. To confirm this, the monitor data from Mesh 1 for the LES axial flow case was taken. u component of the velocity being in the order of 2.2 m/s which is close to the free stream axial velocity of 2.46 m/s. Figures 4.9, 4.10, 4.11 and 4.12 show that the parameters are approximately stationary by the time they reach 0.2 s. The sharp fluctuations observed at time locations of 0.04 s, 0.09 s and 0.15 s are a result of restarting the simulations from the last backed up file. These are observed at the first iteration of the restart points which die out within 2 to 3 iterations.

Details of each case are given in the following paragraphs.

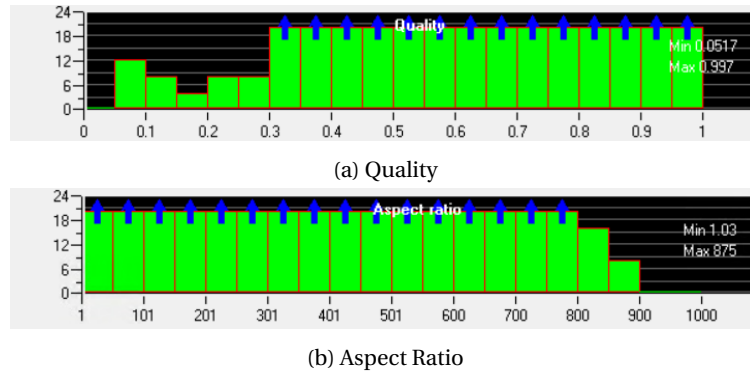


Figure 4.6: Mesh metric histograms

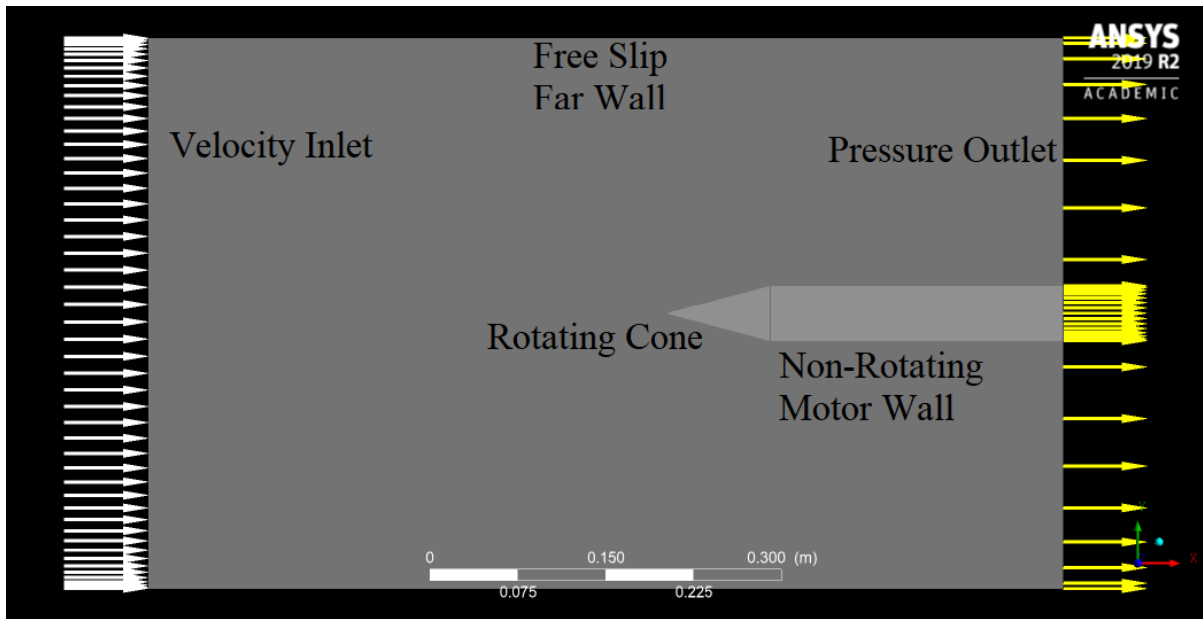


Figure 4.7: Overview of boundary conditions

4.4.1. Case 1

As mentioned earlier, this case uses URANS in an attempt to simulate the vortices over the rotating cone and understand its efficacy. In order to achieve this and validate the results, the flow conditions at the setup were kept the same (to the best possible degree) with those used in the experiments by Tambe et al. [4], [3] and [5]. The parameters used to set up this case on CFX Pre are itemised below:

- Time stepping:
 - Adaptive time stepping scheme based on maximum Courant number of 1
 - Average time step: 9.25×10^{-7} s
- Reference Pressure: 1 atm
- Turbulence intensity: 1 %
- Initialisation:
 - u (x direction) velocity = 2.46 m/s
 - v (y direction) velocity = 0 m/s
 - w (z direction) velocity = 0 m/s

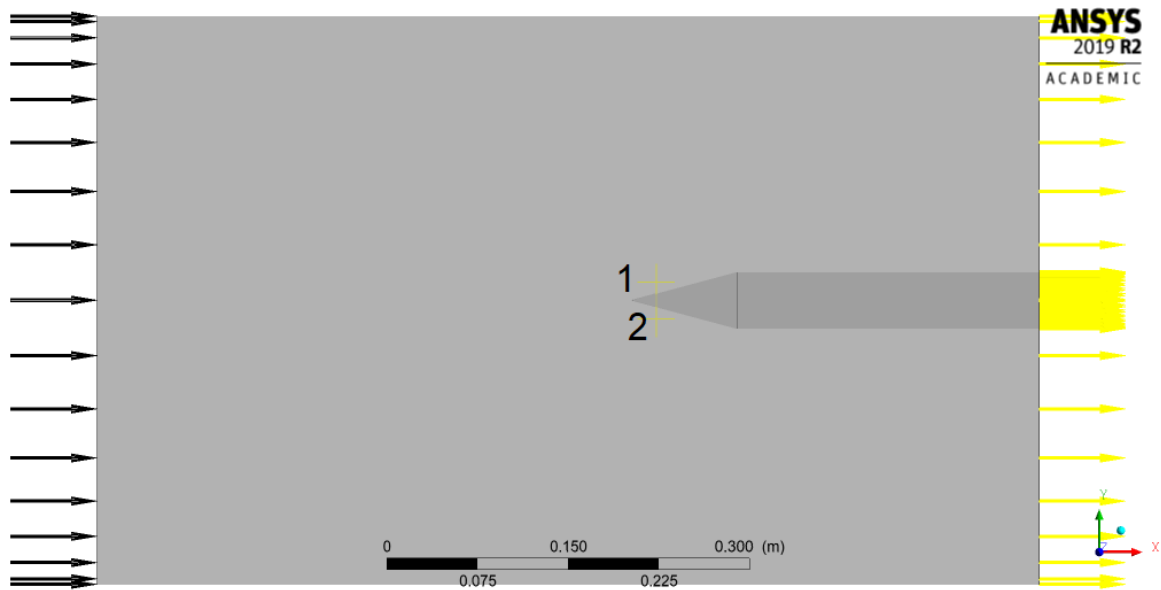
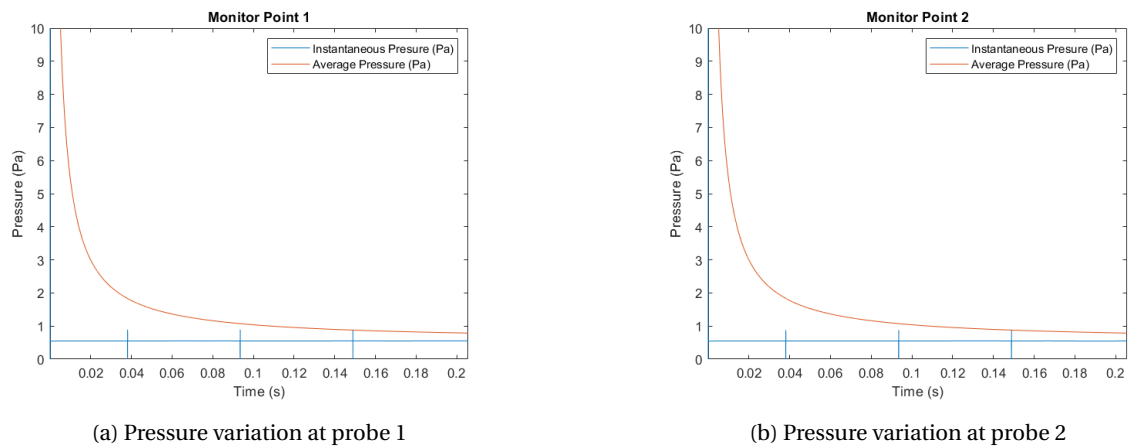


Figure 4.8: Probes for measurement of variations in velocity components and pressure



(a) Pressure variation at probe 1

(b) Pressure variation at probe 2

Figure 4.9: Case 2 - Mesh 1 - Pressure variation at both probe locations

Choice of initialisation made, keeping in mind the diameter based Reynolds number ⁴ of 7.4×10^3 , used in the experiments by Tambe et al. [3].

- Boundary Conditions:

- Inlet:

- ◊ Velocity inlet: $u = 2.46 \text{ m/s}$, $v = 0 \text{ m/s}$ and $w = 0 \text{ m/s}$
- ◊ Low intensity turbulence (1 %)

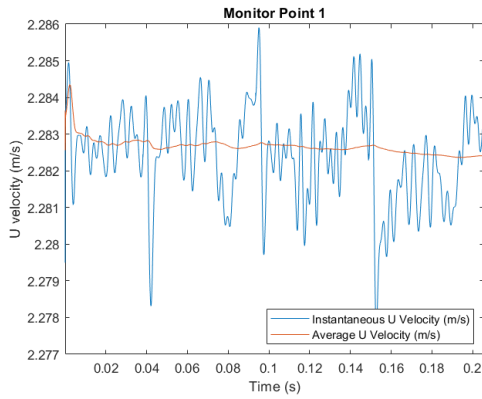
- Cone:

- ◊ No slip wall
- ◊ Rotating wall: 5000 RPM (clockwise)
- ◊ Adiabatic Wall

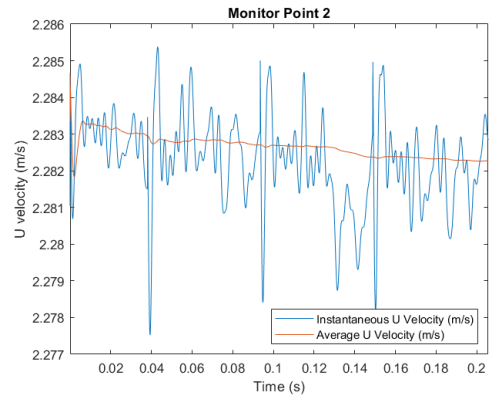
- Motor:

- ◊ No slip wall

⁴ $Re_D = \frac{Dia \times U_\infty}{\nu}$ here, Dia is the diameter of the cone, U_∞ is the inflow velocity and ν is the kinematic viscosity

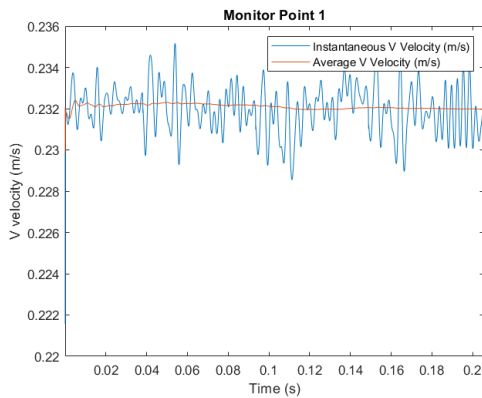


(a) U component variation at probe 1

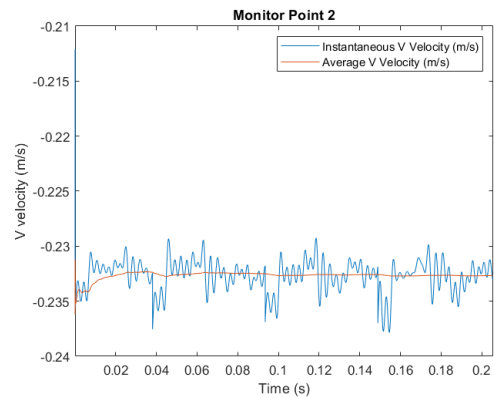


(b) U component variation at probe 2

Figure 4.10: Case 2 - Mesh 1 - U component velocity variation at both probe locations



(a) V component variation at probe 1



(b) V component variation at probe 2

Figure 4.11: Case 2 - Mesh 1 - V component velocity variation at both probe locations

- ◇ Non rotating wall
- ◇ Adiabatic wall
- Outlet:
 - ◇ Static Pressure outlet: 0 atm
- Far Wall:
 - ◇ Free slip wall

The solver settings are itemised below:

- High Resolution Advection scheme
- Second order backward Euler Transient scheme
- Convergence criteria: 2×10^{-6}

4.4.2. Case 2

This case involved numerical simulation using LES for an axial inflow under similar conditions. There were two different mesh sizes implemented. The coarser mesh here is named Mesh 1 and the finer one is named Mesh 2. The input details for both meshes remain the same, the difference lies in the average time stepping.

For the LES cases, the initialisation was done by first running a laminar case with the same boundary conditions used in Case 1 (except for the introduction of turbulent intensity) and the results were used as initial

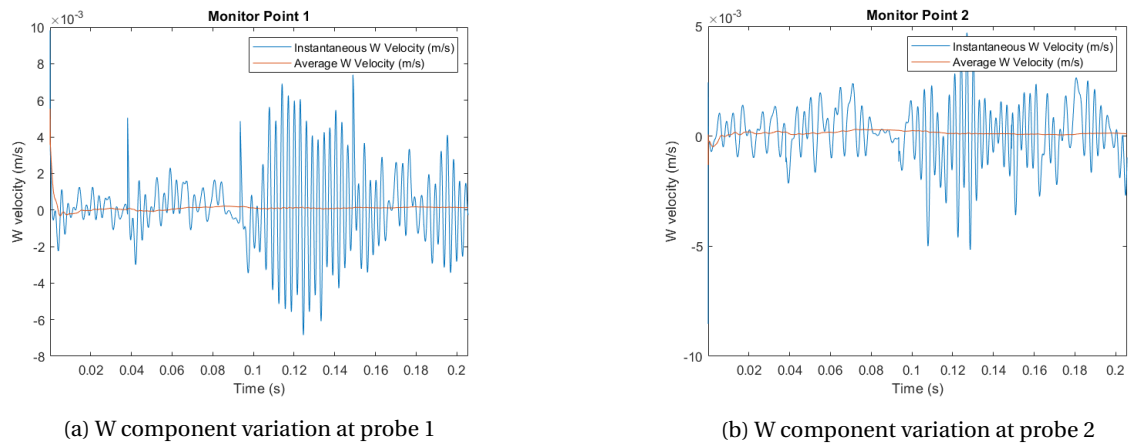


Figure 4.12: Case 2 - Mesh 1 - W component velocity variation at both probe locations

conditions for the LES model. A RANS case was not used as initial conditions since based on the research conducted on the phenomena, the vortices appear in the transition region over the cone, using the turbulent boundary layer generated from a RANS simulation as initial conditions would not be suitable for a flow which originates from a laminar boundary layer. The fluctuations were imparted on this initial condition in CFX Pre.

The parameters for the LES cases are detailed below:

- Time stepping:
 - Adaptive time stepping scheme based on maximum Courant number of 1
 - Average time step:
 - ◊ Mesh 1: 1.319×10^{-6} s
 - ◊ Mesh 2: 9.567×10^{-7} s
- Reference Pressure: 1 atm
- Initialisation:
 - Result file from Laminar run
 - Velocity fluctuation: 1% of inlet velocity
- Boundary Conditions:
 - Inlet:
 - ◊ Velocity inlet: $u = 2.46$ m/s, $v = 0$ m/s and $w = 0$ m/s
 - Cone:
 - ◊ No slip wall
 - ◊ Rotating wall: 5000 RPM (clockwise)
 - ◊ Adiabatic Wall
 - Motor:
 - ◊ No slip wall
 - ◊ Non rotating wall
 - ◊ Adiabatic wall
 - Outlet:
 - ◊ Static Pressure outlet: 0 atm
 - Far Wall:
 - ◊ Free slip wall

The solver settings are itemised below:

- Central Difference Advection scheme
- Second order backward Euler Transient scheme
- Convergence criteria: 1×10^{-5}
 - For each iteration, continuity, U and W momentum reaches order of 10^{-6}

4.4.3. Case 3

For the final case, the conditions were kept the same as in case 2, except that the finer mesh (Mesh 2) was considered and an incidence angle of 2° was given as inflow conditions. The incidence angle (α) is represented in figure 4.13.

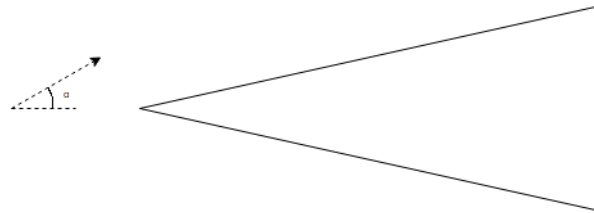


Figure 4.13: Representation of angle of attack (α)

To implement the incidence in the flow, the velocity components from the previous cases were modified such that, $U = U_\infty \cos(\alpha)$ and $v = U_\infty \sin(\alpha)$. With, $U_\infty = 2.46$ m/s, the respective components are, 2.458 m/s and 0.0858 m/s. The remaining parameters were kept the same as case 2.

The average time step for the non-axial case was: 6.904×10^{-7} s.

5

URANS: Axial Inflow

This chapter will delve into the results obtained as a result of running the Baseline Explicit Algebraic Reynolds Stress Model (BSL EARSM), one of the Unsteady Reynolds Averaged Navier-Stokes (URANS) models available in ANSYS CFX.

5.1. Analysis

The URANS model selected for the simulation was based on the Reynolds Stress Model developed by Wallin and Johansson [56], named the Explicit Algebraic Reynolds Stress Model (EARSM). This was selected for the following reasons [51]:

- Due to higher order terms in the formulation, many flow phenomena are included in the model and does not require solving transport equations of the Reynolds stresses. The Baseline EARSM is used to capture the following flow effects ([51]):
 - Secondary flows
 - Streamline curvature and system rotation

Further detail on this model is attached in Appendix C.

The first step in validating whether the selected URANS model was able to capture the formation of these vortices is to check the footprint over the cone left behind by them. Prior to this, a small note on the defining parameters for model setup in ANSYS CFX is given next.

As the name suggests, URANS is an unsteady RANS simulation and thus a transient setup was done. To maintain solver stability, a maximum Courant number of 1 for every iteration was set as a parameter. The CFX solver would then adapt the time step between each iteration based on this parameter and the mesh spacing. For this simulation, Mesh 2, was selected. Although this is a finer mesh, it was chosen so that a direct comparison can be made with the results from the LES case (subsection 6.3). The time steps between iterations remained constant at 9.26×10^{-7} s, making the simulations computationally expensive.

Since the exact turbulence intensity at the inlet was not known, for this model of URANS, a low intensity turbulence setting (1 %) was given as inlet conditions. The longitudinal turbulence intensity, defined as, $\sqrt{\langle U'^2 \rangle} / U_\infty$, was evaluated to be less than 3 %.

To visualise the footprint left behind by these vortices, a wall friction coefficient (C_f) was defined as,

$$C_f = \frac{\text{Wall Shear}}{\frac{1}{2} \rho_\infty U_\infty^2} \quad (5.1)$$

Here, U_∞ is the inlet flow velocity, 2.46 m/s and ρ is the density.

A similar contour plot to that obtained by Tambe et al. [5] (figure 2.24) of C_f would be expected if the turbulence model is successful in simulating this phenomena. Unfortunately, the URANS model selected, Baseline

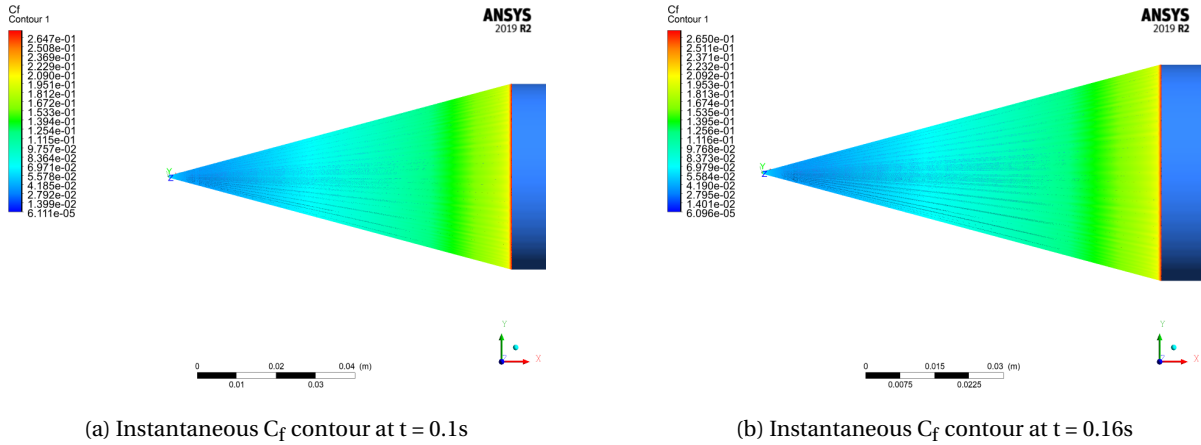


Figure 5.1: Instantaneous contour plots of C_f

Explicit Algebraic Reynolds Stress Model (BSL EARSM) was unable to model this footprint. Two instantaneous contour plots of C_f is shown in figure 5.1.

It is observed that the BSL EARSM model fails to capture these counter-rotating vortices observed in the experiments. The following sections attempt to find an answer to this.

5.2. Potential Cause

There are many potential reasons for why the BSL EARSM was unable to model this phenomena. Two main causes are discussed here.

The first probable cause might be a low turbulence intensity level at the inlet which dampens by the time the flow reaches the cone. To check this, a plot of the turbulent intensity variation with respect to the mean flow was made.

To check the variation, the mean turbulent intensity is defined as,

$$I = \frac{\sqrt{\langle U'^2 \rangle}}{\langle U \rangle} \tag{5.2}$$

$\langle U \rangle$ is the transient mean flow velocity. Figure 5.2 shows the variation along a line across the domain. The line is positioned at $Y/D = 0.85$ (figure 5.2a).

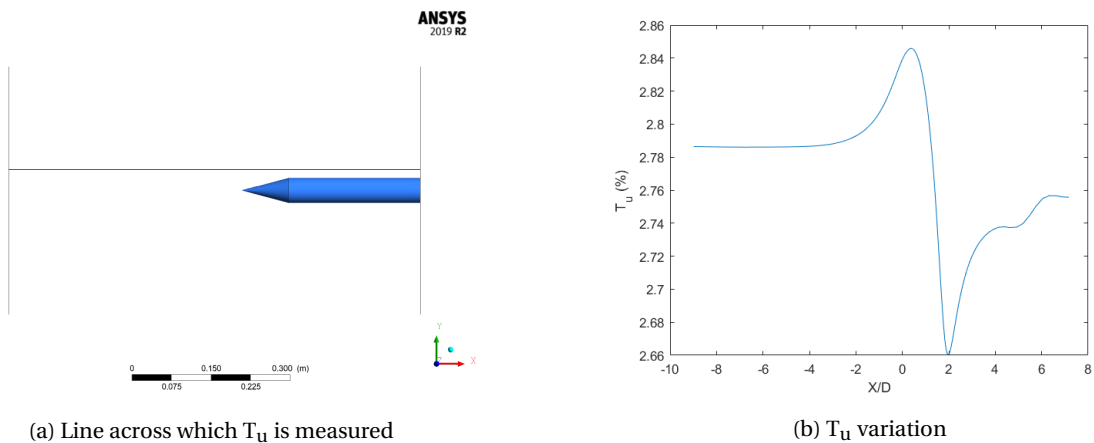


Figure 5.2: T_u (%)

In figure 5.2b, the tip to corner of the cone is between $X/D = 0$ and $X/D = 1.87$. This corresponds to the slight increase near the tip and a gradual decrease over the length of the cone. The reason for the increase in intensity

near $X/D = 0$ is due to the effect of the tip and the rotation of the cone, inducing fluctuations to the upstream flow. Over the length of the cone, this intensity is seen to reduce and this is attributed to the increase in the mean flow velocity as the flow "sees" the section converging.

The intensity is seen to be roughly constant from the inlet and thus a damping of upstream intensity can be ruled out as a potential cause.

Another potential error may be the intensity set was low to begin with, however, experiments by Tambe et al. [5] and Kohama [24] have shown that these counter rotating vortices form even at low inlet turbulence levels (<1 %).

As has been looked into in chapter 3, the foundation of the RANS model is based on splitting the flow into two components, the time averaged component and the fluctuating one. The averaged quantities are then used in the Navier-Stokes equations, to achieve the RANS formulation¹. Upon formulating the RANS equations, unknown terms crop up in the momentum transport equations, known as the Reynolds stress components. Leading to the well known closure problem in turbulence. Additional equations model these Reynolds stresses thus closing the system of equations. RANS models are therefore based on statistical averaging and individual fluctuations are not obtained by simply subtracting the mean from the instantaneous velocity fields. This puts URANS at a disadvantage in visualisation of the vortices and forms the crux of the difference with LES.

As has been touched upon in chapter 3, Large Eddy Simulations are based on scale separation, where the velocity field, instead of separating based on mean and fluctuating component, are separated based on the resolved and residual (unresolved/modelled) scales (illustrated through figure 5.3).

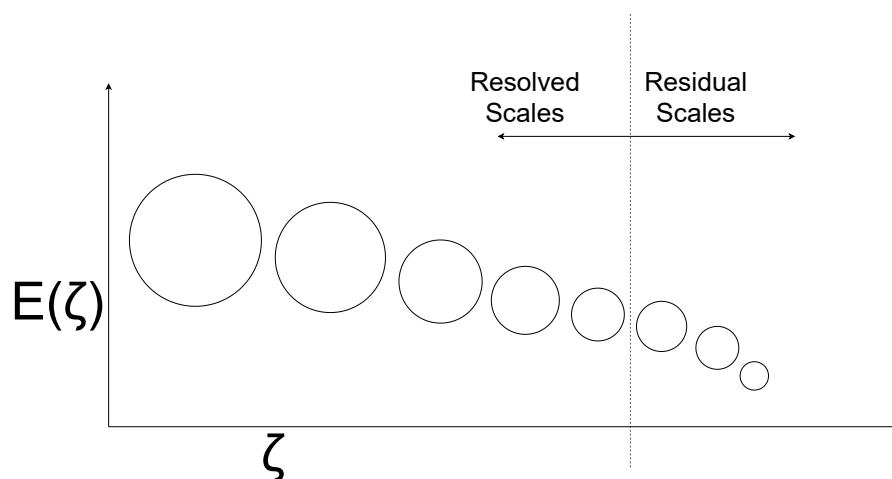


Figure 5.3: Illustration of LES scale separation²

The sub-grid scales (unresolved scales) are modelled in LES. This allows the visualisation of fluctuations by subtracting the mean from the instantaneous flow field.

This thus forms the most likely cause for the URANS model not being able to show the vortices formed over the surface and thus not showing the effects of it over the surface through the C_f contours.

As an ANSYS CFX user, to account for the first cause discussed above:

- A low turbulent intensity setting was chosen at the inlet, since the exact intensity was unknown. If this is not the case for future work and the exact intensity and eddy viscosity ratio is known, then the "Intensity and Eddy Viscosity Ratio" can be selected as the turbulence setting.

¹To model transient simulations, the equations are ensemble averaged, thus obtaining the URANS formulation

² ζ here is the wave-number and $E(\zeta)$ is the energy associated with the scales

6

LES: Axial Inflow

This chapter describes the results from the Large Eddy Simulation of an axial inflow over the cone. Two meshes were built using ICEM CFD, named here as Mesh 1 and Mesh 2. For details, the reader is directed to section 4.4.2. In this chapter, the results obtained using LES will be compared with those obtained in the experiments by Tambe et al. [3] and [5].

6.1. Coordinate System

A wall bounded coordinate system is defined for the analysis of some of the results. This coordinate system was defined by rotating the cartesian coordinate system by 15° (half angle of the cone) with respect to the X axis. With the origin of the cartesian system at the tip of the cone, the origin of the local system remains the same.

The X axis is now wall parallel (X') and the Y axis is wall normal (Y'). Figure 6.1 shows the new coordinate system. This will be used to obtain the wall parallel velocity profiles.

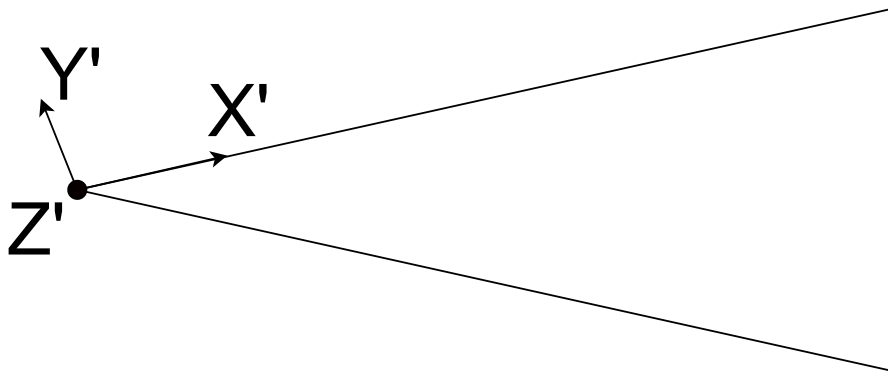


Figure 6.1: User defined local coordinate system

6.2. Mesh 1

This section will describe the results obtained using Mesh 1. This is the coarser of the two meshes with a total node count of 1636710. To recap, the inflow velocity is 2.46 m/s, a no slip, adiabatic rotating wall (5000 RPM) is set for the cone. The motor wall is also set to no slip, adiabatic conditions, but to save computation time, the wall is not rotated and the physical component rotating the cone is assumed to be inside it. Thus, the wall of the motor is acting as a casing. A static outlet pressure of 0 atm is set and the far wall has zero shear stress, thus acting as a free slip wall.

6.2.1. Vortex Footprint

Previous parametric experimental studies have shown that for rotating cones with half angles less than 30° , counter rotating pairs of vortices are formed in the transition region (Kohama [24]). The vortices formed will have a direct impact on the stresses over the surface of the cone. To visualise the footprint left by these vortices, a series of instantaneous wall friction coefficient (C_f) contours were created using ANSYS CFD Post. Figures 6.2 and 6.3 shows the footprints left by the vortices over the surface at different time instants. This coefficient was determined using equation 5.1.

A series of alternating bright and dark spiral patches of wall friction coefficient is observed over the cone. There are black dots observed over the surface of the cone along the azimuthal direction. These are formed due to an insufficient number of contour levels chosen. The choice for the number of contour levels shown using ANSYS CFD Post was made based on the best visual description of the effect of flow over the surface. The brighter patches represent a higher wall friction coefficient which corresponds to alternating up-wash and down-wash (counter-rotating vortices). To confirm this, a contour plot of instantaneous wall normal velocity fluctuations with respect to the mean flow in the meridional plane was made as shown in figure 6.4. The vectors indicate a pair of counter rotating vortices, corresponding to the lighter and darker regions of the contour over the surface.

Both figures (6.2 and 6.3) show a gradual increase in the wall shear from the tip, before reaching an alternating spiral structure at around x/D of 0.6 and reaches its maximum value at the corner of the cone. This high value is expected as the flow reaches a sharp corner where the stresses over the surface will be high, exacerbated due to the rotation of the cone.

6.2.2. Wall Parallel Velocity Profiles

To observe the development of the flow over the surface, the transient mean¹ (over a time period of 0.2 s) wall parallel velocity profiles were taken at different locations. The locations (wall normal lines shown in figure 6.5) are taken at $X/D = 0.8, 1.0, 1.2, 1.4, 1.6$ and 1.8 . Figure 6.6 shows these profiles.

The hollow circles on the various profiles represent the mesh nodes over the cone. The velocities in the profiles are normalised using the inflow velocity, $U_\infty = 2.46$ m/s. The transient mean values of velocity were taken after the simulation was made to run for 0.2 s.

It can be observed from the profiles, the wall parallel velocity gradient initially is quite low ($X/D = 0.8, 1.0$ and 1.2), i.e. the change in velocity data between two successive mesh points. This gradient keeps increasing progressively and this results in higher net wall shear values.

The profile at axial location, $X/D = 0.8$, shows a smooth transition from being near zero at the wall (the value is not exactly zero since CFD Post provides conservative values²)

For $X/D = 1$, the profile indicates the addition of wall parallel momentum. At around $Y'/D = 0.01$, i.e. very near the wall, a region of disturbance is observed. The boundary layer region at this location can be said to extend till $Y'/D = 0.06$ as the velocity is significantly less than the inflow velocity.

Replicating the addition of momentum near the wall, observed in the experiments by Tambe et al. [5] was attempted through the simulations. To this end, the wall parallel transient mean (over a time period of 0.2 s) velocity contour was plotted.

Figure 6.7 shows the contour in the region within $X/D = 0.8$ to 1 . The contour shows a region of higher velocity near $X/D = 1$ as was observed through the profile (figure 6.6). The mesh being a coarse one, does not fully capture this momentum increase in detail. To further resolve the boundary layer, the maximum y^+ value should be ~ 1 which was not the case for either of the meshes in this thesis.

6.2.3. Wall Friction Coefficient Variation

Sub section 6.2.1 showed the footprint left by these vortices over the surface. A series of planes (every 5°) were created in the circumferential direction and wall shear values were taken along the lines intersecting between the plane and the wall of the cone. To characterise the growth of the spiral vortices, a circumferential

¹ANSYS CFX provides the transient average of the velocity data for LES

²Conservative values in CFD Post are those obtained on the boundary vertices. They are representative of the control volume over which the equations are solved rather than the boundary itself and thus may not exactly be zero on no-slip walls

mean was taken and subtracted from the wall shear values for every plane, thus providing a fluctuating wall shear profile. This wall shear value was then normalised by the free stream dynamic pressure to obtain the fluctuating C_f . This process was then repeated for a few available time steps and the RMS was taken to obtain one final profile along the meridian of the cone, shown in figure 6.8.

The profile (figure 6.8) shows a dramatic increase in C_f fluctuations from $X/D = 0.5$. This dramatic increase in the fluctuations represents the point at which the vortices start to have a higher impact over the surface of the cone. This is called the critical point and was also studied by Tambe et al. [3] using the IRT setup with the physical process explained by Tambe et al. in [5]. The profile of RMS values of the digital pixel intensity fluctuations (I'_{RMS}) obtained in the experiments are shown in figure 6.9. The reader is directed to the experiments conducted by Tambe et al. [3] to know more about the methodology.

To define a criterion for the critical point, a spatial moving mean (sliding window length: 25) of the fluctuations were taken to smoothen the curve. This leads to two regions of linear curve in the plot, the initial stage before the formation of the coherent structures and the other is the rise in fluctuations over the transition region. The intersection provides the critical point. This is shown through figure 6.10.

Mesh 1 under predicts the critical point when compared with experiments by Tambe et al. [5]. This can be explained by the following:

- Mesh points over the surface are not fine enough, i.e. the spatial distance between the nodes is large thus the location of the rise can be under-predicted. In general, for numerical simulations, variable data is evaluated for the entire cell, i.e. one value is obtained across the cell region. Thus, in this case, each wall shear data obtained would span a larger area over the surface and thus the rise is under-predicted with respect to the experiments by Tambe et al. [5]
- To obtain the profile for the simulations, only a few time steps were taken. This is not ideal and RMS profiles are obtained by taking all the available timesteps. In the experiments by Tambe et al. in [3] and [5], 2000 images were taken at a rate of 200 Hz, thus giving ample data points for an accurate analysis

The experiment profile (figure 6.9) shows a clear peak, depicting the point of maximum amplification of the vortices. This peak is not clear in the numerical simulations (figure 6.10), which can again be attributed to, a) The same reason as the second point above and b) The corner of the cone impacting the accuracy of the results.

6.2.4. Local Reynolds Number Variation

A local Reynolds number was defined to study the variation of Reynolds number along the meridional plane of the cone.

To be consistent with the experiments by Tambe et al. [5], this local Reynolds number was defined as,

$$\text{Re}_l = \frac{u_e l}{\nu} \quad (6.1)$$

u_e is the transient mean streamwise velocity of the flow at the edge of the boundary layer. To evaluate this, the velocity corresponding to the location where the out of plane vorticity approached zero, was taken as the reference. In this case, the vorticity value taken was 0.015% of the maximum vorticity. l is the distance along the meridian measured from the tip of the cone. ν is the kinematic viscosity.

This local Reynolds number was measured against the local rotation ratio, S . This is defined as,

$$S = \frac{r\omega}{u_e} \quad (6.2)$$

Here, r is the local radial location and ω is the rotational velocity of the cone.

Using this, figure 6.11 shows the local Reynolds number plot against S .

The profile obtained by the experiments covering the entire length of the cone is based on the power-law fit, defined, $u_e = CU_\infty l^m$. C and m are constants. The measurement area for the experiments were between $l/D = 0.8$ to 1.8 .

The initial discrepancy in the profile can be attributed to the use of a power law fit for the experiments. This has more credence when the profile between $S = 2.5$ and $S = 4.5$, where the profile shows a good match, since the experimental data was collected between those regions.

There are some outliers present in the data collected from the numerical simulation, leading to the jagged appearance of the profile between $S = 2$ and $S = 4.5$.

The critical local Reynolds number ($Re_{l,c}$)³, obtained through the simulations was 3.356×10^3 and that obtained from the experiments was 5.692×10^3 . This under-prediction is explained by the under-predicted critical point described in the previous section.

The critical Reynolds number through the simulations is located at a local rotation ratio of 1.407 and for the experiments (by Tambe et al [5]) it was at around 2.40. Here too the under-prediction can be associated with the under-predicted critical point since the local rotation ratio is a factor of the local radius. The impact of the boundary layer edge velocity is not significant, since the out of plane vorticity taken was minuscule and thus the velocity associated with it was close to free stream conditions.

6.3. Mesh 2

The section will look into the results obtained by the finer mesh, named in this thesis as Mesh 2. For details the reader is directed to chapter 4 section 4.3. The total node count for this mesh was 2777465. The boundary conditions and initial conditions were kept the same as described in the previous section.

6.3.1. Vortex Footprint

As with the previous section 6.2.1, the vortex footprints left over the surface of this mesh were also observed. Figure 6.12 and 6.13 shows the instantaneous C_f contour over the surface.

There is no significant change observed in the general pattern of the wall friction coefficient. As with the previous section, the development of the spiral vortex distribution is observed through the four instantaneous snapshots. The interesting difference between this and the other mesh is the predicted maximum wall friction coefficient, which is higher for Mesh 2. This can be attributed to the lower spatial distribution of mesh nodes along the surface of the cone, thus providing more accurate results. This may be corroborated through future experiments measuring the wall friction coefficient values or by completing this simulation run, using all the time step data and obtain a correlation between the surface temperature fluctuations (represented using digital pixel intensity) measured in the experiments by Tambe et al. [5] and the wall friction data obtained in the simulations.

To visualise the counter rotating vortex simulated using Mesh 2 for this case, the wall normal velocity fluctuation contour was plotted between $X/D = 1.45$ and 1.6. Figure 6.14 shows the resulting counter rotating vortex.

6.3.2. Wall Parallel Velocity Profiles

As with sub section 6.2.2, the wall parallel velocity profiles at different axial locations was studied for this mesh. The locations were kept the same, i.e. $X/D = 0.8, 1.0, 1.2, 1.4, 1.6$ and 1.8 (as shown in figure 6.5).

Figure 6.15 shows the transient mean wall parallel velocity profiles obtained through the simulations.

The impact of the finer mesh is prominent through figure 6.15. The first thing which stands out is the greater number of mesh points within the boundary layer providing a more detailed profile.

At $X/D = 0.8$, the previous mesh showed a smooth shape in wall parallel velocity from the wall to the outer edges of the boundary layer (figure 6.6), this indicates that the momentum addition phase has already occurred before $X/D = 0.8$, this is expected since the vortices have already been deemed to start forming at around $X/D = 0.5$ (sub section 6.2.3).

The boundary layer region obtained using Mesh 2 is also extended with respect to Mesh 1 and this too will be expected since there are more number of mesh nodes near the wall, thus modelling the near wall region to greater detail. The velocity predicted by the finer mesh is also greater and this agrees with the greater wall friction coefficient values obtained earlier, as an increased flow over the surface will generate higher stresses.

³Reynolds number at the critical point (l_c)

To compare how Mesh 2 performed in replicating the near wall momentum addition, transient mean wall parallel velocity contour between $X/D = 0.6 - 1$ was plotted. This is shown through figure 6.16. With the refinement in the near wall region, the increase in the momentum is clearly visible (increase in the area of higher wall parallel velocity).

6.3.3. Wall Friction Coefficient Variation

The procedure for obtaining the fluctuating wall friction coefficient distribution along the meridian of the cone is the same as described for the previous mesh (subsection 6.2.3). Figure 6.17a shows this profile.

As observed there are multiple corners along with the profile as a result of using an insufficient number of time steps. To overcome this and have a holistic study, a moving mean in space (sliding window length: 25) was taken to obtain the profile shown in figure 6.17b.

In figure 6.17b, the RMS digital pixel intensity fluctuation (I'_{RMS}) profile obtained by Tambe et al. [5] is overlapped. This is done to compare the location of the critical point, i.e. the point at which the vortices are deemed to start to grow.

As seen, this location is under-predicted by the simulation and the same reasoning as with Mesh 1 follows for the finer mesh.

The predicted critical point is also lower for Mesh 2 ($X/D = 0.4010$) when compared with Mesh 1 ($X/D = 0.4511$). This indicates that the spatial mesh refinement may not be the major determining factor in the critical point calculation. A potential contributing factor in the critical point is the SGS viscosity modelled in the near wall region by the turbulence model. This prediction is based on the model constant used (C_w , for the WALE model). For the simulations, the CFX default value for C_w was taken, 0.5. This value is set based on a calibration using freely decaying homogeneous isotropic flow [51]. If the SGS viscosity is under-predicted, the critical point would occur earlier and thus a possible suggestion is to increase the value of C_w and re-calculate this point.

The following section provides a comparison of the critical Reynolds number obtained through Mesh 2 and compares it to that obtained from Mesh 1.

6.3.4. Local Reynolds Number Variation

Using the critical point found in the previous section, figure 6.18 shows the variation of the local Reynolds number with the local rotation ratio.

Figure 6.18 shows that with Mesh 1 (figure 6.11), there remains quite a few outliers at various mesh points for higher S , but there is a qualitative agreement in the trend of the local Reynolds number variation with that in experiments conducted by Tambe et al. [5]. The difference lies in the critical local Reynolds number ($Re_{l,c}$).

The simulations indicate (based on the criterion defined previously) that the critical Reynolds number is 3.095×10^3 and occurs at a rotation ratio of 1.404. This when compared to the results obtained through Mesh 1, wherein the critical Reynolds number was 3.356×10^3 at $S = 1.407$.

Mesh 2 shows an earlier point for the critical Reynolds number (compared to Mesh 1), with all other parameters having kept constant, the finer mesh seems to have shown an earlier point for the growth of the coherent vortical structures. Although the rotation ratio difference is not large (compared to Mesh 1 and this difference is attributed to the lower local radius, since the X/D location of the critical point was seen to be 0.4010 as compared to 0.4511 for Mesh 1), the reason for the larger difference in Reynolds number is seen when examining the logarithmic variation in Reynolds number from figure 6.18.

The difference with the experiments by Tambe et al. in [5] is once again attributed to the under-predicted critical point.

6.4. Spatial Distribution of Vortices

The next part of the study involved analysing the distribution of these spiral vortices along the circumference (azimuthal direction) and how the number of vortices developed along the length of the cone.

The reader is taken back to subsections 6.2.1 and 6.3.1 where the contour plot of the instantaneous wall friction coefficient was used to visualise the imprint of these vortices, i.e. its spiral distribution.

Using the same principle, several axial locations were chosen in between $X/D = 0.6$ and $X/D = 1.8$. The choice of these two endpoints followed the following reasoning:

- The number of vortex pairs (n) along the entire circumference was counted based on the number of peaks in the fluctuating wall friction coefficient (wrt the mean flow) values (one pair of maxima and the minima in the wall friction were counted as one pair of vortices). Analysing the data, the peaks were prominent between these two regions. As the vortices were still in the process of formation in the region before $X/D = 0.6$, uncertainty may have crept into the analysis. After $X/D = 1.8$, the corner of the cone plays a role in the shape of these vortices and thus data points in that region were not taken.

As an example, figure 6.19 shows the entire circumferential variation of C_f for Mesh 2 at $X/D = 0.9$ (with the maxima marked), here there are 6 peaks and thus concluding that the simulation captured 6 pairs of spiral vortices.

This process was repeated on all the axial locations for both meshes. Figure 6.20 shows the result of this analysis compared with those obtained in the experiments by Tambe et al. [5].

The experiments by Tambe et al. [5] measured the surface temperature fluctuations in the azimuthal direction and used the same method in extracting the number of pair of azimuthal vortices.

Best fit for the simulations were made using the power law with the equation of the form, $y = f(n) = aS^b + c$. Here, a , b and c are constants. The equation, defining the variation for both meshes (and the polynomial form used in the experiments by Tambe et al. [5]) were:

- Mesh 1: $n = (49.17S)^{-4.538} + 4.224$
- Mesh 2: $n = (103.1S)^{-5.906} + 5.937$
- Experiment: $n = 138.96 \exp\{-1.25S\} + 8.3$ [5]

The captured number of vortex pairs in the simulation depends on the spatial distribution of mesh nodes along a) the circumference and b) along the wall normal direction. The effect of a finer mesh (Mesh 2) in capturing these vortices is seen through figure 6.20. Mesh 2 captured more number of vortex pairs in general compared to Mesh 1.

To quantify the above statement, table 6.1 shows the azimuthal spacing and the first cell height used for Mesh 1 and Mesh 2 respectively. The number of vortex pairs simulated at 3 different axial locations (X/D) is also shown to highlight the difference in the number of small wavelength perturbations (small scale vortices) simulated by the two meshes.

	Axial Location (X/D)			Azimuthal spacing (m)	First cell height (m)
	0.7	1.25	1.7		
Mesh 1	6	4	4	0.00079	9.20E-05
Mesh 2	6	6	8	0.00066	6.94E-05

Table 6.1: Discretization Effect

Figure 6.20 clearly shows that neither of the currently used meshes is fine enough to provide results close to the experiments. The difference between the simulations and experiments being at least one order of magnitude in the initial rotation ratios.

6.5. Conclusions

A 15° half angle cone, rotated at 5000 rpm under an axial inflow of 2.46 m/s was simulated using the WALE model of LES. Two meshes were chosen to study the formation of counter-rotating vortical structures observed over the rotating cone through experiments.

A wall friction coefficient (C_f) was defined using the wall shear normalised by the free stream dynamic pressure. This was used to visualise the footprint left by the vortices over the surface cone, as they would have a

direct impact over the cone through wall shear stresses. WALE was able to capture this for both meshes with varying accuracy. The finer mesh (Mesh 2) predicted a higher C_f .

To study the development of the spiral vortices over the surface, a set of 36 planes were created on CFD Post and the wall shear data was extracted after which the mean was subtracted from individual planes to obtain a fluctuating C_f data, and RMS was taken to obtain a single profile for the entire cone. This was repeated for several time steps (between 0.1 s and 0.2 s) and another RMS was taken (in time) for analysis.

The profile indicated a spatial delay in the formation of these coherent structures as they were relatively small in the initial stages before increasing at around $X/D = 0.4$. Based on this, a critical point (l_c) was defined. To set a criterion for this point, a spatial moving mean (sliding window size: 25) was taken to smooth the curve. This led to two regions of linearity over the curve and a first order polynomial fit was taken over the two regions. The intersection of the two fits provided the critical point.

With the geometrical parameters, inflow conditions, and cone rotation rate the same as used in the experiments by Tambe et al. [5], Mesh 1 predicted the critical point at around $X/D = 0.45$ and Mesh 2 at around $X/D = 0.40$. The experiments conducted by Tambe et al. [5] predicted this at around $X/D = 0.8$ (although the vortices were seen at around $X/D = 0.5$). This under-prediction can be attributed to the spatial distribution of the mesh nodes along both the axial and azimuthal direction. The under-prediction by Mesh 2 with respect to Mesh 1, however, indicates that mesh spacing might not be the major determining factor in the calculation. The SGS viscosity (modelled by WALE) in the near wall region plays a critical role and if under-predicted, the critical point will be under-predicted as well. The model constant plays an important role in this, and increasing C_w from the CFX default of 0.5 might bring the critical point calculation closer to the experiments.

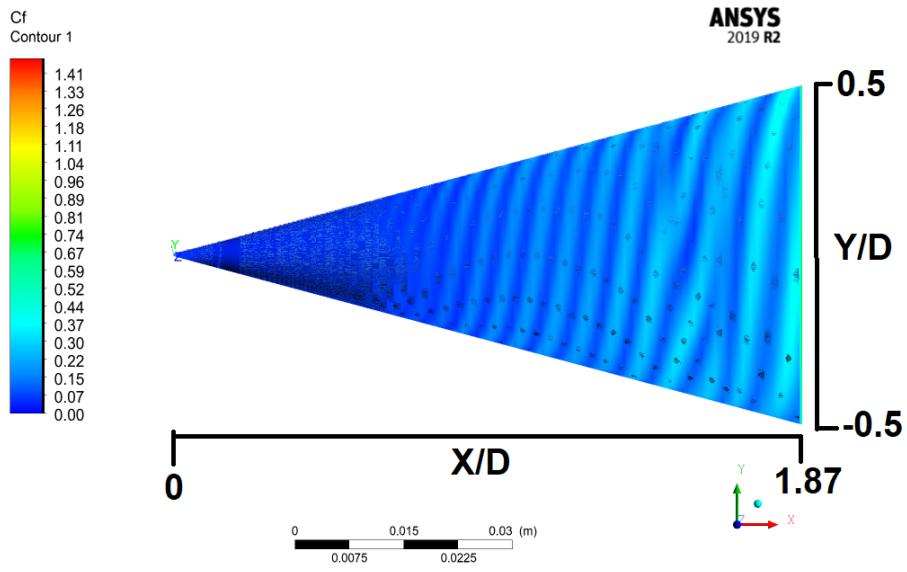
The need for a spatial moving mean profile (sliding window length: 25) arose because the RMS profiles of C_f fluctuations showed constant corners along with it. This is a consequence of not having taken enough timesteps for the RMS data analysis. Due to limitations in the data collection, all the timesteps could not be taken, this is addressed in chapter 8.

A critical local Reynolds number was defined, as the local Reynolds number (Re_l , equation 6.1) at the critical point. This local Reynolds number was plotted against local rotation ratio (S , equation 6.2). Mesh 1 predicted this critical Reynolds number at 3.356×10^3 with the corresponding local rotation ratio at 1.407. In contrast Mesh 2, predicted the critical Reynolds number to be earlier, 3.095×10^3 and thus at a lower rotation ratio of 1.404. The experiments by Tambe et al [5] on the other hand observed this critical Reynolds number to be further along at 5.692×10^3 with a local rotation ratio of 2.40. The reason for the under-prediction by the simulations in comparison to the experiments may be chalked down to the simulations having not yet run to completion and thus as the simulation progresses, this location may vary. A possible method to check this would be to check the monitor data at different probe locations (in this case, two probes were used as discussed in chapter 4). The u velocity component data for both probes shown through figures 4.10a and 4.10b shows a gradient and thus implies that the simulation has not run for sufficient timesteps.

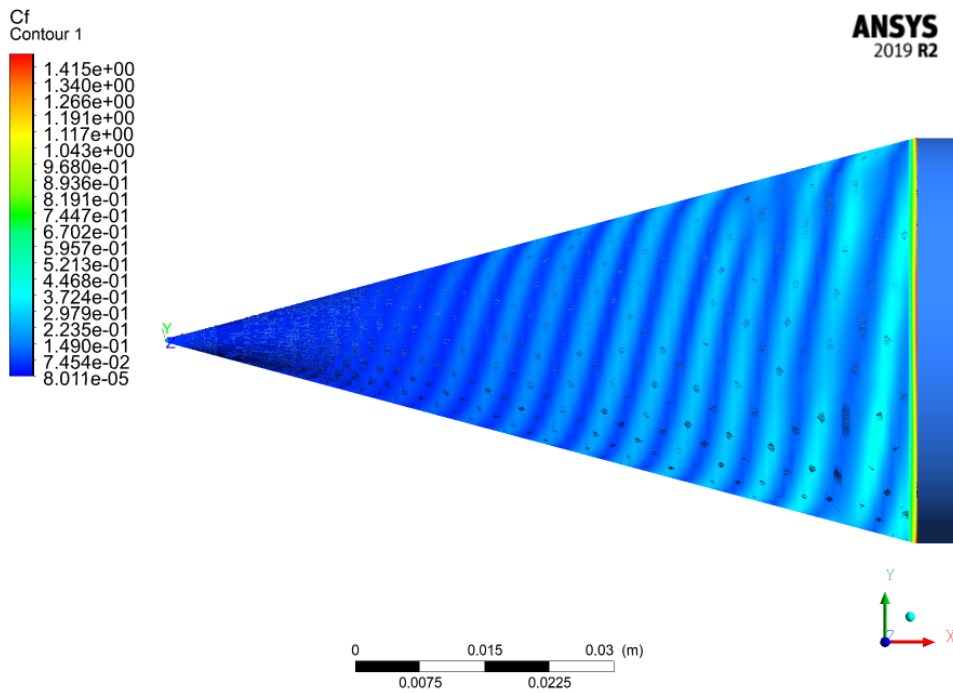
To study the distribution of these vortices along the axial length of the cone, the number of vortices was checked. For this, several axial locations between $X/D = 0.6$ and $X/D = 1.8$ were chosen. This range was taken, as the C_f variation showed the formation of vortices from $X/D = 0.4$. The corner of the cone at just more than $X/D = 1.87$ can affect the vortex structures and thus a maximum of $X/D = 1.8$ was taken.

To count the vortices, the peaks of fluctuating C_f (wrt the mean flow) along the azimuthal direction were counted and the best fit was taken along the length (for corresponding local rotation ratio).

The general trend does not seem to agree with the experiments. With the simulated number of vortex pairs not changing after a local rotation ratio of 3. The reason for this is currently unclear and further investigation is needed. The number of vortex pairs was also under-predicted and this can be explained by the azimuthal spacing of mesh nodes. To verify this, the finer mesh showed a slightly higher number of vortex pairs than the coarser one but not nearly fine enough to quantitatively agree with the experiments.

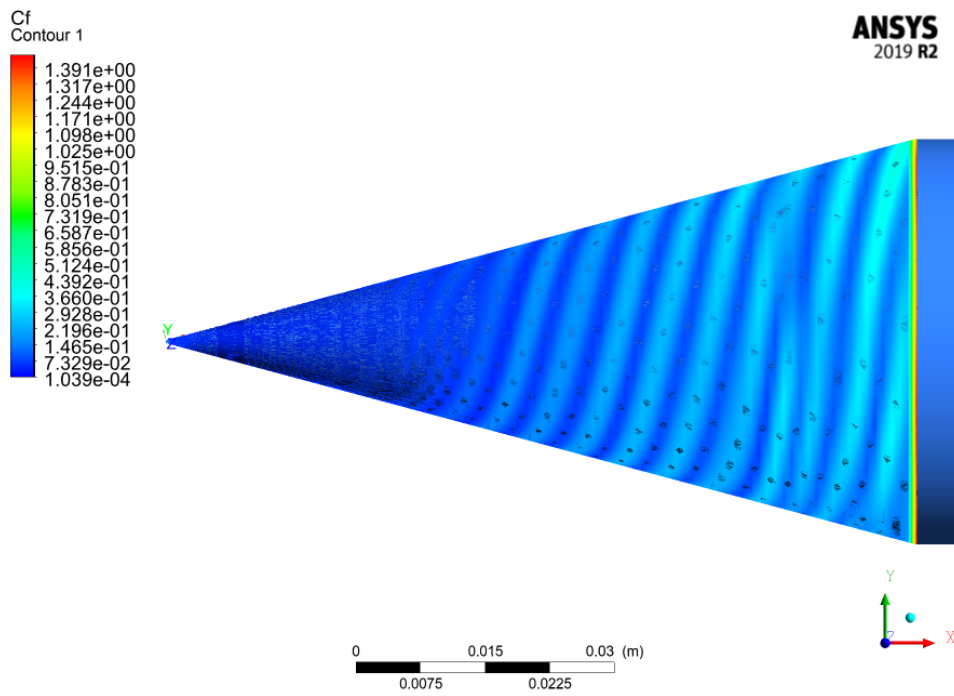


(a) Instantaneous C_f contours at 0.1 s

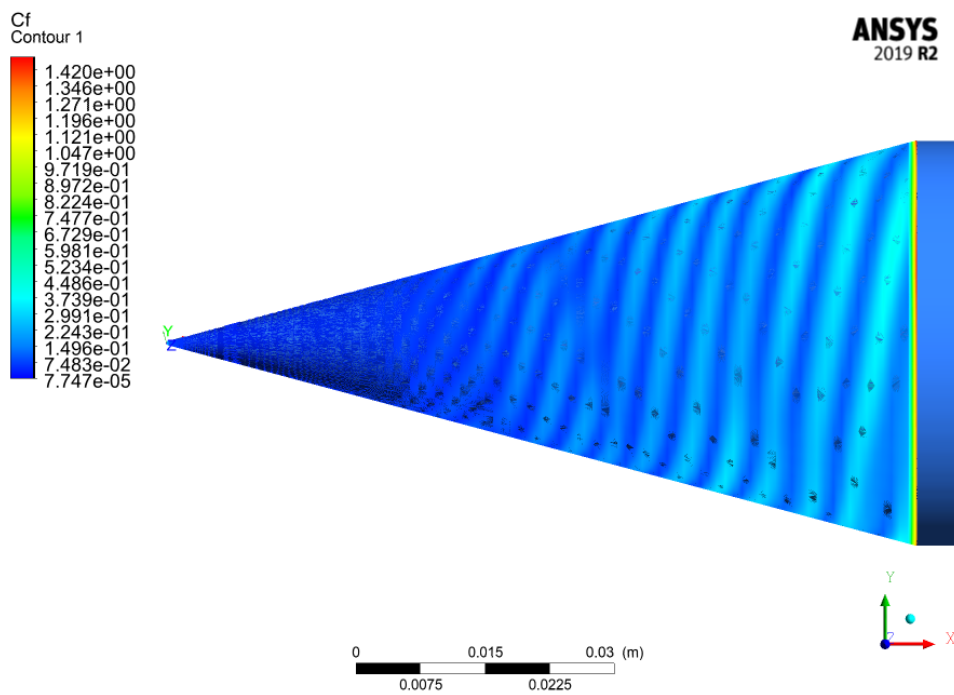


(b) Instantaneous C_f contours at 0.13 s

Figure 6.2: Mesh 1 - Instantaneous (C_f) contours (Instantaneous physical time = 0.1 s and 0.13 s)



(a) Instantaneous C_f contours at 0.15 s



(b) Instantaneous C_f contours at 0.2 s

Figure 6.3: Mesh 1 - Instantaneous (C_f) contours (Instantaneous physical time = 0.15 s and 0.2 s)

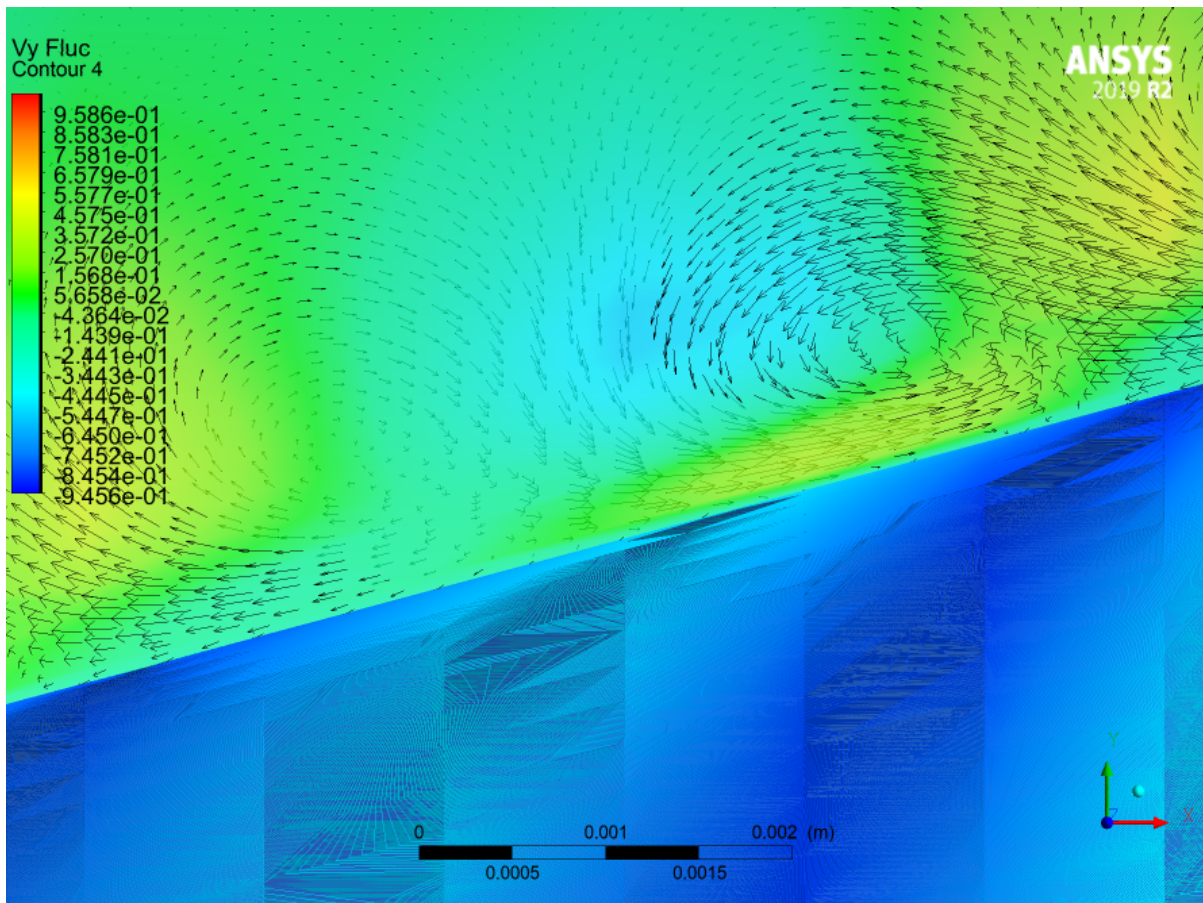


Figure 6.4: Mesh 1 - Wall normal velocity fluctuation Contour

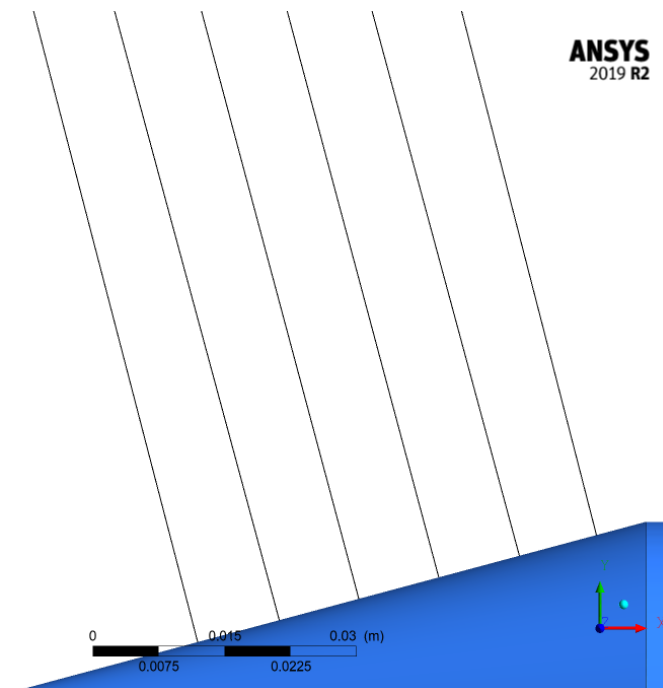


Figure 6.5: Axial locations for velocity profiles

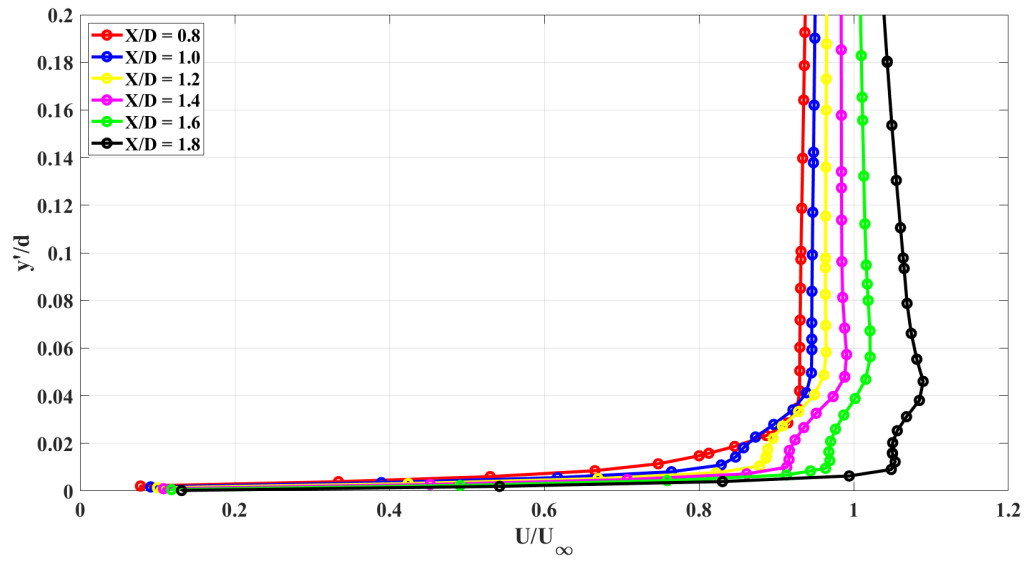


Figure 6.6: Mesh 1 - Velocity Profile

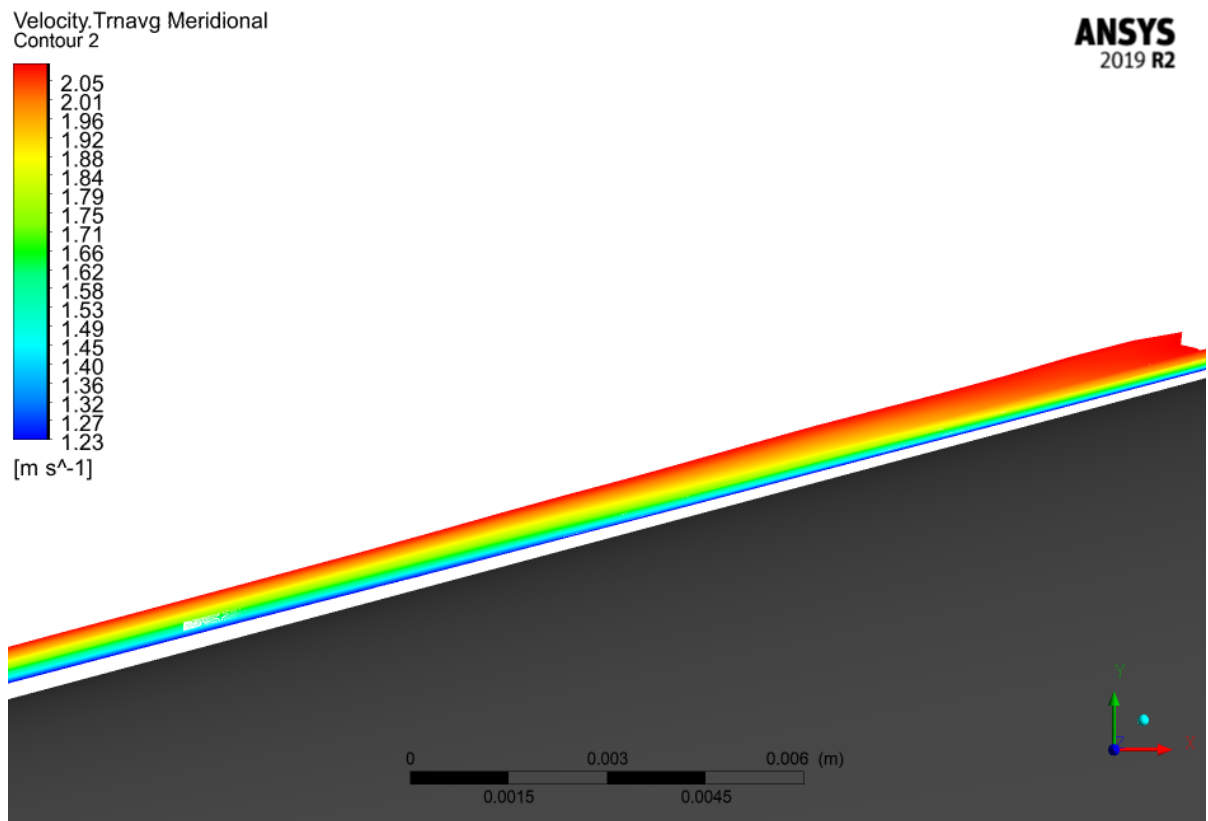
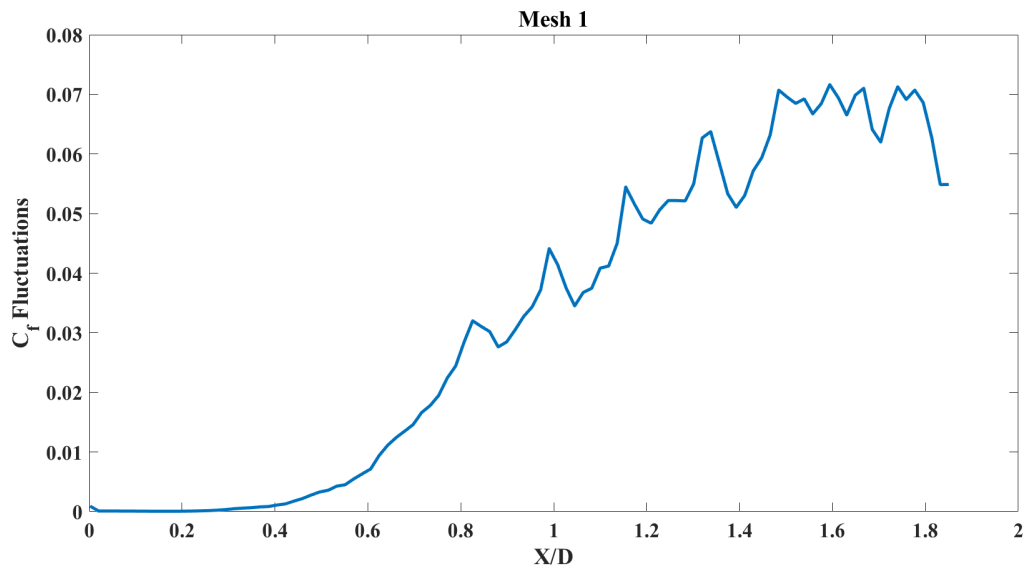
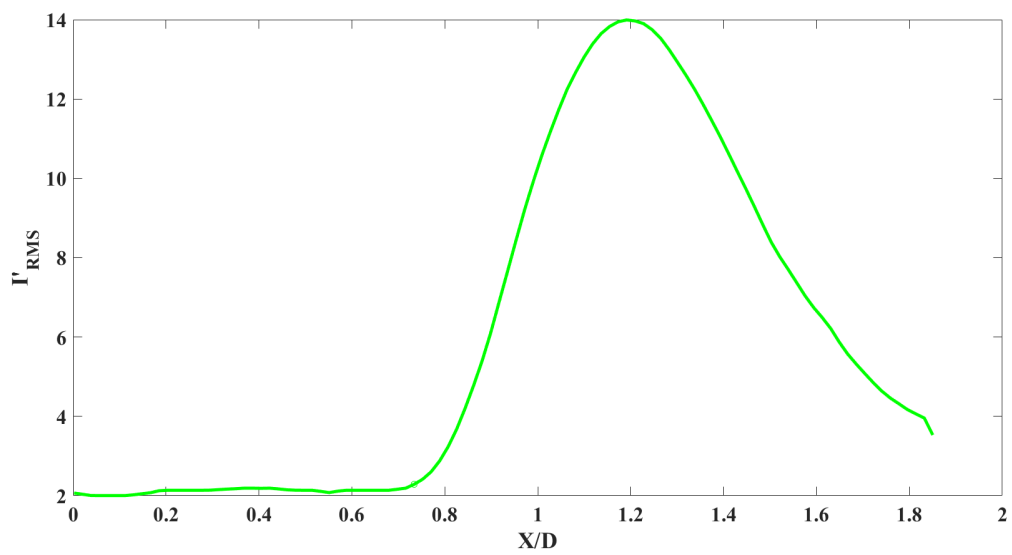


Figure 6.7: Mesh 1: Wall parallel transient average velocity contour

Figure 6.8: C_f fluctuation profileFigure 6.9: Meridional Trace of I'_{RMS} [5]

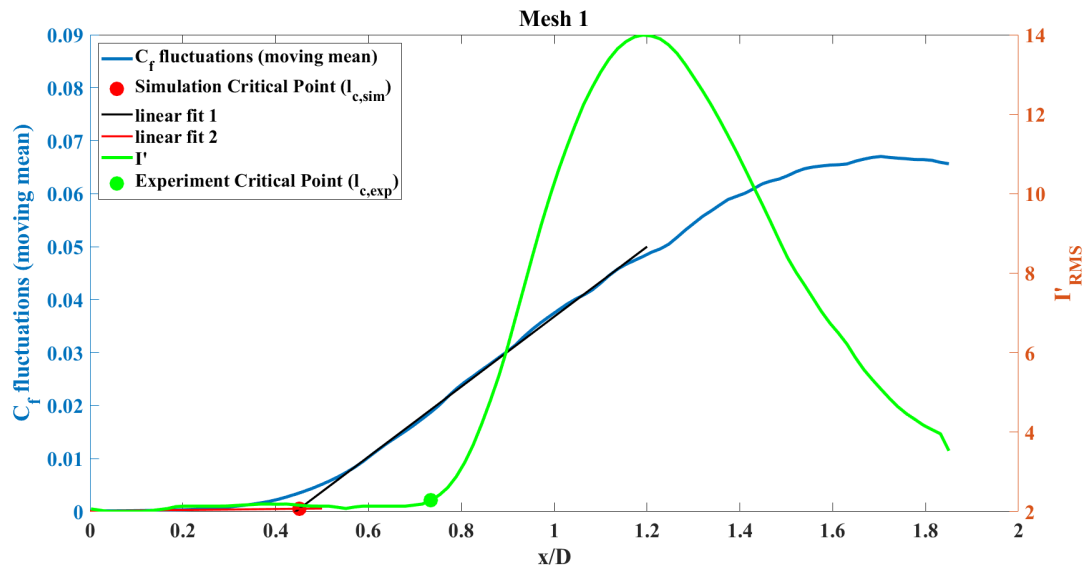


Figure 6.10: Critical point Mesh 1

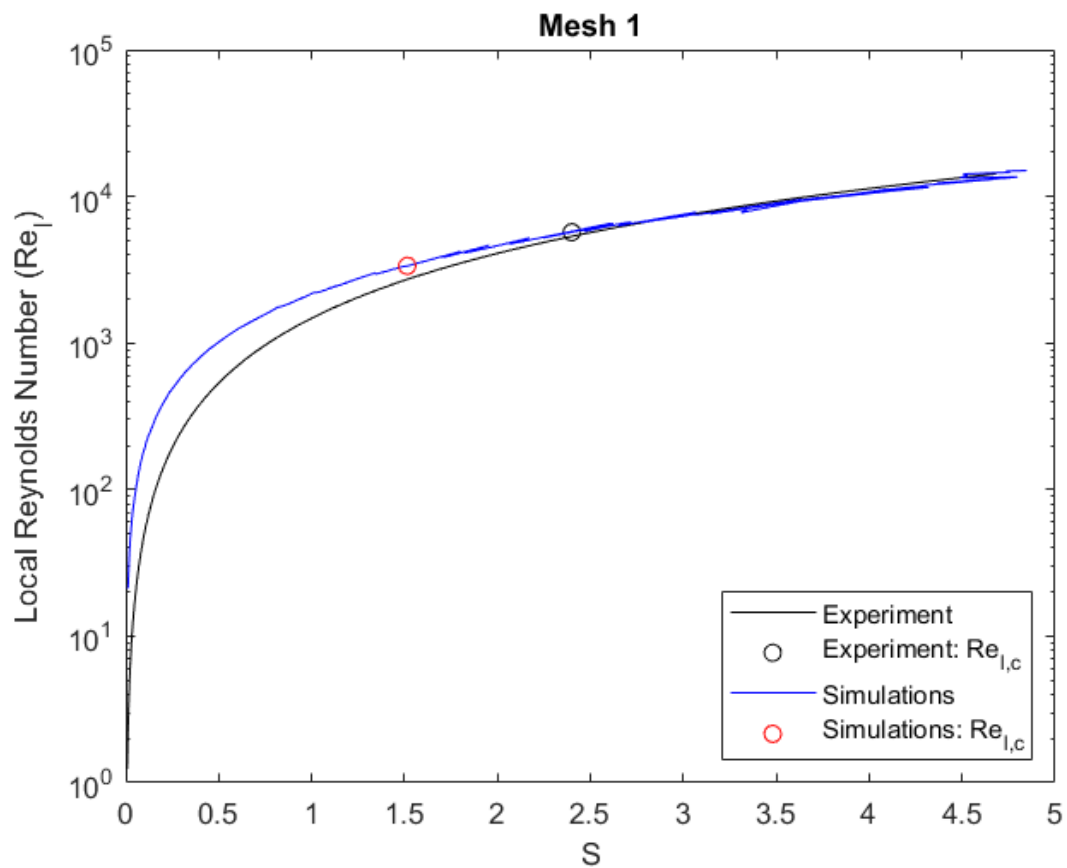
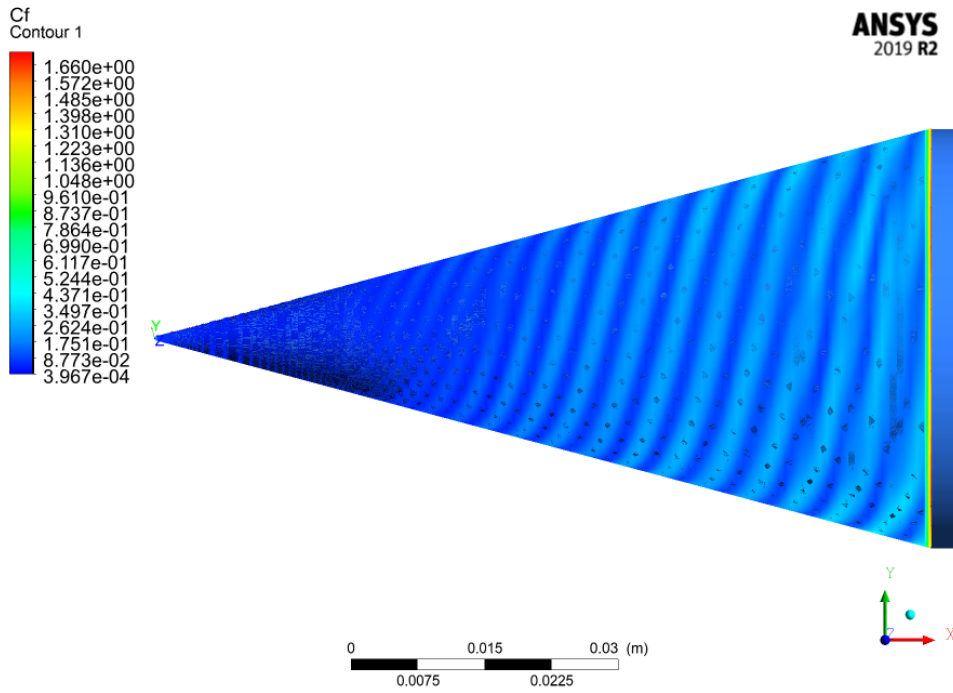
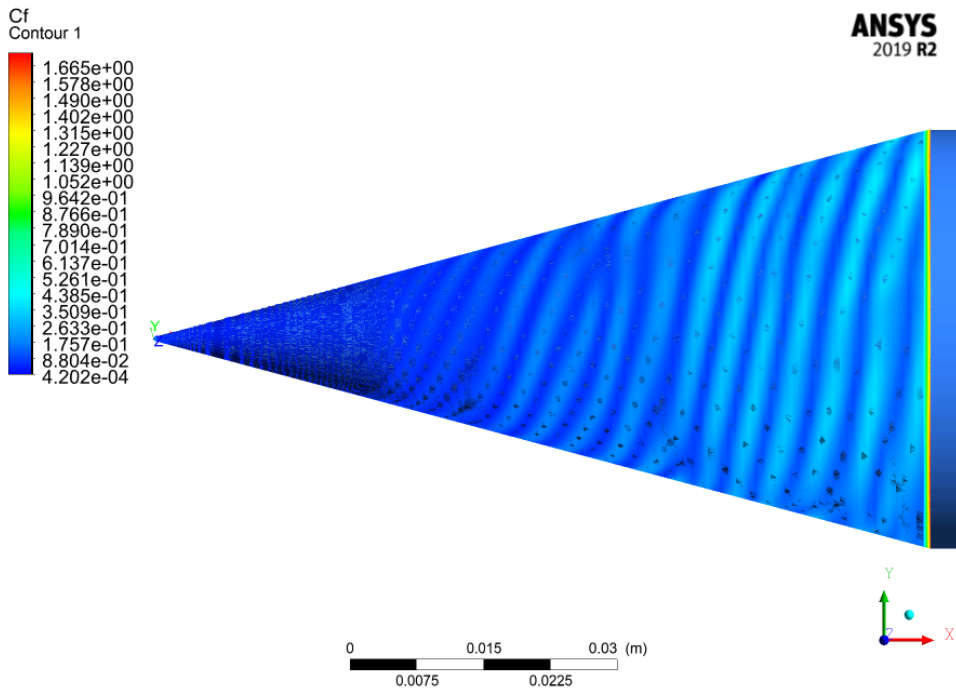


Figure 6.11: Mesh 1 - Local Reynolds Number variation with local rotation ratio

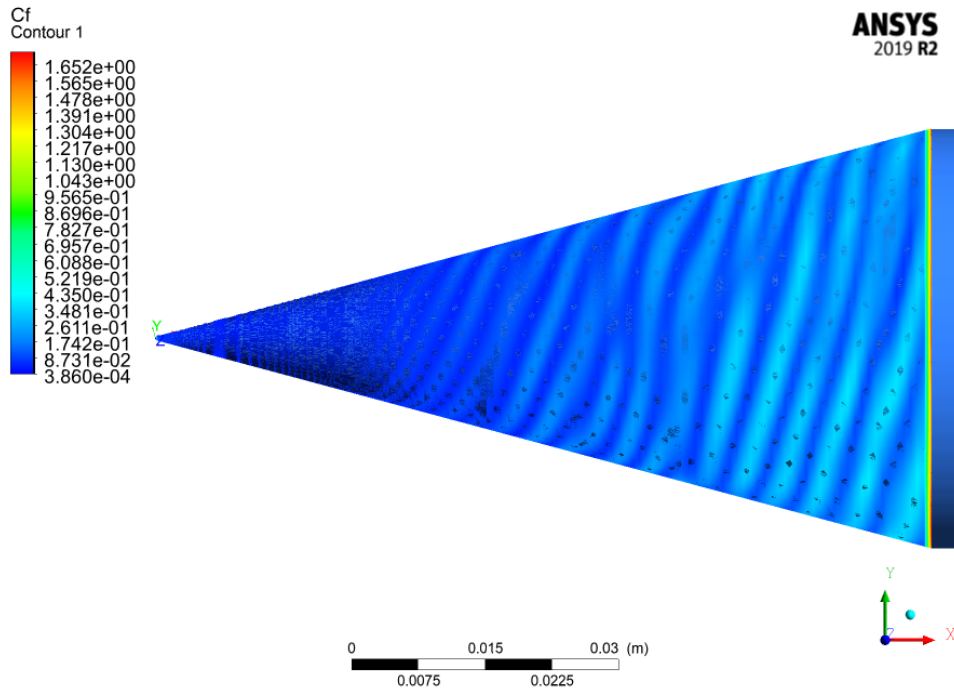


(a) Instantaneous physical time - 0.1 s

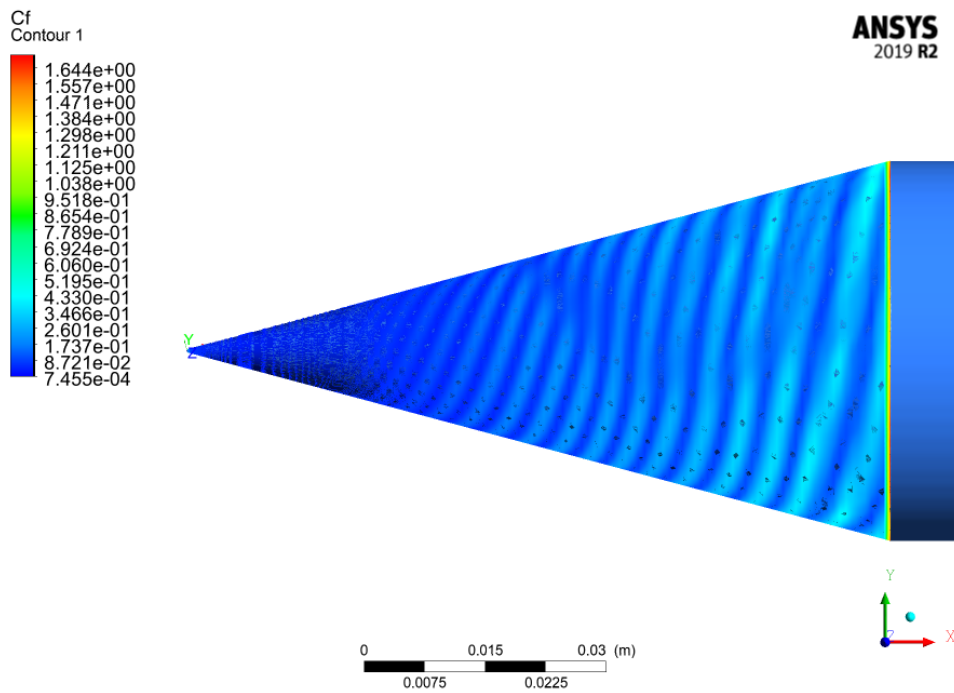


(b) Instantaneous physical time - 0.13 s

Figure 6.12: Mesh 2 - Instantaneous Wall Friction Coefficient Contours (t = 0.1 s and 0.13 s)



(a) Instantaneous physical time - 0.15 s



(b) Instantaneous physical time - 0.2 s

Figure 6.13: Mesh 2 - Instantaneous Wall Friction Coefficient Contours ($t = 0.15$ s and 0.2 s)

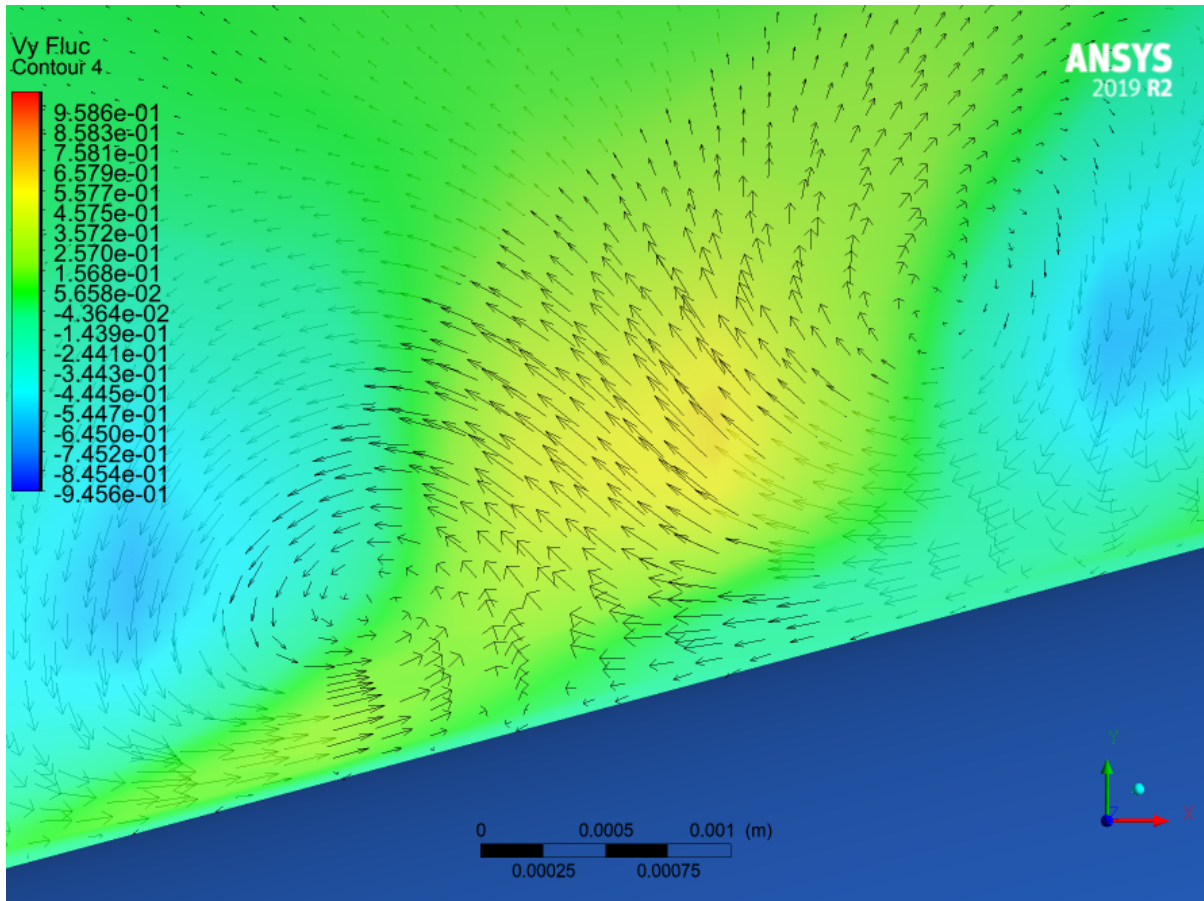


Figure 6.14: Mesh 2 - Wall normal velocity fluctuation Contour

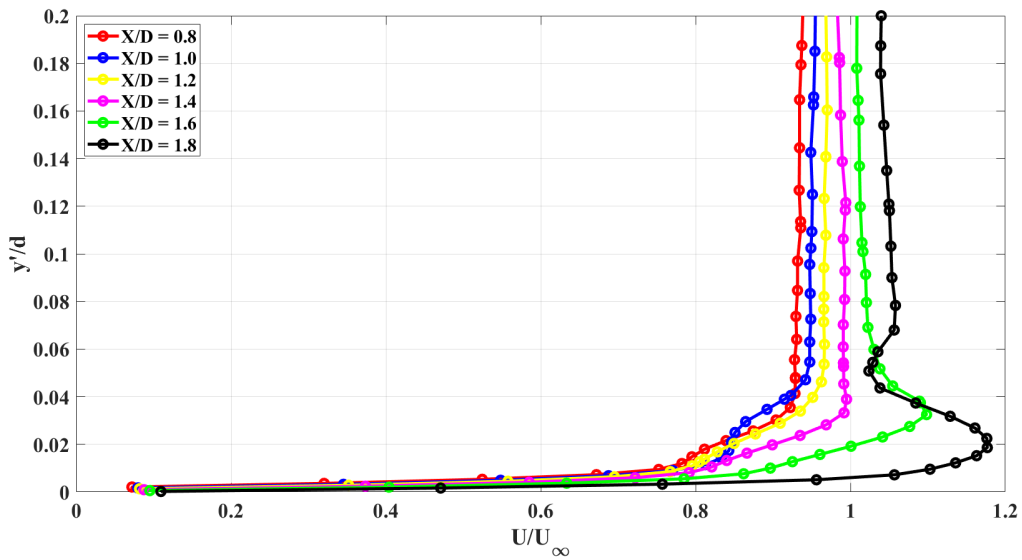


Figure 6.15: Mesh 2 - Wall Parallel Transient Mean Velocity Profile

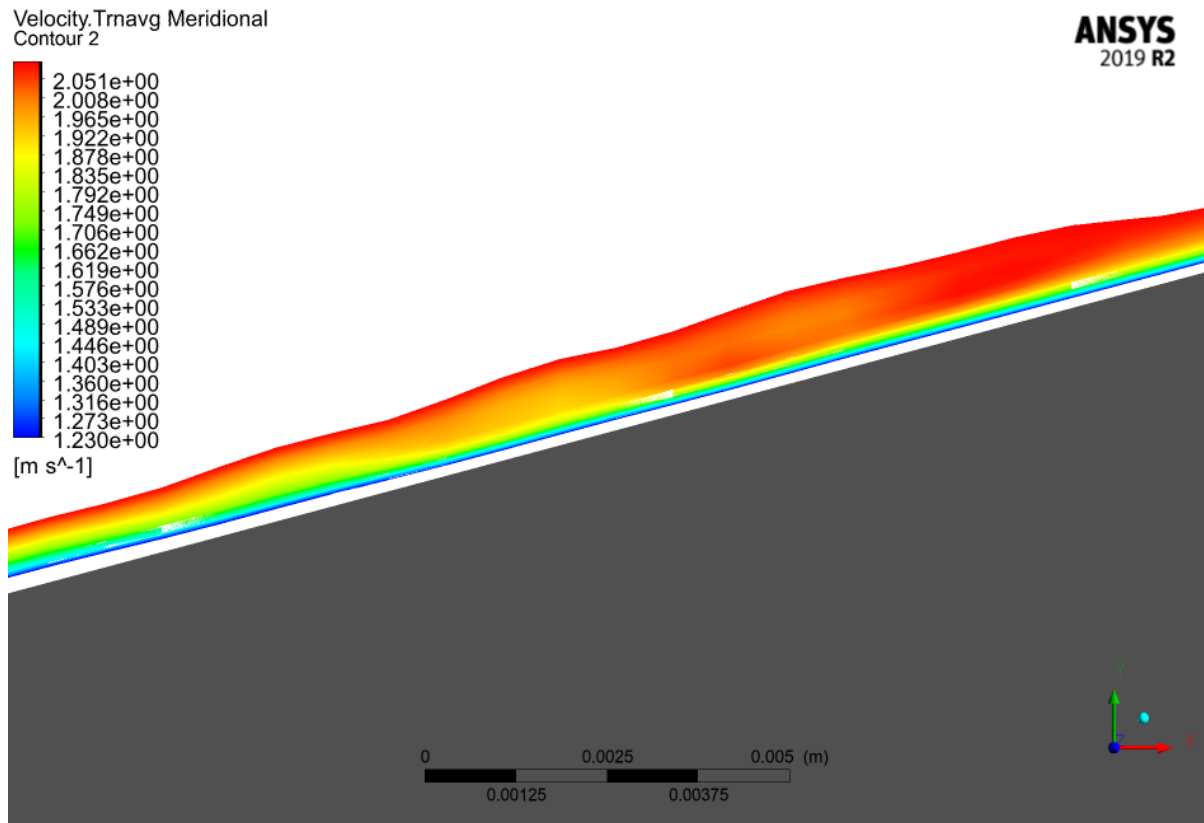


Figure 6.16: Mesh 2: Wall parallel transient average velocity contour

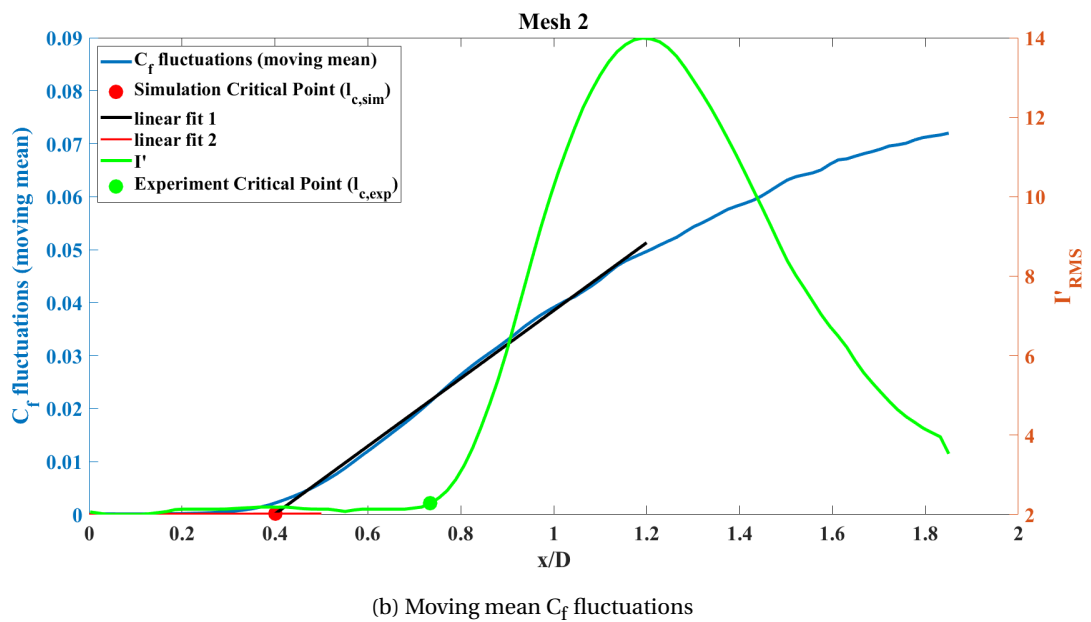
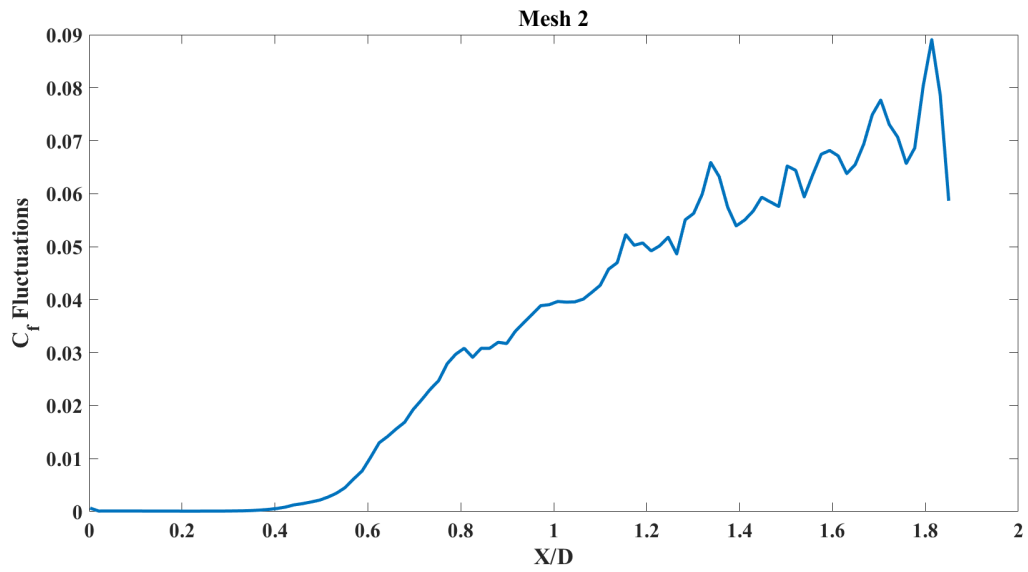


Figure 6.17: Wall normal velocity fluctuations

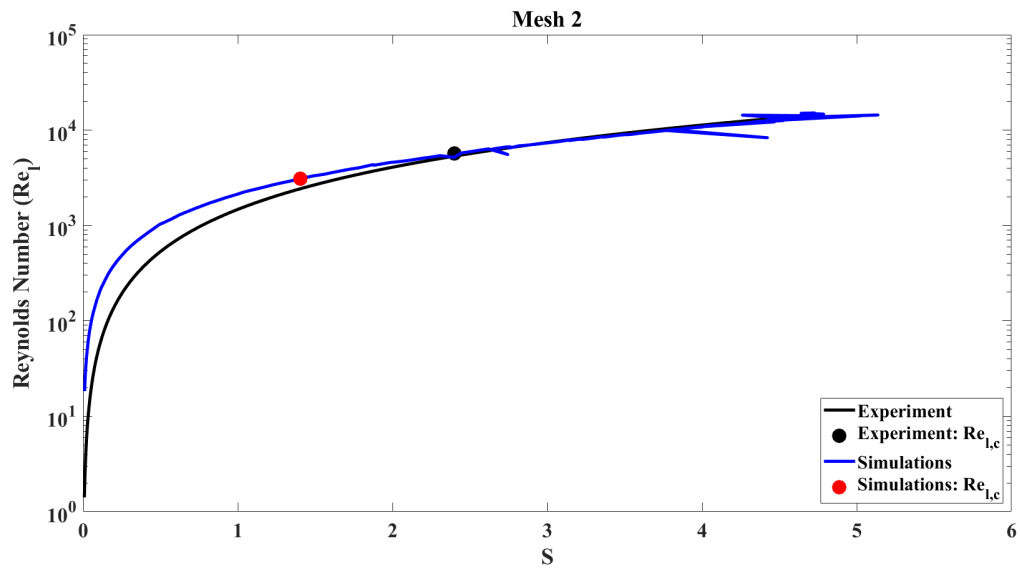


Figure 6.18: Mesh 2: Local Reynolds Number Variation with local rotation ratio (Re_l Vs S)

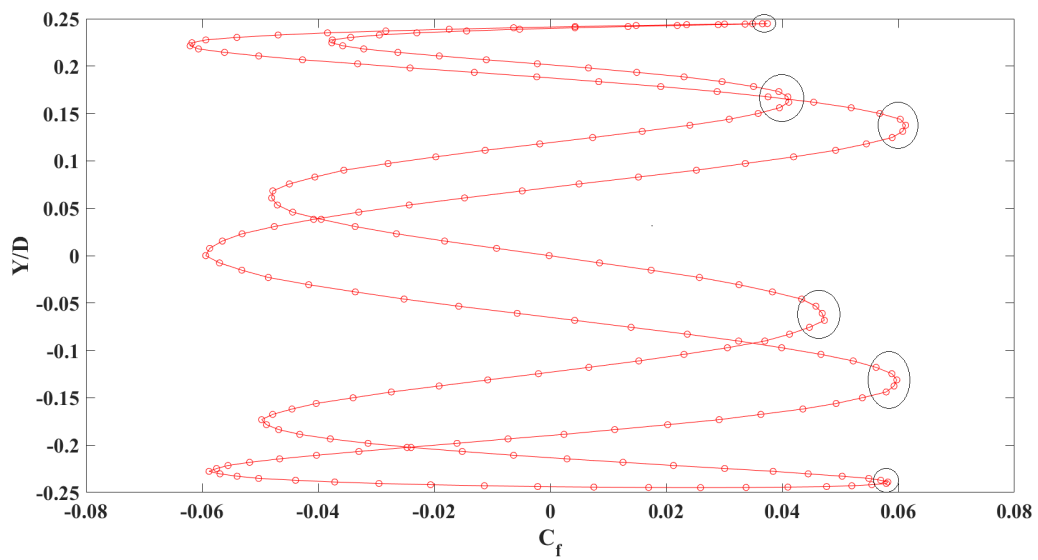
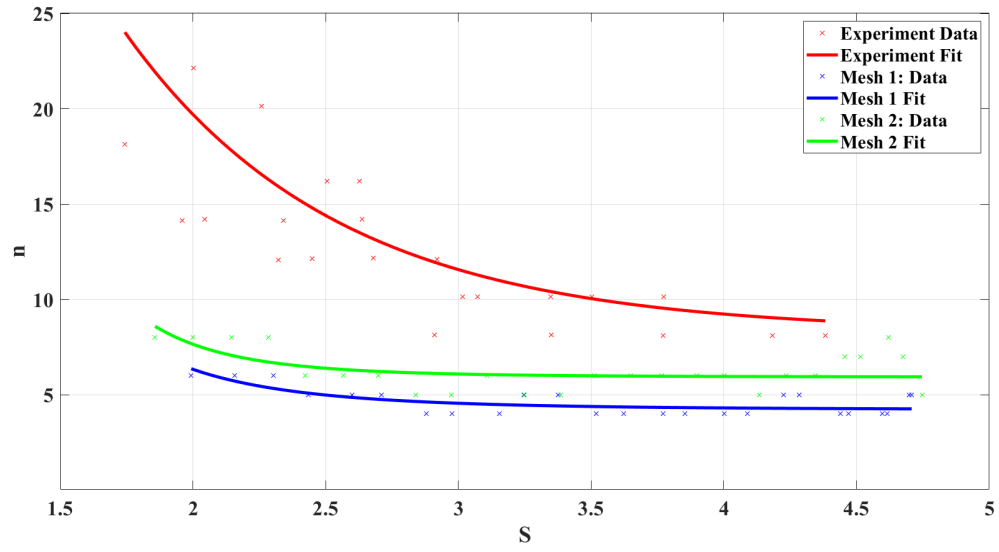


Figure 6.19: C_f variation in Y/D

Figure 6.20: n vs S

LES: Non-Axial Inflow

The previous chapters (chapter 5 and 6) deal with an axial inflow over the cone. The application area of this research is in the use of similar axis-symmetric geometries as spinners in Boundary Layer Ingestion (BLI) engines. As described in chapter 2 the distorted inflow generates an incidence angle to the flow over the cone (chapter 2 sub section 2.1.4).

For setting up the simulation run with a 2° incidence angle with respect to the X axis (global coordinate system), the velocity components were changed at the inlet for the laminar case, (the results of which were used as the initial conditions for the LES run). These changes are quantified in the following way:

$$\begin{aligned} U &= U_\infty \times \cos(2) = 2.46 \times \cos(2) = 2.458 \text{ m/s} \\ V &= 2.46 \times \sin(2) = 0.0858 \text{ m/s} \\ W &= 0 \text{ m/s} \end{aligned} \quad (7.1)$$

Here, U, V and W are the velocity components in the X, Y and Z directions respectively.

Figure 7.1, 7.2 and 7.3 represent velocity magnitude vectors (in red) over the cone, near the inlet and near the outlet respectively. These were plotted to visualise the difference of applying a 2° incidence angle on the flow direction.

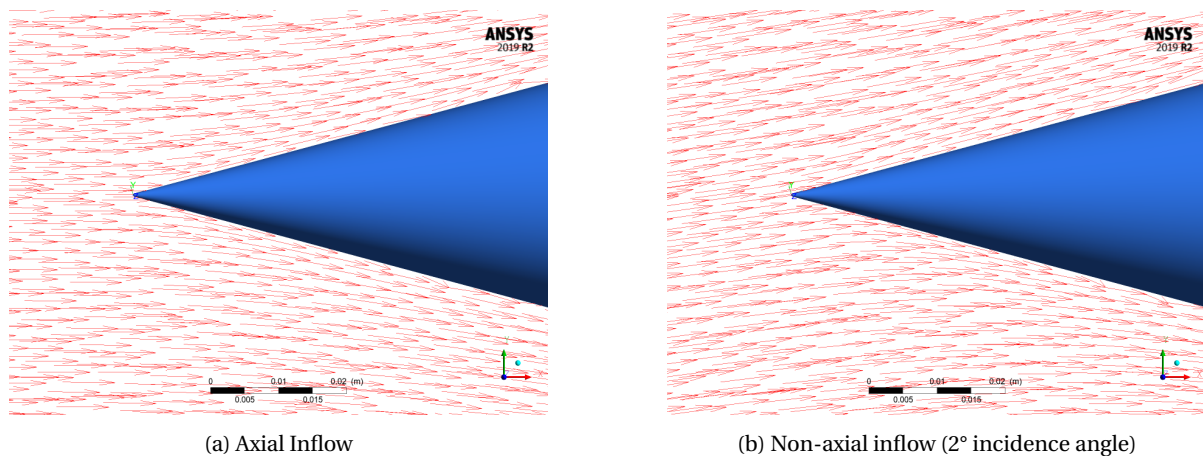


Figure 7.1: Velocity magnitude vectors (in red) showing effect of incidence of flow upstream over cone

The difference in the flow direction over the cone is clearly visualised through figure 7.1. This non incidence implies that one side of the cone will be the windward and the other the leeward side (figure 7.5 illustrates this). Tambe et al. [5] found that this asymmetry causes the formation of the observed small scale perturbations to be delayed in space (figure 2.25).

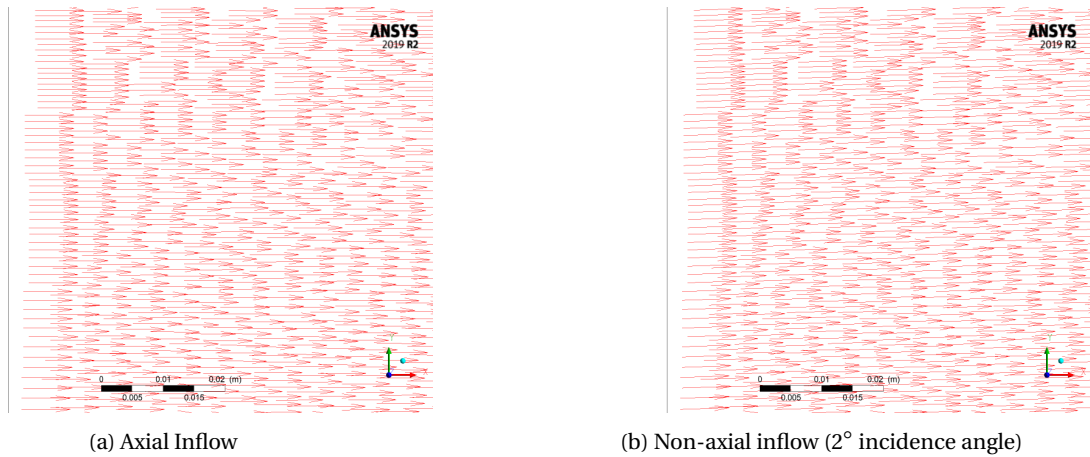


Figure 7.2: Velocity magnitude vectors (in red) showing effect of incidence of flow near the inlet

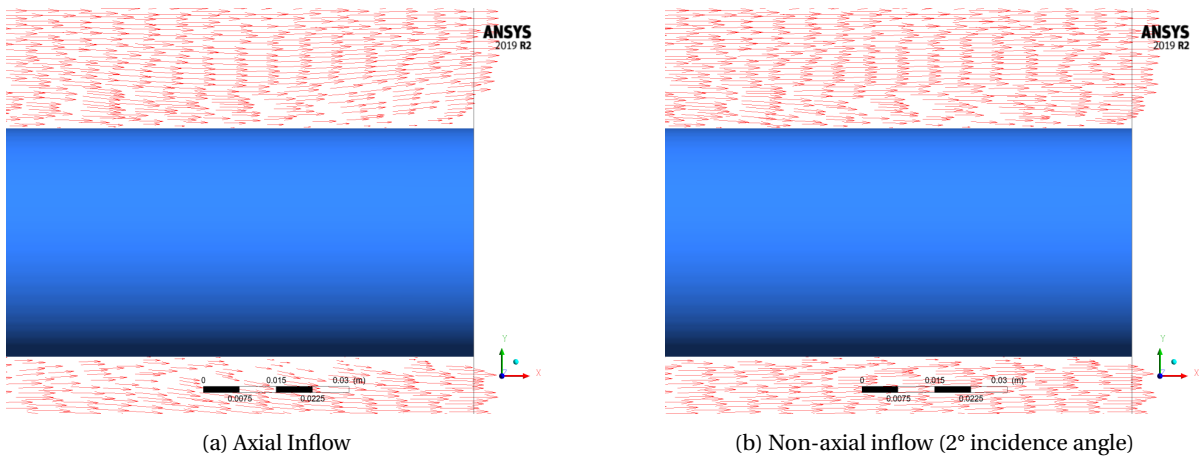


Figure 7.3: Velocity magnitude vectors (in red) showing effect of incidence of flow near the outlet

The flow direction at the inlet (figure 7.2) also shows the effect of the 2° incidence. The primary difference between the simulations and the experiment is the direction of flow at the side walls.

The experiments by Tambe et al. [5] was conducted in the open jet wind tunnel facility (W Tunnel) at the Aerospace faculty in TU Delft, The Netherlands. In the numerical simulations, the flow is bounded by the domain walls and cannot exit it. With the domain far walls having set to free slip conditions, i.e. the shear stress on the wall was set to 0. Under these conditions, the flow would follow the direction of the wall (figure 7.4b). This forms the fundamental difference in the implementation of the incidence angle between the experiments and the simulations. With the flow following the wall at the far surface, the velocity vectors would be affected near the surface and this will change the development of the flow over the cone surface.

Mesh 2 was selected for this study. The following sections will delve into the analysis of this case and compare with the experiments by Tambe et al. [5] (for this reason, the basic conditions, like rotation velocity of cone, inflow velocity and geometry of cone were kept the same as in the experiments) to validate if this was indeed successful and recommend any potential changes.

7.1. Vortex Footprint

Studies on non-axial flows over cones have only recently been conducted by Tambe et al. [5] in 2020. The experimental study used surface temperature measurements as the footprint for these vortices. Figure 2.25 shows an instantaneous image of the surface temperature footprint for a non-axial inflow (2° incidence angle). When compared to figure 2.24, it is observed that the development of the coherent vortical structures over the cone are delayed in space.

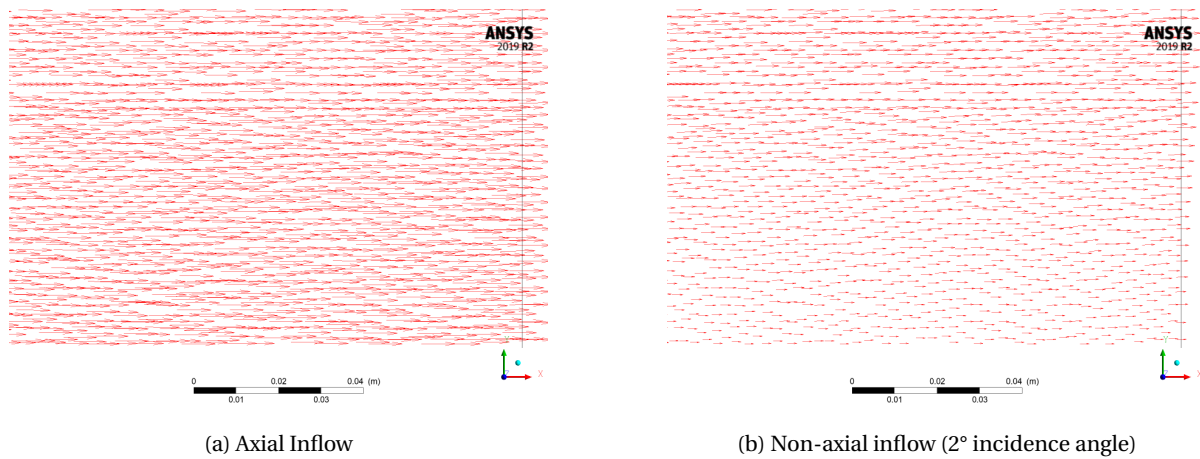


Figure 7.4: Velocity magnitude vectors (in red) showing effect of incidence of flow at the side walls

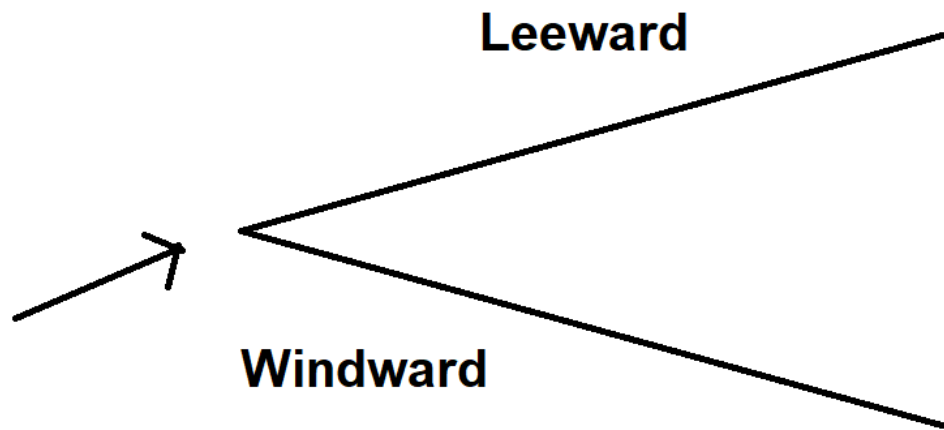


Figure 7.5: Illustration of windward and leeward side of cone

Figure 7.6 is used for visualising the footprints of these vortices, using instantaneous C_f contours.

Tambe et al. [5] in their studies, found that the asymmetry in the flow due to the incidence (causing varying stability characteristics along the circumference), suppressed the growth of these counter-rotating vortices.

The simulation was unable to capture, through instantaneous C_f contours, the delay in the formation of the coherent structures. To visualise the small counter rotating vortices due to the non-axial inflow, instantaneous wall normal velocity fluctuation contours were plotted for both the axial and non-axial cases at the same physical time step, i.e. 1.5 s (figure 7.7).

A zoomed in contour plot within locations of $X/D = 1.3 - 1.6$ and $Y/D = 0 - 0.5$ (shown in figure 7.8) was also made to visualise the difference in the shape of these counter rotating vortices and compare it with those obtained in the axial case.

Figure 7.6 failed to show the spatial delay in the development of the coherent vortical structures over the cone, to check if this delay is captured through the simulations, a meridional profile of the C_f fluctuations was made and defining the same criterion used in chapter 6 the critical point was calculated for this case. Figure 7.9 shows the profile obtained using the limited number of available timesteps.

The critical point calculated for the non-axial case (using the above criterion) was at $X/D = 0.47$. Before comparing it with that obtained using Mesh 2 for the axial case, it is important to note that the axial case simulation

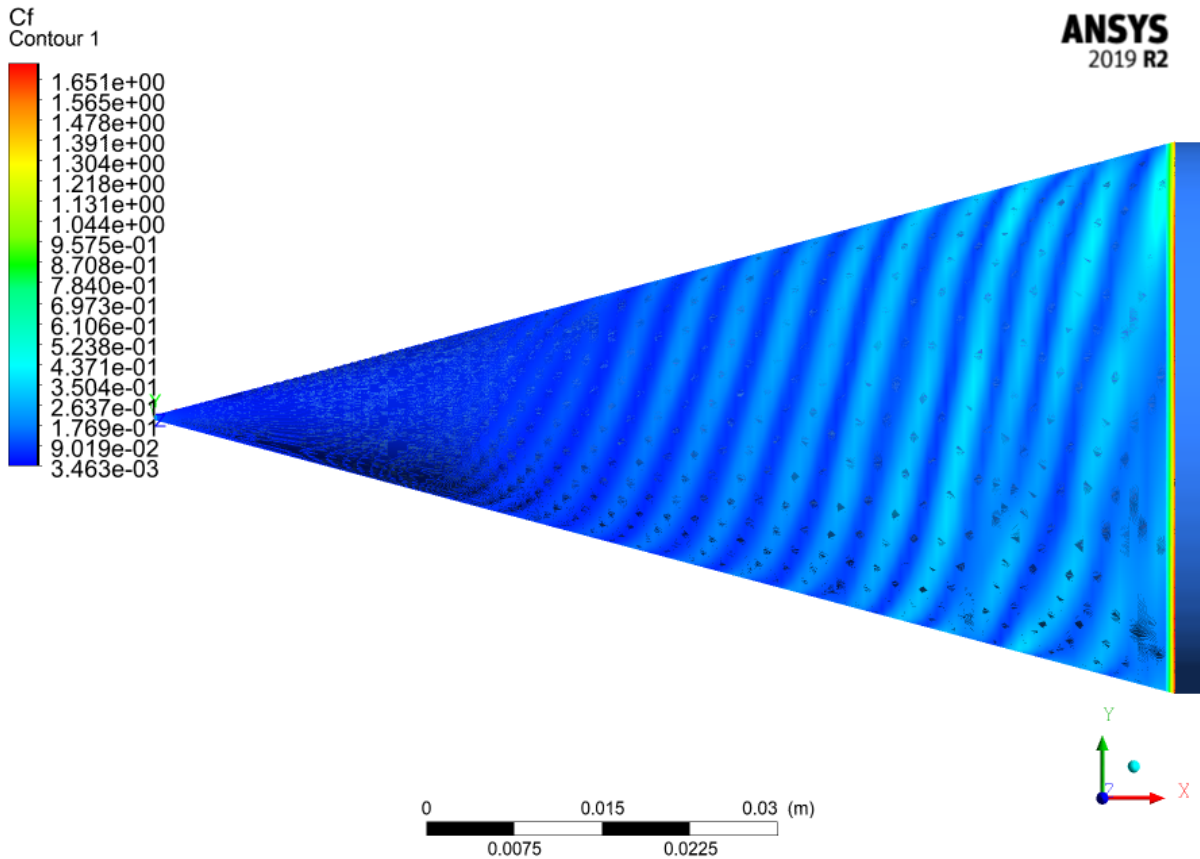


Figure 7.6: Instantaneous C_f contours (physical timestep = 0.15s)

ran for a physical time of 0.2 s, while the non-axial case for 0.15 s (constraints involved extremely small time steps and limitations in job wall time on cluster). This would thus not be a fair comparison at the onset. To overcome this, the time steps between 0.1 s and 0.15 s for the axial case was taken and using the same criterion, the critical point was calculated to be at $X/D = 0.4413$. Figure 7.10 shows both critical point locations.

With all the other parameters in the setup of the simulation being constant (other than the introduced incidence flow angle), it can be concluded that the spatial delay due to the non-axial inflow was qualitatively captured by the simulations. It should be noted here that the simulations (for non-axial case in particular and axial case in general) should be made to run for further time steps (the evidence for this is provided in the following section).

7.2. Reynolds Number

As mentioned earlier, the experiments by Tambe et al.[5] found that the asymmetry in the flow due to the incidence angle spatially delayed the formation of the vortices. This asymmetry thus induces changing flow conditions across the azimuth of the cone.

Figure 7.11 and 7.12 characterises the simulated flow asymmetry. The local rotation ratio and local Reynolds number, which are a function of the edge velocity is used to characterise this asymmetry. The edge velocity¹ will vary in the windward and leeward side and this is visible in the two figures.

The experiments by Tambe et al. [5] found that the edge velocity for the windward case is reduced and increased for the leeward side. Through figures 7.11 and 7.12 the simulations show a qualitative agreement with this. A closer match with the experiments by Tambe et al. [5] was found for the leeward side than for the windward meridian.

¹The definition of edge velocity kept the same as for the previous case

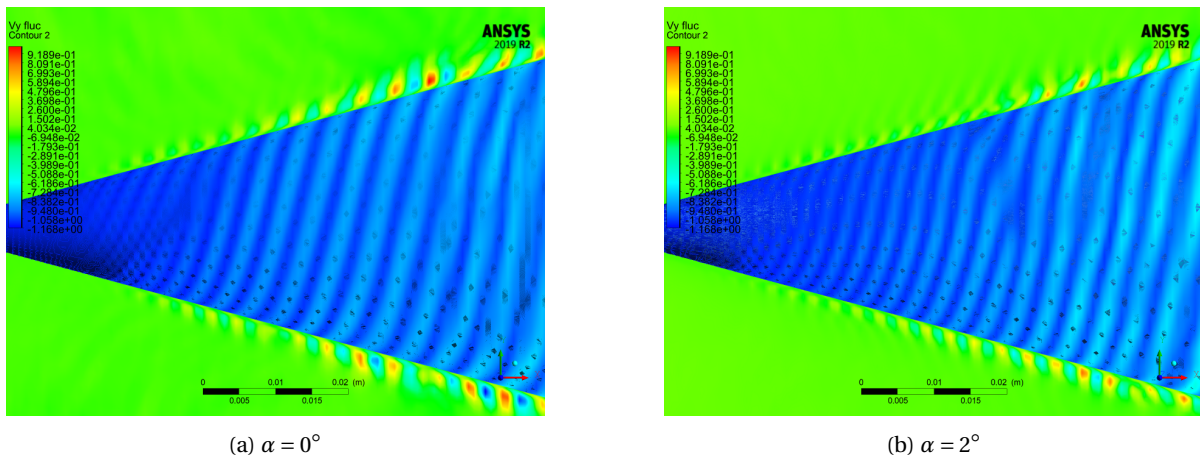


Figure 7.7: Wall normal velocity fluctuations

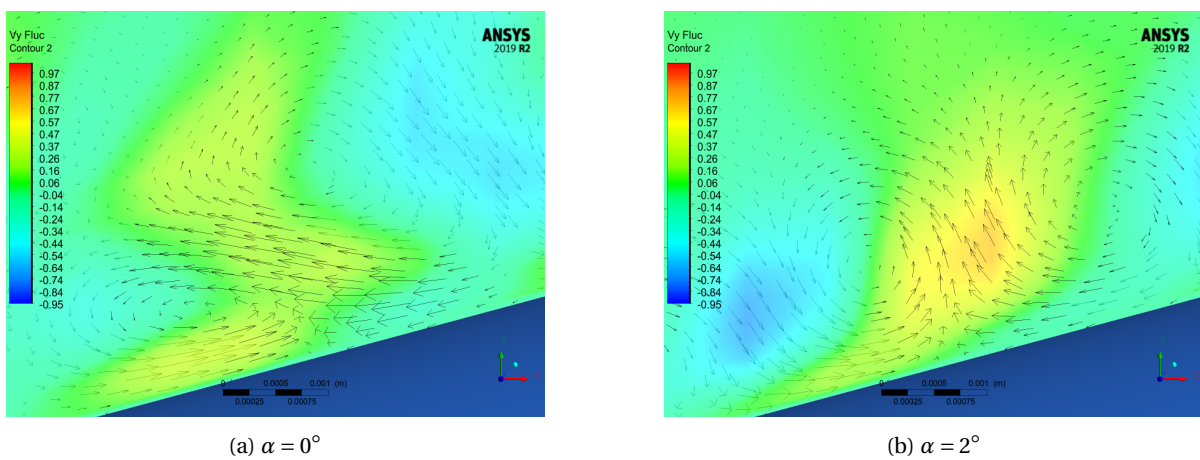


Figure 7.8: Counter rotating vortices for axial and non-axial case at instantaneous physical time of 0.15s

There are multiple outliers in the initial values of S (for both windward and leeward side) and may be explained by the simulation not having run for enough timesteps. With a non-axial inflow having an additional velocity component in the vertical direction (Y direction), the v component of the velocity is deemed as the determining factor. Figure 7.13 shows the running average² variation of the v velocity component at the two probe locations. As is seen, this is a still developing flow and needs further iterations before the data exported can be studied in further detail.

7.3. Wall Parallel Velocity Profile

The previous sections showed the simulated asymmetry between the windward and leeward side of the cone under the non-axial incident flow.

Figure 7.14 shows the wall parallel transient averaged (over a total physical time of 0.15 s) velocity profile obtained at the leeward meridian (the locations are the same as taken in the previous case, represented through figure 6.5) and figure 7.15 shows the locations ($X/D = 0.8, 1.0, 1.2, 1.4, 1.6$ and 1.8) over the windward meridian of the cone. The corresponding profiles are shown in figure 7.16.

For ease of comparison, the windward side plot was mirrored. The velocity profiles further indicate the asymmetry between the windward and leeward meridian.

To further visualise the asymmetry between the two meridians, transient mean wall parallel velocity contours are made for both the leeward (figure 7.17) and windward meridians (figure 7.18).

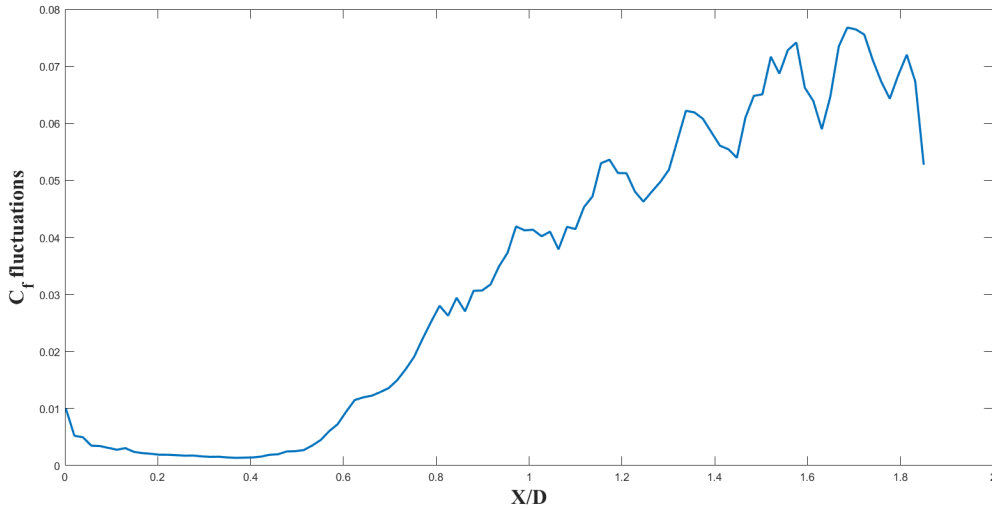


Figure 7.9: Fluctuating C_f v/s X/D for non axial inflow

The velocity profiles, figures 7.16, 7.14, 6.6 and 6.15, indicate that the momentum mixing process for both the windward and leeward sides is gradual in comparison to the axial flow case. The simulations also show that the momentum mixing is much more gradual in the leeward side as compared to the windward edge. Both observations qualitatively agree with the experiments.

7.4. Spatial distribution of Vortices

The next objective was to study the spatial distribution of the vortices. Figure 7.19 shows the trend of the number of counter rotating pairs of vortices against the local rotation ratio. The trend for the axial cases through both the simulation and experiments is added to the plot for ease in comparison.

As with the previous axial case, the number of pairs of counter rotating vortices were calculated using the same methodology, and thus the predicted number is dependant on the azimuthal distribution of mesh nodes.

The formation of the vortices being delayed, i.e. they were detected at higher rotation ratios compared to the axial case, which is in agreement with the experiments by Tambe et al [5]. They also found that the trend in the observed number of vortex pairs remained the same for both the axial and non-axial cases (the similarity in trend through the simulations is seen in figure 7.19). As with the axial flow case, the trend, however, is not similar when comparing the simulations with the experiments. The non-axial case showed no change after a local rotation ratio of 3.5. The reason for this is not clear at this moment and further investigation is needed.

The equations defining the best fit are the following:

- Experiment ([5]): $n = 138.96\exp(-1.25S) + 8.3$
- Simulations (Axial case): $n = (103.1S)^{-5.906} + 5.937$
- Simulations (Non axial case): $n = (1.28 \times 10^5 S)^{-12.98} + 5.278$

To quantify the number of vortex pairs simulated for the non-axial case, the same three locations as with the previous case were taken and table 7.1 shows the predicted number of vortex pairs.

7.5. Conclusions

The WALE model of LES was chosen to study the effects of a non-axial inflow over the cone (half angle 15°) rotating at 5000 RPM. Only Mesh 2 (finer mesh) was used for this case.

²Average taken using cumulative sum

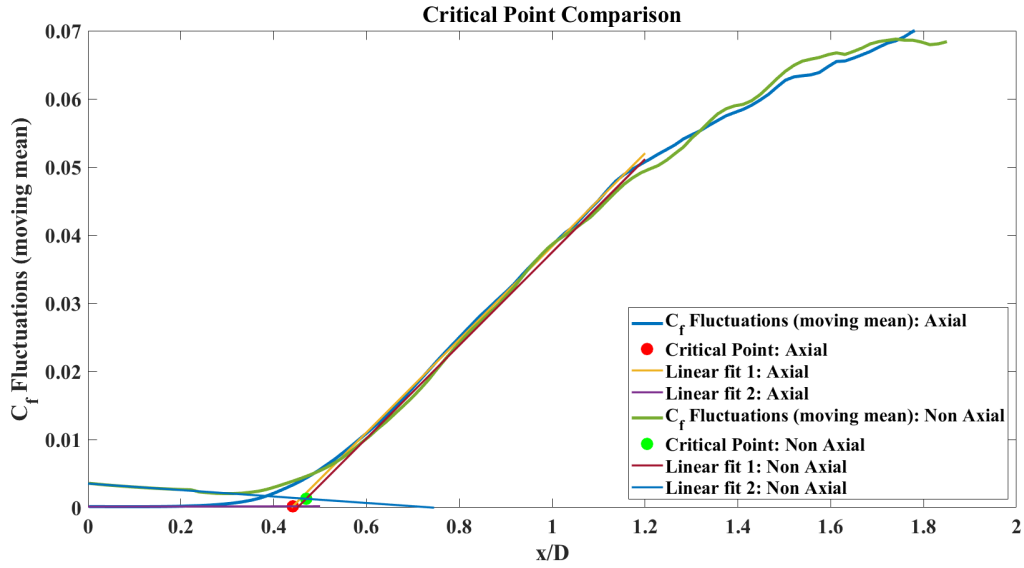


Figure 7.10: Fluctuating C_f (moving mean) profile v/s X/D for both axial and non axial inflow

Mesh 2			
Axial Location (X/D)	Azimuthal Spacing (m)	First Cell Height (m)	n
0.7	0.00066	6.94E-05	6
1.25	0.00066	6.94E-05	5
1.7	0.00066	6.94E-05	7

Table 7.1: Non-Axial case - Spatial distribution of n ($\alpha = 2^\circ$)

A 2° incidence angle (α) was given to the system. To make this change in the simulation setup, the velocity components were changed. The horizontal velocity component was set to $U_\infty \times \cos(\alpha)$ and the vertical component was set to $U_\infty \times \sin(\alpha)$. All other settings in the simulation setup was kept the same from Mesh 2 in chapter 6.

The instantaneous C_f contours failed to show the experimentally observed spatial delay in the formation of the vortex structures. To check if the setup captured the delay, the C_f fluctuations over the cone surface was obtained using the same method explained in chapter 6.

The obtained critical point with the axial and non-axial cases were compared after the same physical time interval (0.15 s), The non-axial case showed a slight spatial delay ($X/D = 0.47$) compared to the axial case ($X/D = 0.44$). With all other parameters in the setup having kept constant, other than the incidence angle given to the flow, it was concluded that the non-axial flow does indeed delay the formation of vortices in space. It should be noted that this simulation is still in its development stage and the vertical velocity component plays an important role in this. Through running averages of monitor plots, this component was seen to not have stabilised, and thus the simulation needs to run for a longer time span.

Experiments by Tambe et al. [5] found that the non-axial flow induced asymmetry in the flow over the cone. To characterise this asymmetry, local Reynolds number and local rotation ratio were used. Both quantities dependant on the edge velocity³. The edge velocity was simulated to be lower in the windward meridian compared to the leeward meridian. This qualitatively agreed with those obtained in the experiments. The variation of the local Reynolds number in the windward region did not seem to quantitatively match with the experiments and this might be because the simulations have not yet run for enough timesteps. A non-axial inflow would have a normal component of the velocity (v component) and the running average of this was taken over the entire range of timesteps at two probe locations. This showed that the v component of velocity is currently varying in time thus giving credence to the previous statement. Asymmetry was also shown using the wall parallel transient mean velocity profiles on both the leeward and windward meridian.

³Definition kept the same as the axial case

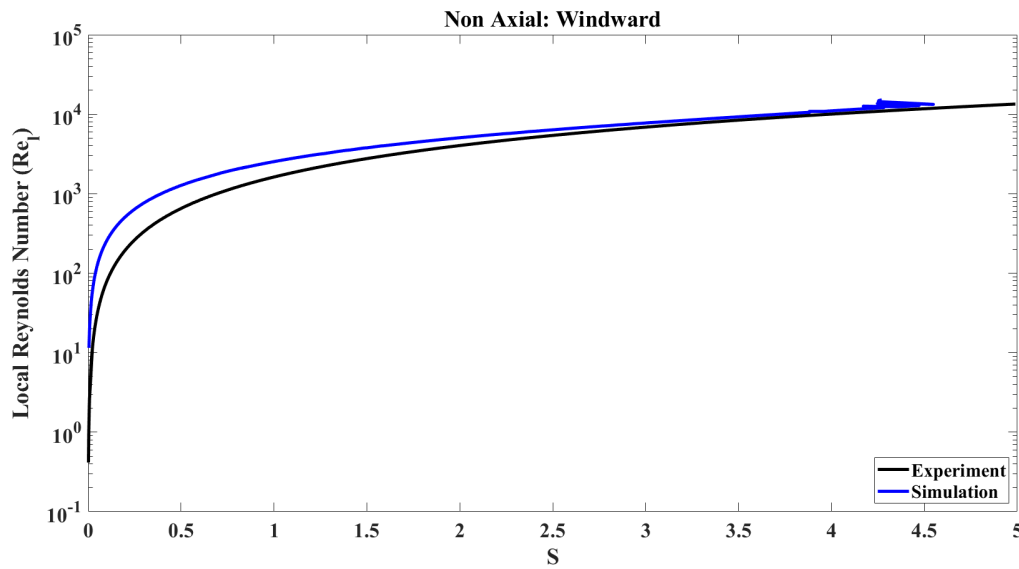
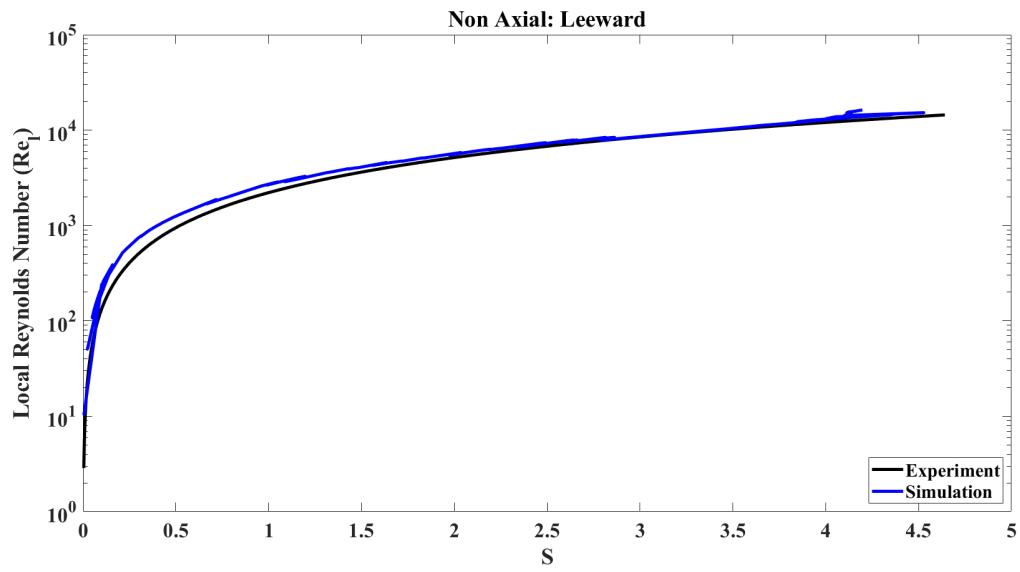
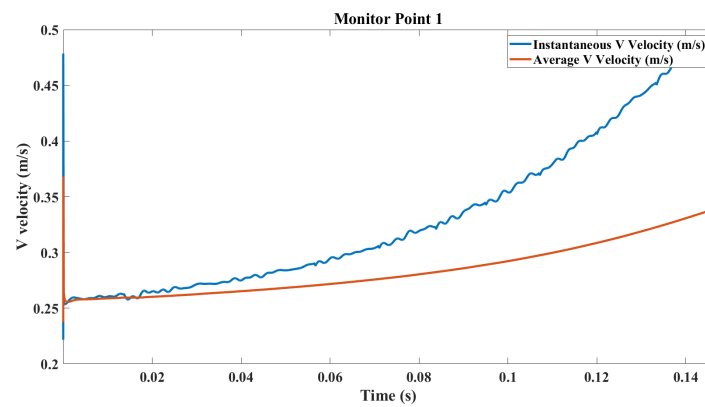


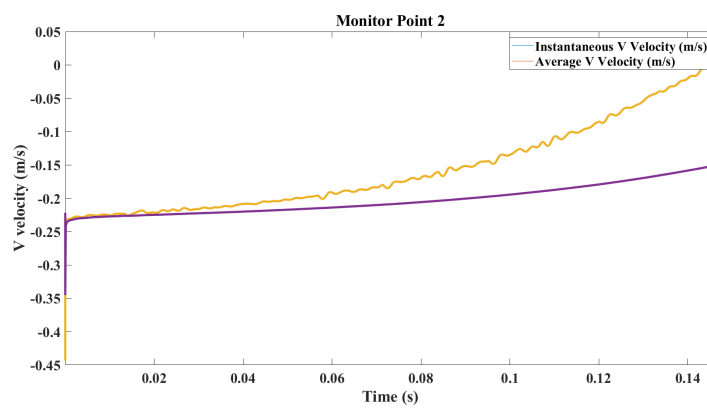
Figure 7.11: Non Axial - Re_l vs S (Windward Meridian)

The momentum mixing was visualised using both the transient mean wall parallel velocity profiles and the respective contours on both the windward and leeward side. The momentum mixing process was seen to be gradual in both the leeward and windward side when compared to the axial case. Further, the mixing process was gradual at the leeward side in comparison to the windward edge. Both the observations, qualitatively agreeing with the experiments by Tambe et al. [5].

Using the same method as the previous chapter to calculate the number of vortex pairs, the predicted delay in the start of the formation of the vortices with local rotation ratio was in agreement with the experiments. The lower number of vortices is attributed to the high spatial distance between mesh nodes in the azimuthal direction. The general trend however did not agree with the experiments by Tambe et al. [5]. The reason for this is currently unknown and needs further investigation.

Figure 7.12: Non Axial - Re_l vs S (Windward Meridian)

(a) Probe 1



(b) Probe 2

Figure 7.13: V velocity variation in time at 2 probe locations

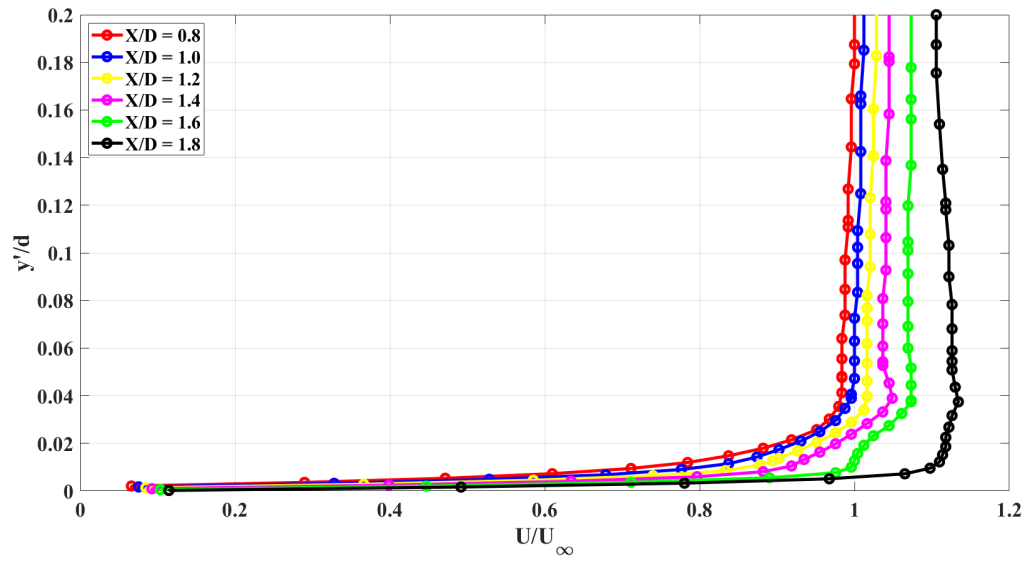


Figure 7.14: Leeward meridian: Wall parallel velocity profile ($\alpha = 2^\circ$)

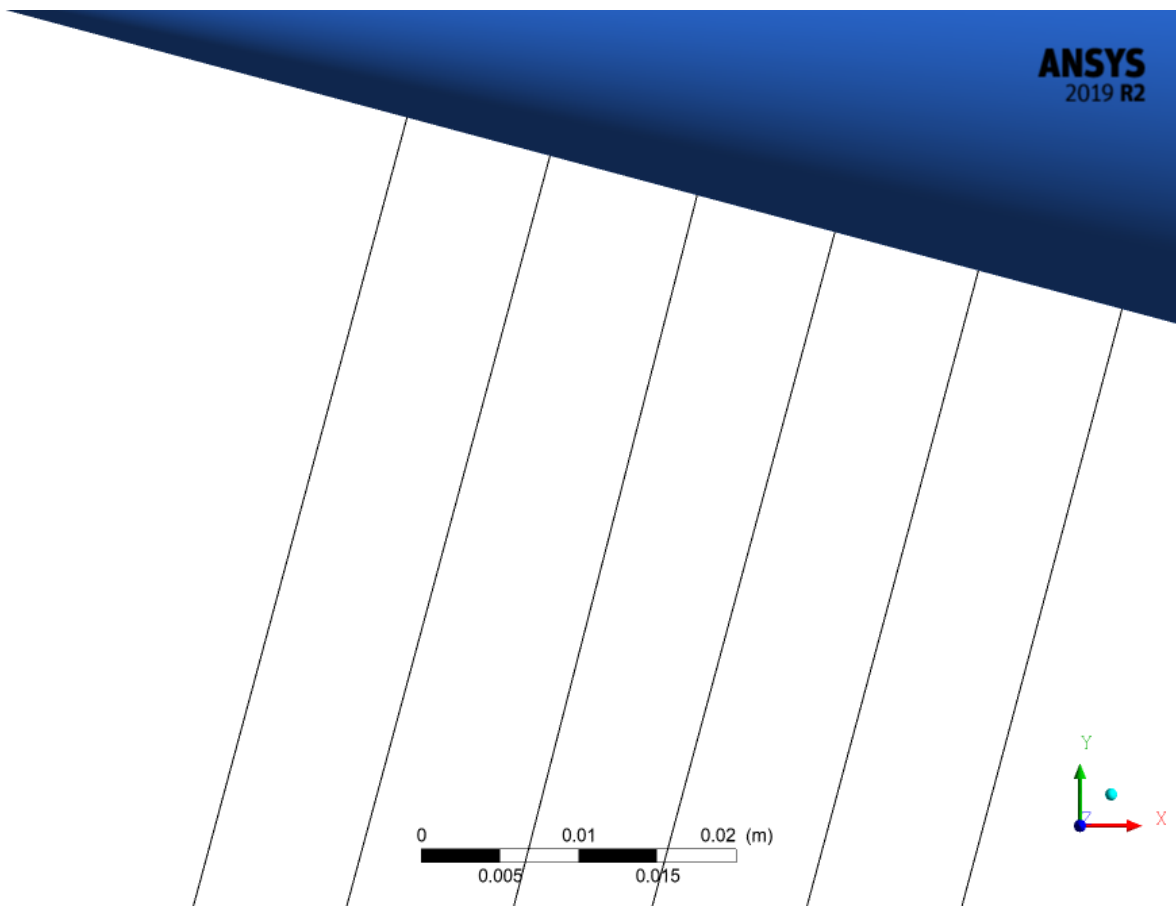


Figure 7.15: Windward meridian locations for velocity profile

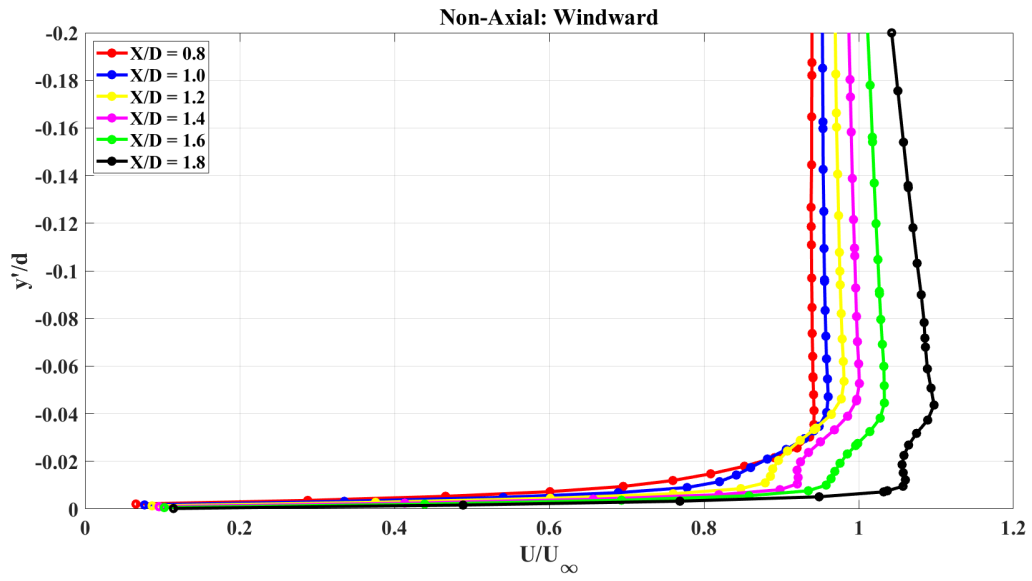


Figure 7.16: Windward meridian: Wall parallel velocity profile ($\alpha = 2^\circ$)

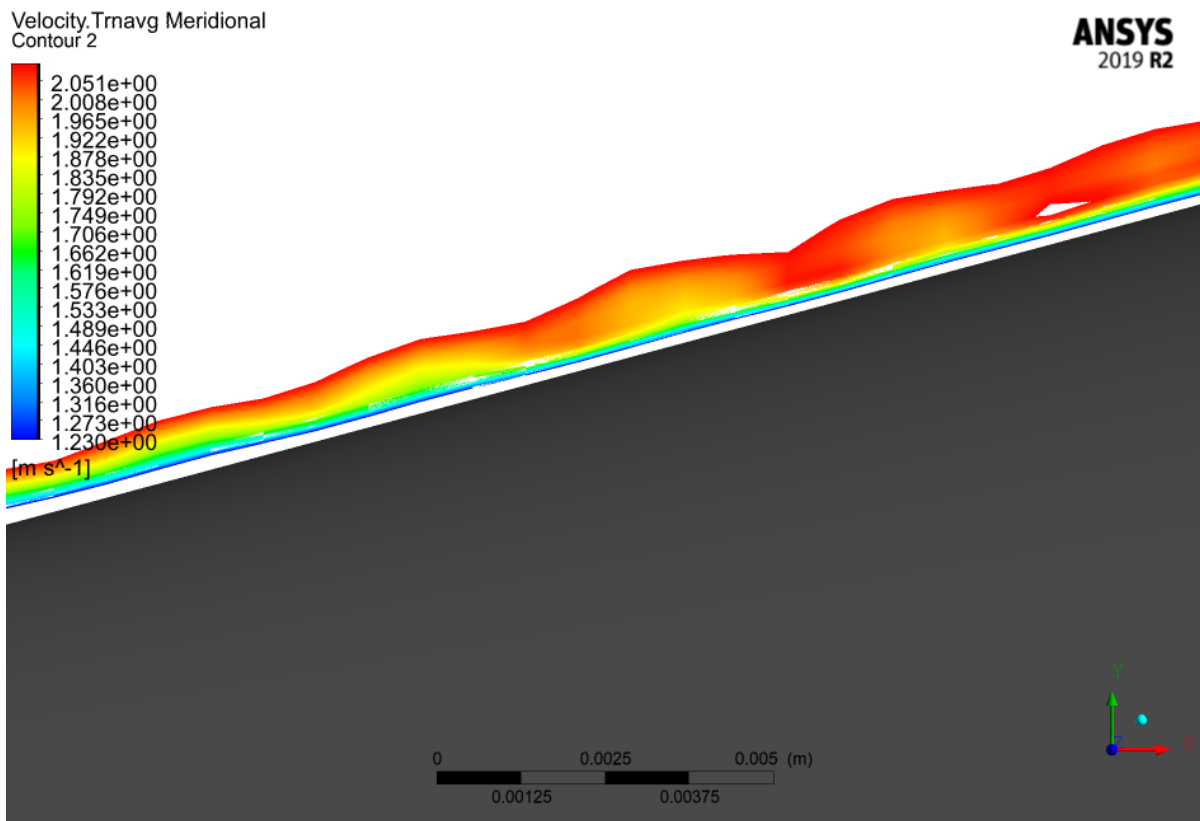


Figure 7.17: Leeward transient velocity contour

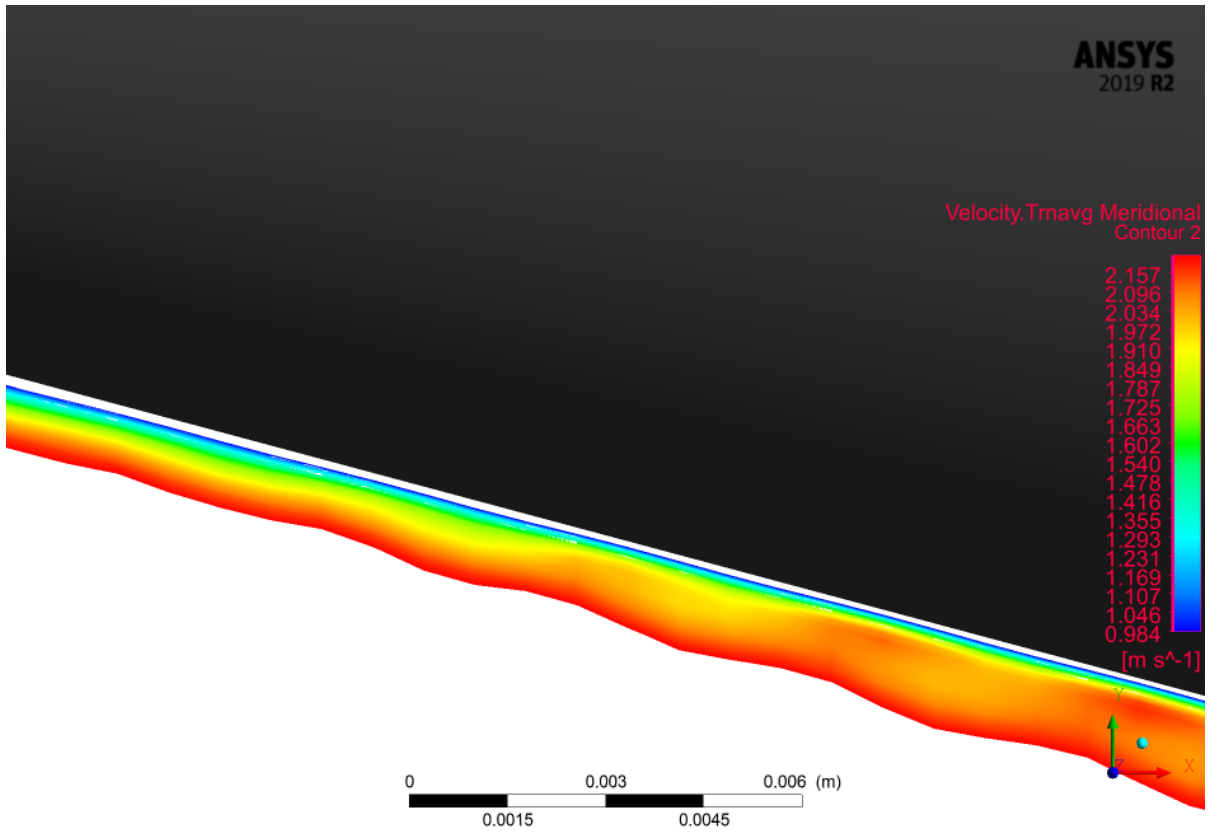


Figure 7.18: Windward transient velocity contour

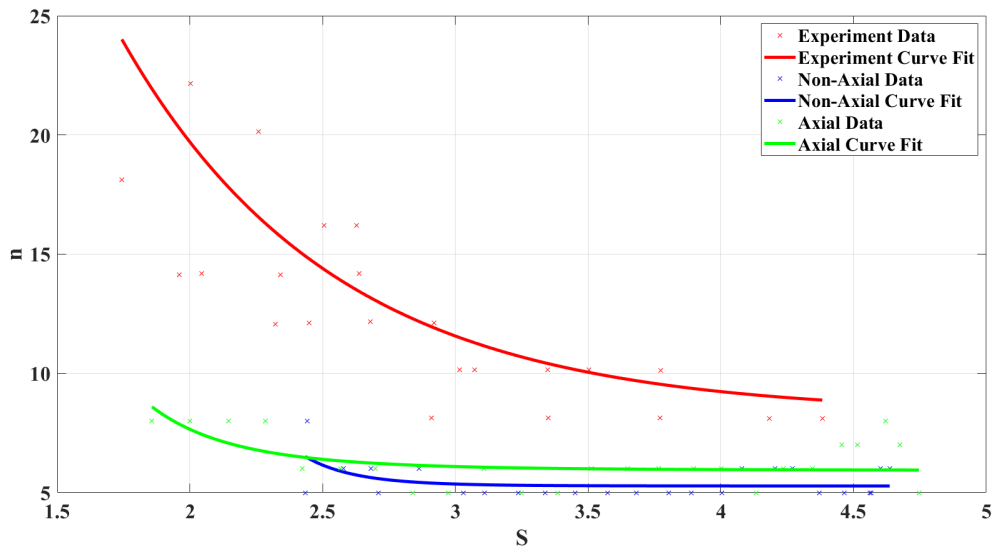
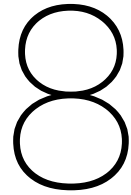


Figure 7.19: N vs S



Conclusions and Recommendations

The objective of this master thesis was to numerically simulate the counter rotating vortices observed over a rotating cone.

A cone of 15° half angle was rotated at 5000 RPM and was given an axial inflow ($U_\infty = 2.46$ m/s) as one of the cases and a non-axial inflow (2° incidence angle) as the other case.

The Baseline Explicit Algebraic Reynolds Stress Model (BSL EARSM) model was chosen to attempt the simulation using URANS and the Wall Adapting Local Eddy Viscosity (WALE) model was chosen for the LES study. ANSYS CFX was chosen as the solver. The geometry was created and meshed using the ANSYS Packages namely, DesignModeler, and ICEM CFD.

This chapter will summarise the conclusions derived from the different cases studied. The various limitations during the course of this study will also be mentioned and finally, recommendations for a mesh study and future work will be given.

8.1. Conclusions

- Using the setup explained in chapter 5, the BSL Explicit Algebraic Reynolds Stress Model was unable to simulate the counter rotating vortices. The main cause attributed to this:
 - RANS models are based on statistical averaging and individual fluctuations are not obtained by simply subtracting the mean from the instantaneous velocity fields. This puts URANS at a disadvantage in visualisation of the vortices.
- Two meshes were used to study the axial inflow case using LES. Mesh 1 being coarser and Mesh 2 the finer one. The results of the various study undertaken in this case are listed below:
 - Instantaneous wall friction coefficient (C_f , equation 5.1) contours (at different time instants) were used to visualise the spiral vortex distribution over the cone. It showed qualitatively good agreement with the experiments for both meshes.
 - To check the point at which the spiral vortices started growing, a net meridional profile of fluctuation C_f was made. Comparing with the experiments, both meshes under-predicted this point. The possible reason for this is the high spatial distance between two mesh nodes in the axial and azimuthal direction.
 - Referring to the above statement, the critical point simulated by Mesh 2 was lower than that by Mesh 1. This indicates that the mesh spatial refinement might not be the dominant factor. The SGS viscosity (modelled by WALE) plays an important role in this critical point and if a smaller SGS viscosity is under-predicted in the near wall region, it would under-predict the critical point.
 - The local Reynolds number (Re_l , equation 6.1) distribution with local rotation ratio (S , equation 6.2) showed good agreement with the experiment.
 - For both meshes, the associated critical Reynolds number was under-predicted as a result of the under-predicted critical point.

- To study the spatial distribution of the vortices along the length of the cone, the C_f variation in Y/D at different axial locations were taken and the trend was analysed using a power law fit (as the best fit). The vortex pairs were counted by the number of peaks of C_f as the number of pairs distributed around the circumference of the cone.
- The effect of the mesh sizes was visible by observing the simulated number of vortex pairs. The finer mesh, as expected, showed more vortex pairs but neither of the meshes was fine enough to quantitatively agree with the experiments by Tambe et al. [5].
- A non-axial inflow of 2° incidence was given as the final case to study. Mesh 2, the finer one, was chosen for this. To set up the simulation, the velocity components were changed. The horizontal velocity component was set to, $U_\infty \cos(2^\circ)$ and the vertical component was set to $U_\infty \sin(2^\circ)$. The simulation is still in its development stage, as could be seen by the running average of the vertical velocity component. The results of this preliminary study are itemised below:
 - The instantaneous C_f contours failed to show the experimentally observed (by Tambe et al. [5]) stark spatial delay in the formation of the vortex structures. To check if the setup captured the delay, the C_f fluctuations were obtained. A slight spatial delay was indeed observed.
 - The obtained critical point with the axial and non-axial cases were compared after the same physical time interval (0.15 s), The non-axial case showed a slight spatial delay ($X/D = 0.47$) compared to the axial case ($X/D = 0.44$). With all other parameters in the setup being constant, other than the incidence angle given to the flow, it was concluded that the simulation of the non-axial flow does indeed capture the spatial delay in the formation of the vortical structures.
 - Experiments by Tambe et al. [5] found that the non-axial flow induced asymmetry in the flow over the cone. To characterise this asymmetry, local Reynolds number and local rotation ratio were used. The variation of the local Reynolds number in the windward region did not seem to quantitatively match with the experiments and this might be because the simulations have not yet run for enough timesteps.
 - Asymmetry was also shown using the wall parallel transient mean velocity profiles on both the leeward and windward meridian.
 - The momentum mixing was visualised using both the transient mean wall parallel velocity profiles and the respective contours on both the windward and leeward side. The momentum mixing process was seen to be gradual in both the leeward and windward side when compared to the axial case. Further, the mixing process was gradual at the leeward side in comparison to the windward edge. Both the observations, qualitatively agreeing with the experiments by Tambe et al. [5].
 - The same method as the axial case was used to calculate the number of vortex pairs. The simulations, like the experiments, predicted delay in the start of the formation of the vortices with local rotation ratio. The lower number of simulated vortices is attributed to the high spatial distance between mesh nodes in the azimuthal direction. The trend through the simulations, however, for both the axial and non-axial cases, did not agree with the experiments and further investigation into this is needed.

8.2. Limitations

A few of the limitations in this thesis are mentioned below:

- The mesh could not be refined further as it would have been computationally expensive since maintaining the CFL number to less than 1 was important to maintain solver stability and accuracy of results. This CFL number is directly related to the mesh size and time-step chosen.
- Another limitation regarding the refinement of the mesh was related to the metrics. In particular, the Aspect Ratio (equation 4.1). The solver, ANSYS CFX can handle a maximum Aspect Ratio of 1000 and further refinement, using the current blocking technique, would affect this.
- The simulations were undertaken using the TU Delft HPC cluster setup. The maximum wall time for each job (simulation setup) was 3 days. Due to this and the limited storage allocated to every user, all the backup files needed for a more thorough analysis could not be taken.

- Due to an issue with some of the available backup files, for a few cases, the monitor data could not be extracted from them. Thus the thesis could not include those to provide further evidence concerning the required simulation time.

8.3. Recommendations

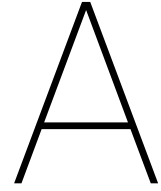
Various recommendations for meshing will be given next along with some recommendations into the future work which could be undertaken in this area.

8.3.1. Meshing

- The blocking technique involved generating an O-Grid and splitting the domain into three different sections, generating 13 blocks around the cone. A better blocking technique might involve generating more blocks, such that more sections would be used to wrap around the cone surface (excluding the cone tip) and thus another few blocks would be used for the region outside the boundary layer.
- Further near wall mesh refinement would allow for the boundary layer to be resolved. This would thus allow the momentum mixing phenomena to be captured in much greater detail and also resolve a greater number of vortices along the length of the cone. The trend through the simulations would then be much closer to the experiments by Tambe et al. [5].
- Using another block covering the cone would allow for a more refined mesh near the boundary layer while overcoming the limitation due to the Aspect Ratio.
- The limitation in the above mentioned method lies in the extremely small radius of the cone tip ($1/100^{\text{th}}$ of the base radius). This would need another extremely small block around the tip of the cone and an interface linking the block around the tip and the block around the cone.

8.3.2. Future Work

- To further study the development of the spiral vortices over the cone, the angle the vortices make with the meridional line can be studied. A potential way to do this would be to study the angle, the out of plane vorticity vectors near the surface makes with the meridional plane.
- The critical point was simulated to be under-predicted in comparison to the experiments by Tambe et al. [5]. The finer mesh under-predicted this point in comparison to the coarser one, thus indicating that mesh refinement may not be the major determining factor in the prediction of this point. The viscosity might be under-predicted in the boundary layer thus triggering the vortices to form earlier. To remedy this, increasing the model constant is recommended (the constant used in the simulations was the CFX default of 0.5).
- The practical application of this study lies in its use as spinners for engines operating under the concept of Boundary Layer Ingestion (BLI). To link the two areas, the research on hub stall indicator by Lei et al. [6] can be used. The fan blades are attached at the intersection of the cone corner. If the velocity vectors are studied near this corner, the angle at which it exits can be used to study how the skewness of this flow affects the stall criterion developed by them.
- Once the simulations are run to completion, the result files of CFX provide the data for all the time steps and a transient analysis would then be more effective. This would lead to the RMS profile of C_f fluctuations to be smooth by itself and the spatial moving mean would not be needed. This would allow the researcher the capture the maximum amplification point of the vortices observed in the experiments.



Plane Boundary Layer Equation

Plane flows or planar flows are two dimensional flows, wherein the streamlines lie in parallel planes. This section will derive the boundary layer equations for a general planar flow with variable properties. Thermal properties will also be looked into so as to provide a more generic study of the behaviour of various fluid properties such as density, viscosity, isobaric specific heat capacity and thermal conductivity. This chapter follows the derivation provided by Schlichting et al [10].

The derivation starts with the Navier-Stokes equations (Note: Although traditionally only the set of momentum equation is considered as the Navier Stokes equation, here the entire collection of continuity, momentum and energy equations are taken as the Navier Stokes equation, as introduced by John D. Anderson Jr. [49]) :

$$\begin{aligned}\frac{D\rho}{Dt} &= -\rho \operatorname{div}(\vec{v}) \\ \rho \frac{D(\vec{v})}{Dt} &= \vec{f} - \operatorname{grad} p + \operatorname{Div}[\mu(2\dot{\epsilon} - \frac{2}{3}\delta \operatorname{div}(\vec{v}))] \\ \rho c_p \frac{DT}{Dt} &= \operatorname{div}(\lambda \operatorname{grad} T) + \beta T \frac{Dp}{Dt} + \Phi\end{aligned}\tag{A.1}$$

Here, \vec{f} is the body force per unit volume. c_p and β represents the isobaric specific heat capacity and the coefficient of thermal expansion respectively. λ is the thermal conductivity. $\frac{Dm}{Dt}$ represent the material derivative of a general function "m". If m is either density (ρ), Temperature (T) or pressure (p), then,

$$\frac{Dm}{Dt} = \frac{\partial m}{\partial t} + \vec{v} \cdot \operatorname{grad} m\tag{A.2}$$

If m is the velocity field (\vec{v}),

$$\frac{D\vec{v}}{Dt} = \frac{\partial \vec{v}}{\partial t} + \operatorname{grad}\left(\frac{1}{2}\vec{v}^2\right) - \vec{v} \times \operatorname{curl} \vec{v}\tag{A.3}$$

To non-dimensionalise the above equations, various reference parameters are taken, l (length), V (velocity, eg. mean flow velocity), T_R (temperature), p_R (pressure). Other reference properties include, ρ_R , μ_R , c_{pR} , λ_R and β_R . The non-dimensional forms are :

$$\begin{aligned}
x^* &= \frac{x}{l}, \quad y^* = \frac{y}{l}, \quad z^* = \frac{z}{l}, \\
t^* &= \frac{tV}{l}, \quad \vec{v}^* = \frac{\vec{v}}{V}, \quad p^* = \frac{p - p_R}{\rho_R V^2}, \\
T^* &= \frac{T}{T_R}, \quad \rho^* = \frac{\rho}{\rho_R}, \quad \mu^* = \frac{\mu}{\mu_R}, \\
c_p^* &= \frac{c_p}{c_{pR}}, \quad \lambda^* = \frac{\lambda}{\lambda_R}, \quad \beta^* = \frac{\beta}{\beta_R}, \\
\dot{\epsilon}^* &= \frac{l}{V} \dot{\epsilon}, \quad \text{grad}^* = l \text{grad}, \quad \text{div}^* = l \text{div}, \\
\text{Div}^* &= l \text{Div}, \quad \text{curl}^* = l \text{curl}, \quad \Phi^* = \frac{\Phi l^2}{\mu_R V^2}
\end{aligned} \tag{A.4}$$

Equation A.1, can now be rewritten by substituting the variables defined in equation A.4,

$$\begin{aligned}
\frac{D\rho^*}{Dt^*} &= -\rho^* \text{div}^*(\vec{v}^*) \\
\rho^* \frac{D(\vec{v}^*)}{Dt^*} &= \frac{1}{\text{Fr}^2} \rho^* \vec{e}_g - \text{grad}^* p^* + \frac{1}{\text{Re}} \text{Div}^* [\mu^* (2\dot{\epsilon}^* - \frac{2}{3} \boldsymbol{\delta} \text{div}^* \vec{v}^*)] \\
\rho^* c_p^* \frac{DT^*}{Dt^*} &= \frac{1}{\text{Re}} \frac{1}{\text{Pr}} \text{div}^* (\lambda^* \text{grad}^* T^*) - K_\rho \text{Ec} \beta^* T^* \frac{Dp^*}{Dt^*} + \frac{\text{Ec}}{\text{Re}} \Phi^*
\end{aligned} \tag{A.5}$$

Equation A.5 introduces many non dimensional physical quantities, they are defined as follows :

- Reynolds Number : Ratio of inertial to viscous forces, given by :

$$\text{Re} = \frac{\rho_R V l}{\mu_R} \tag{A.6}$$

- Froude Number : Indicates the effect of gravity on the flow. Given by :

$$\text{Fr} = \frac{V}{\sqrt{gl}} \tag{A.7}$$

g represents the acceleration due to gravity

- Prandtl Number : Ratio of momentum to thermal diffusivity.

$$\text{Pr} = \frac{\mu_R c_{pR}}{\lambda_R} \tag{A.8}$$

- Eckert Number : Helps to understand the relative importance of kinetic energy to the enthalpy in a flow with heat transfer.

$$\text{Ec} = \frac{V^2}{c_{pR} T_R} \tag{A.9}$$

- Thermal Expansion Number : Defined here as the product of the reference temperature and coefficient of thermal expansion.

$$K_\rho = -\beta_R T_R \tag{A.10}$$

Beginning with equation A.5, the flow domain is broken into an inviscid outer layer and viscous inner boundary layer. Using the boundary layer transformations :

$$\bar{y} = y^* \sqrt{\text{Re}}, \quad \bar{v} = v^* \sqrt{\text{Re}} \tag{A.11}$$

Assuming high Reynolds number ($\text{Re} \rightarrow \infty$, equation A.5 break down to the dimensionless version of the boundary layer equations (sans the Reynolds Number).

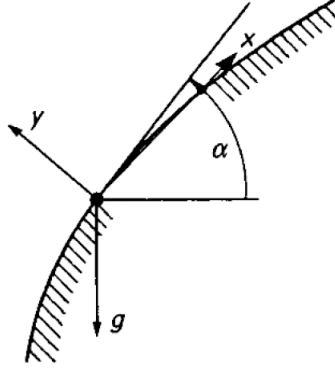


Figure A.1: Coordinate system following the body profile [10]

To obtain these equations back in its dimensional form, the gravitational force can first be broken into two components (from figure A.1, representing the coordinate system following the body contour) :

$$g_x = -g \sin(\alpha), \quad g_y = -g \cos(\alpha) \quad (\text{A.12})$$

The boundary layer equations are thus :

$$\begin{aligned} \frac{\partial(\rho u)}{\partial x} + \frac{\partial(\rho v)}{\partial y} &= 0 \\ \rho(u \frac{\partial u}{\partial x} + v \frac{\partial v}{\partial y}) &= -\rho g \sin(\alpha) - \frac{dp}{dx} + \frac{\partial}{\partial y} (\mu \frac{\partial u}{\partial y}) \\ \rho c_p (u \frac{\partial T}{\partial x} + v \frac{\partial T}{\partial y}) &= \frac{\partial}{\partial y} (\lambda \frac{\partial T}{\partial y}) + \beta T u \frac{dp}{dx} + \mu (\frac{\partial u}{\partial y})^2 \end{aligned} \quad (\text{A.13})$$

B

Linear Stability Theory

This chapter will give a small description of the linear stability theory, which has been used multiple times by various authors as has been seen in chapter 2. The contents of this chapter has been generally referenced from the work of Frank M White [57].

Laminar flows are highly susceptible to changes in Reynolds number. Order of magnitudes as small as $\mathcal{O}(3)$, will trigger the beginning of the end for laminar flows (the Reynolds number at that point is known as the Critical Reynolds Number), thus making turbulent flows much more common in the real world.

Since, to date the concept of turbulence has never mathematically proven to be the final stable state at higher Reynolds number, the discussion of the transition from laminar to turbulent flows (occurring within a range of Reynolds Number) can be done using an empirical prediction of based on spatial amplification rates of linearised stability theory. White [57] provides an excellent outline of the steps involved in stability analysis, it is summarised below :

1. To check the stability of any solution to a physical problem (for example v_0), add a disturbance and substitute the resulting variable in the original governing equation. In this case, consider v' to be the disturbance, the resulting variable will be, $v_0 + v'$
2. The term, v_0 , is subtracted from the original equation obtained in (1) in such a way that the resulting equation satisfies the original governing equations identically. This leaves behind the disturbance equation
3. An assumption that the disturbances are small which would neglect the higher order disturbance terms and thus linearise the equations obtained in (2) . Further assumptions to reduce the complexity of the resulting equation can be made at this step
4. The equations obtained in (3) needs to be homogeneous and thus would need homogeneous boundary conditions thus resulting in an eigenvalue problem
5. The eigenvalues obtained in (4) will be analysed to determine its stability and thus resulting in stability diagrams

C

Baseline Explicit Algebraic Reynolds Stress Model

The contents of this chapter is based on the theory provided in [51], [56] and [58].

The EARSM model first formulated by Wallin and Johansson [56], is an extension of the standard two equation model. The EARSM is implemented with the Baseline (BSL) model in CFX. The BSL model is formulated by first considering the problems faced in the standard $\kappa - \omega$ model, which is its sensitivity to free stream conditions. To rectify this, a blending function was added by [59], such that the model equations are transformed to function as $\kappa - \omega$ near the surface and $\kappa - \epsilon$ away from it. After transforming the $\kappa - \epsilon$ model and adding the κ and ϵ equations to it, the BSL formulation is obtained.

For the EARSM, the Reynolds stresses are evaluated using the anisotropy tensor (a_{ij}) and is mathematically written as,

$$\overline{u_i u_j} = k(a_{ij} + \frac{2}{3}\delta_{ij}) \quad (C.1)$$

The anisotropy tensor is calculated using the implicit algebraic matrix equation:

$$\begin{aligned} N\mathbf{a} &= -A_1\mathbf{S} + (\mathbf{a}\Omega - \Omega\mathbf{a}) - A_2(\mathbf{a}\mathbf{S} - \mathbf{S}\mathbf{a} - \frac{2}{3}tr(\mathbf{a}\mathbf{S})) \\ N &= A_3 + A_4(\frac{P_k}{\epsilon}) \end{aligned} \quad (C.2)$$

Table C.1 lists the values for the A_i coefficients (they depend on the C_i coefficients of the pressure-strain term in the underlying Reynolds stress transport model) used in ANSYS CFX.

A_1	A_2	A_3	A_4
1.245	0	1.8	2.25

Table C.1: A_i coefficients in ANSYS CFX [51]

S_{ij} and Ω_{ij} are the non-dimensional strain-rate and vorticity tensors. The equations defining these are given in 2.14 but defined here with a time scale, τ . $\tau = \frac{\kappa}{\epsilon} = \frac{1}{C_\mu\omega}$. Here, $C_\mu = 0.09$.

The strain rate and vorticity tensors are used to describe the anisotropy tensors in a polynomial,

$$a_{ij} = \beta_1 S_{ij} + \beta_3 (\Omega_{ik}\Omega_{kj} - \frac{1}{3}II\Omega\delta_{ij}) + \beta_4 (S_{ik}\Omega_{kj} - \Omega_{ik}S_{kj}) + \beta_6 (S_{ik}S_{kl}\Omega_{ij} + \Omega_{ik}\Omega_{kl}S_{ij} - \frac{2}{3}IV\delta_{ij} - II\Omega S_{ij}) \quad (C.3)$$

The various coefficients are defined as:

$$\begin{aligned}
\beta_1 &= -N/Q \\
\beta_3 &= -12 \cdot IV / (N \cdot Q \cdot (2N^2 - II_\Omega)) \\
\beta_4 &= -1/Q \\
\beta_6 &= -6 \cdot N / (Q \cdot (2N^2 - II_\Omega))
\end{aligned} \tag{C.4}$$

Here,

$$Q = (N^2 - 2II_\Omega) / A_1 \tag{C.5}$$

The terms, II_Ω, IV are invariants defined as,

$$\begin{aligned}
II_\Omega &= \Omega_{kl} \Omega_{lk} \\
IV &= S_{kl} \Omega_{lm} \Omega_{mk}
\end{aligned} \tag{C.6}$$

In three dimensional cases, to solve for N , a sixth order function is needed and an explicit relation is not derived.

The vorticity tensor is modified to add streamline curvature effects,

$$\Omega_{ij} = \frac{1}{2} \tau \left(\frac{\partial U_i}{\partial x_j} - \frac{\partial U_j}{\partial x_i} \right) - C_{\text{scale}} \cdot \frac{\tau}{A_0} \Omega_{ij}^{cc} \tag{C.7}$$

Ω_{ij}^{cc} is responsible for the curvature correction and is defined as,

$$\Omega_{ij}^{cc} = \epsilon_{ijk} \omega_k^{s-s} \tag{C.8}$$

Here,

$$\omega_k^{ss} = \frac{S_{pl} \dot{S}'_{lq} \epsilon_{pqk}}{2II_S} \tag{C.9}$$

The invariant $II_S = S_{kl} S_{lk}$. The term \dot{S}'_{lq} is given as,

$$\dot{S}'_{lq} = \frac{DS_{ij}}{Dt} + (\epsilon_{imn} S_{jn} + \epsilon_{jmn} S_{in}) \Omega_m^{rot} \tag{C.10}$$

ϵ_{ijk} is the Levi-Chivata factor and is equal to 0 if i,j,k are equal and 1 if they form an even/odd permutation.

The coefficient A_0 needs to be calibrated (default calibration value in CFX is -0.4). The scaling coefficient (C_{scale}) is present to influence the effects of the curvature correction term ($\frac{\tau}{A_0} \Omega_{ij}^{cc}$) for specific flows. Default value is set to 1.

Bibliography

- [1] R. Kobayashi and H. Izumi, “Boundary-layer transition on a rotating cone in still fluid”, *Journal of Fluid Mechanics*, 127:353–364, 1983. doi:10.1017/S0022112083002761.
- [2] R. Kobayashi, Y. Kohama, and M. Kurosawa, “Boundary-layer transition on a rotating cone in axial flow”, *Journal of Fluid Mechanics*, 127:341–352, 1983. doi:10.1017/S002211208300275X.
- [3] S. Tambe, F. Schrijer, A. G. Rao, and L. Veldhuis, “An experimental method to investigate coherent spiral vortices in the boundary layer over rotating bodies of revolution”, *Experiments in Fluids*, 60, 2019. doi:10.1007/s00348-019-2756-8.
- [4] S. Tambe, F. Schrijer, A. G. Rao, and L. Veldhuis. Coherent vortex structures over a rotating spinner under non-axial inflows at low Reynolds number. in *54th 3AF International Conference on Applied Aerodynamics*, 2019.
- [5] S. Tambe, F. Schrijer, A. G. Rao, and L. Veldhuis, “Boundary layer instability over a rotating cone under non-axial inflow”, *Journal of Fluid Mechanics*, 2020 (manuscript submitted).
- [6] V.-M. Lei, Z. S. Spakovszky, and E. M. Greitzer, “A Criterion for Axial Compressor Hub-Corner Stall”, *Journal of Turbomachinery*, 130(3), 05 2008. doi:10.1115/1.2775492.
- [7] E. S. Hendricks. “A review of boundary layer ingestion modeling approaches for use in conceptual design”. Technical report, NASA Glenn Research Center, Cleveland, OH, United States, 2018. URL <https://ntrs.nasa.gov/search.jsp?R=20180005165>.
- [8] A. Uranga, M. Drela, E. Greitzer, N. Titchener, M. Lieu, N. Siu, A. Huang, G. M. Gatlin, and J. Hannon. Preliminary experimental assessment of the Boundary Layer Ingestion benefit for the D8 aircraft. in *52nd Aerospace Sciences Meeting*, 2014. doi:10.2514/6.2014-0906.
- [9] F. T. Nieuwstadt, J. Westerweel, and B. J. Boersma. *Turbulence*. Springer International Publishing, 2016. doi:10.1007/978-3-319-31599-7.
- [10] H. Schlichting and K. Gersten. *Boundary-Layer Theory*. Springer Berlin Heidelberg, 2017.
- [11] G. I. Taylor, “Viii. stability of a viscous liquid contained between two rotating cylinders”, *Philosophical Transactions of the Royal Society of London. Series A, Containing Papers of a Mathematical or Physical Character*, 223(605-615):289–343, 1923. doi:10.1098/rsta.1923.0008.
- [12] H. Görtler, “Instabilität laminarer grenzsichten an konkaven wänden gegenüber gewissen dreidimensionalen störungen”, *ZAMM - Journal of Applied Mathematics and Mechanics / Zeitschrift für Angewandte Mathematik und Mechanik*, 21(4):250–252, 1941. doi:10.1002/zamm.19410210408.
- [13] M. Karp and M. J. P. Hack, “Transition to turbulence over convex surfaces”, *Journal of Fluid Mechanics*, 855:1208–1237, 2018. doi:10.1017/jfm.2018.690.
- [14] J. M. Floryan and W. S. Saric, “Stability of gortler vortices in boundary layers”, *AIAA Journal*, 20(3):316–324, 1982. doi:10.2514/3.51076.
- [15] V. Patel and F. Sotiropoulos, “Longitudinal curvature effects in turbulent boundary layers”, *Progress in Aerospace Sciences*, 33(1):1 – 70, 1997. ISSN 0376-0421. doi:https://doi.org/10.1016/S0376-0421(96)00001-2.
- [16] J. Piquet and V. Patel, “Transverse curvature effects in turbulent boundary layer”, *Progress in Aerospace Sciences*, 35(7):661 – 672, 1999. ISSN 0376-0421. doi:https://doi.org/10.1016/S0376-0421(99)00007-X.
- [17] P. Bradshaw, “Turbulent secondary flows”, *Annual review of fluid mechanics*, 19(1):53–74, 1987.

- [18] D. Chang and S. Tavoularis, "Unsteady Numerical Simulations of Turbulence and Coherent Structures in Axial Flow Near a Narrow Gap", *Journal of Fluids Engineering*, 127(3):458–466, 02 2005. ISSN 0098-2202. doi:10.1115/1.1900140.
- [19] V. J. Fidalgo, C. A. Hall, and Y. Colin, "A Study of Fan-Distortion Interaction Within the NASA Rotor 67 Transonic Stage", *Journal of Turbomachinery*, 134(5), 05 2012. ISSN 0889-504X. doi:10.1115/1.4003850.
- [20] R. Kobayashi, Y. Kohama, and C. Takamadate, "Spiral vortices in boundary layer transition regime on a rotating disk", *Acta Mechanica*, 35(1-2):71–82, 1980. doi:10.1007/BF01190058.
- [21] Y. Kohama, "Study on boundary layer transition of a rotating disk", *Acta Mechanica*, 50(3-4):193–199, 1984. doi:10.1007/BF01170959.
- [22] Y. Kohama and R. Kobayashi, "Behaviour of spiral vortices on rotating axisymmetric bodies", *Report of Institute of High Speed Mechanics, Tohoku University, Japan*, 47:27, 1983.
- [23] R. Kobayashi, "Linear stability theory of boundary layer along a cone rotating in axial flow", *Bulletin of JSME*, 24(192):934–940, 1981. doi:10.1299/jsme1958.24.934.
- [24] Y. Kohama, "Behaviour of spiral vortices on a rotating cone in axial flow", *Journal of Fluid Mechanics*, 51: 105–117, 1984. doi:10.1007/BF01177066.
- [25] R. Kobayashi, Y. Kohama, T. Arai, and M. Ukaku, "The Boundary-layer Transition on Rotating Cones in Axial Flow with Free-stream Turbulence : Fluids Engineering", *JSME international journal*, 30(261):423–429, 1987. doi:10.1299/jsme1987.30.423.
- [26] M. Wimmer, "Viscous flows and instabilities near rotating bodies", *Progress in Aerospace Sciences*, 25(1): 43 – 103, 1988. ISSN 0376-0421. doi:10.1016/0376-0421(88)90012-7.
- [27] H. L. Reed and W. S. Saric, "Stability of three-dimensional boundary layers", *Annual Review of Fluid Mechanics*, 21(1):235–284, 1989.
- [28] W. S. Saric, "Görtler vortices", *Annual Review of Fluid Mechanics*, 26(1):379–409, 1994.
- [29] R. Kobayashi, "Review: Laminar-to-Turbulent Transition of Three-Dimensional Boundary Layers on Rotating Bodies", *Journal of Fluids Engineering*, 116(2):200–211, 06 1994. doi:10.1115/1.2910255.
- [30] D. Degani and L. B. Schiff, "Numerical simulation of the effect of spatial disturbances on vortex asymmetry", *AIAA Journal*, 29(3):344–352, 1991. doi:10.2514/3.10585.
- [31] N. M. El-Hady and T. A. Zang, "Large-eddy simulation of nonlinear evolution and breakdown to turbulence in high-speed boundary layers", *Theoretical and Computational Fluid Dynamics*, 7(3):217 – 240, 1995. doi:10.1007/BF00312364.
- [32] M. Germano, U. Piomelli, P. Moin, and W. H. Cabot, "A dynamic subgrid-scale eddy viscosity model", *Physics of Fluids A: Fluid Dynamics*, 3(7):1760–1765, 1991. doi:10.1063/1.857955.
- [33] P. Moin, K. Squires, W. Cabot, and S. Lee, "A dynamic subgrid-scale model for compressible turbulence and scalar transport", *Physics of Fluids A: Fluid Dynamics*, 3(11):2746–2757, 1991. doi:10.1063/1.858164.
- [34] S. Garrett and N. Peake, "The absolute instability of the boundary layer on a rotating cone", *European Journal of Mechanics - B/Fluids*, 26(3):344 – 353, 2007. ISSN 0997-7546. doi:10.1016/j.euromechflu.2006.08.002.
- [35] C. Hah, D. C. Rabe, T. J. Sullivan, and A. R. Wadia, "Effects of Inlet Distortion on the Flow Field in a Transonic Compressor Rotor", *Journal of Turbomachinery*, 120(2):233–246, 04 1998. doi:10.1115/1.2841398.
- [36] J. E. Giuliani and J.-P. Chen, "Fan response to boundary-layer ingesting inlet distortions", *AIAA Journal*, 54(10):3232–3243, 2016. doi:10.2514/1.J054762.
- [37] D. K. Hall, E. M. Greitzer, and C. S. Tan, "Analysis of Fan Stage Conceptual Design Attributes for Boundary Layer Ingestion", *Journal of Turbomachinery*, 139(7), 03 2017. ISSN 0889-504X. doi:10.1115/1.4035631.

- [38] V. Kolář, “Vortex identification: New requirements and limitations”, *International Journal of Heat and Fluid Flow*, 28(4):638 – 652, 2007. ISSN 0142-727X. doi:10.1016/j.ijheatfluidflow.2007.03.004. Including Special Issue of Conference on Modelling Fluid Flow (CMFF’06), Budapest.
- [39] ANSYS, Inc. “ANSYS CFD Post, Release 19.2”.
- [40] J. Jeong and F. Hussain, “On the identification of a vortex”, *Journal of Fluid Mechanics*, 285:69–94, 1995. doi:10.1017/S0022112095000462.
- [41] M. Jiang, R. Machiraju, and D. Thompson, “Detection and visualization of”, *The visualization handbook*, 295, 2005.
- [42] J. C. Hunt, A. A. Wray, and P. Moin, “Eddies, streams, and convergence zones in turbulent flows”, 1988.
- [43] U. Dallmann. *Topological structures of three-dimensional vortex flow separation*. 1983. doi:10.2514/6.1983-1735.
- [44] V. Holmén. Methods for vortex identification, 2012. ISSN 1404-6342. Student Paper.
- [45] Y. Levy, D. Degani, and A. Seginer, “Graphical visualization of vortical flows by means of helicity”, *AIAA Journal*, 28(8):1347–1352, 1990. doi:10.2514/3.25224.
- [46] C. H. Berdahl and D. S. Thompson, “Eduction of swirling structure using the velocity gradient tensor”, *AIAA Journal*, 31(1):97–103, 1993. doi:10.2514/3.11324.
- [47] R. C. Strawn, D. N. Kenwright, and J. Ahmad, “Computer visualization of vortex wake systems”, *AIAA journal*, 37(4):511–512, 1999.
- [48] I. A. Sadarjoen, F. H. Post, Bing Ma, D. C. Banks, and H. . Pagendarm. Selective visualization of vortices in hydrodynamic flows. in *Proceedings Visualization ’98 (Cat. No.98CB36276)*, pages 419–422, Oct 1998. doi:10.1109/VISUAL.1998.745333.
- [49] J. D. A. Jr. *Computational Fluid Dynamics : The Basics With Applications*. McGraw Hill Education (India) Private Limited, 2012.
- [50] S. B. Pope. *Turbulent Flows*. Cambridge University Press, 2000. doi:10.1017/CBO9780511840531.
- [51] ANSYS, Inc. “ANSYS CFX, Release 19.2”.
- [52] J. Smagorinsky, “General circulation experiments with the primitive equations”, *Monthly Weather Review*, 91(3):99–164, 1963. doi:10.1175/1520-0493(1963)091<0099:GCEWTP>2.3.CO;2.
- [53] D. K. Lilly, “A proposed modification of the germano subgrid-scale closure method”, *Physics of Fluids A: Fluid Dynamics*, 4(3):633–635, 1992. doi:10.1063/1.858280.
- [54] F. Nicoud and F. Ducros, “Subgrid-scale stress modelling based on the square of the velocity gradient tensor”, *Flow, Turbulence and Combustion*, 62:183–200, 1999. doi:10.1023/A:1009995426001.
- [55] ANSYS, Inc. “ANSYS ICEM CFD, Release 19.2”.
- [56] S. Wallin and A. V. Johansson, “An explicit algebraic reynolds stress model for incompressible and compressible turbulent flows”, *Journal of Fluid Mechanics*, 403:89–132, 2000. doi:10.1017/S0022112099007004.
- [57] F. M. White. *Viscous Fluid Flow*. The McGraw-Hill Companies, 2006.
- [58] S. Wallin and A. V. Johansson, “Modelling streamline curvature effects in explicit algebraic reynolds stress turbulence models”, *International Journal of Heat and Fluid Flow*, 23(5):721 – 730, 2002. ISSN 0142-727X. doi:https://doi.org/10.1016/S0142-727X(02)00168-6. URL <http://www.sciencedirect.com/science/article/pii/S0142727X02001686>.
- [59] F. R. Menter, “Two-equation eddy-viscosity turbulence models for engineering applications”, *AIAA Journal*, 32(8):1598–1605, 1994. doi:10.2514/3.12149.